HIGH RESOLUTION CHARACTERIZATION OF AQUIFERS TO IMPROVE FLOW AND TRANSPORT MODELS OF HIGHLY HETEROGENEOUS MEDIA

By

Mine Dogan Diker

A DISSERTATION

Submitted to
Michigan State University
in partial fulfillment of the requirements
for the degree of

Geological Sciences - Doctor of Philosophy

ABSTRACT

HIGH RESOLUTION CHARACTERIZATION OF AQUIFERS TO IMPROVE FLOW AND TRANSPORT MODELS OF HIGHLY HETEROGENEOUS MEDIA

By

Mine Dogan Diker

Aquifers are the primary sources of clean drinking water. Pollution in aquifers is one of the most challenging and important environmental problems. It is not only extremely complex to map but also difficult to remediate. Flow and transport of water and pollutants in porous media requires detailed characterization of the properties of the media. The main property which controls the flow and transport is hydraulic conductivity (*K*), which can be defined as the ability of the media to let the water flow through. Intensive studies to map the distribution of hydraulic conductivity are necessary to model the plume migration. Conventional in-situ aquifer characterization techniques are invasive and lack the necessary high resolution. Therefore, novel methods are required to improve the methods to monitor and simulate the flow and transport through aquifers.

This study introduces a combination of novel techniques to provide the necessary information related to porous media. The proposed method was tested at a highly heterogeneous site called the Macro Dispersion Experiment (MADE) site in Mississippi. The MADE site is a very well studied site where several large scale tracer tests were conducted in the 1980s and 1990s. The tracers used for these tests were monitored using more than 300 multi-level sampler (MLS) wells. Concentration measurements showed that the majority of the mass stayed near the injection area, whereas minute concentrations were measured further down-gradient. This behavior is significantly different from the simulations created using models based on the

Advection-Dispersion Equation (ADE). This behavior and the inability to explain this using most models has led to a major debate in the hydrologic science community.

The hypothesis of this study is that the ADE based models can reproduce simulations of the measured transport when the models are parameterized with sufficient high-resolution hydraulic conductivity data. Two novel high resolution characterization methods, the direct-push high resolution hydraulic conductivity (HRK) tool and 3D full-resolution ground penetrating radar (GPR) were combined to generate 3D K fields using fractal stochastic methods. This study demonstrated that the complementary geophysical data can be used to reduce the K variance by dividing the aquifer into hydrofacies. This approach, in combination with a fractional differencing filter, simplifies the statistically complex distribution of K. Fractional differencing was also capable of removing the long range dependence in vertical K profiles to investigate the underlying K distribution. The 3D K fields were then used to test the ADE based modeling approach at the site and resulting concentrations were compared to one of the large scale tracer experiments. The simulations in this study resulted in mass distributions comparable to those measured during the tracer test experiments. They successfully reproduced the extent of the plume in both 1D and 2D using K fields based on solely field data. Additional tests emphasized the importance of high-resolution data to parameterize K models to successfully simulate flow and transport using the ADE model.

For my parents, Emine and Sami Dogan, for all the love, trust, and support they provided I am proud for being able to make them proud of me.	1 .

ACKNOWLEDGEMENTS

First and foremost, I would like to state that there are no words to express my gratitude for my advisor Dr. Remke L. van Dam. He supported me, encouraged me, challenged me and, most importantly, he inspired me. Together, we collected millions of GPR traces during many cold and humid nights in Mississippi. He became not only an advisor, but also a colleague and a most supportive friend throughout this process. His expertise as an earth scientist guided me towards becoming a better scientist with an optimistic character. Without him, my experience as a graduate student would not be as bright and satisfying. "Beep, evet!"

Second, I would like to acknowledge my co-advisor, Dr. David W. Hyndman, for being a great role model for my academic personality and guiding me through the great deal of stress that every graduate student experiences. His confidence in me made every task seem doable and every target reachable. It was a great gift and privilege having not only one, but two wonderful advisors.

I would like to thank Dr. Mark M. Meerschaert for his endless patience for my questions, explanations of challenging statistical concepts, and belief that I could make this project work. His creative insight about our work was exciting and gave me clarity about how to proceed. I also would like acknowledge Drs. Brian Hampton, Kamini Singha, and David Benson for their contribution to my research. They were the ones who made my research complete and strong.

I would like to thank the Hydrogeology Lab members, especially my friends, Erin King and Alex Kuhl, who have been very encouraging and supportive throughout this process. Gizem and Mustafa Ali, for listening to my endless explanations and practice talks, just their existence made many things easier than they actually were. And, my graduate school sister, Dr. Nicole D.

LaDue, for being the magnificent best friend, guiding me through the cultural differences, and challenges. Thanks lady!

Many thanks dear Jackie, Jennae, and Heidi of our departmental office for all of their help handling paperwork and managing deadlines. Their smiling faces always made me thankful to be in the Department of Geological Sciences.

I would like to acknowledge Dr. Gulcin Ozurlan Agacgozgu, who is a role model for me as an intelligent, and confident female scientist, and Dr. Argun Kocaoglu since they kept supporting me all the way from Turkey.

My husband, Kaya, thank you for joining me on this immense journey, and following me all the way to Michigan. Your existence made East Lansing a real home for me and you have helped me grow stronger from this experience.

Finally, my family, I love you to the pieces. My father, Sami Dogan, has been always the greatest role model and my biggest supporter. I could not be who I am without him. Thanks, Dad! My mother, Emine Dogan, made the biggest sacrifice of accepting my decision to live far away, always missing her only daughter. I want to thank to my brother, Malik, for leading and encouraging me to venture out of my safe shell and become a world citizen. Wish you see the better ones from your sons, my beloved nephews, Saman Eren and Bilge Cinar.

TABLE OF CONTENTS

LIST OF TABLES	X
LIST OF FIGURES	xi
Chapter 1 Prologue	1
1.1 Introduction	
1.2 Aquifer Characterization	3
1.3 The MADE Site	6
1.4 Methods	10
1.5 Outline of the thesis/dissertation	14
REFERENCES	18
Chapter 2 Hydrostratigraphic analysis of the MADE site with full-resolution GPR and of	direct-
push hydraulic profiling	21
Abstract	21
2.1 Introduction	22
2.2 Methods	24
2.3 Results	27
2.4 Conclusions	31
2.5 Acknowledgments	32
APPENDIX	34
REFERENCES	41
Chapter 3 Hydraulic conductivity fields: Gaussian or not?	43
Abstract	43
3.1 Introduction	44
3.2 Statistical analysis	48
3.3 Model validation	56
3.4 Discussion	58
3.5 Conclusions	59
3.6 Acknowledgments	60
APPENDICES	61
APPENDIX 3.1: Fractional difference filter	62
APPENDIX 3.2: Flow-Transport Simulations	65
REFERENCES	
Chapter 4 Novel characterization method provides a major advance for flow and transp	ort
prediction	76
Abstract	76
4.1 Introduction	77
4.2 Methods	78
4.3 Results	81
4.4 Discussion and Conclusions	83
REFERENCES	86

Chapter 5 Quantifying the value of different data sets and modeling scho	emes for flow and
transport simulations	89
5.1 Introduction	89
5.2 Complementary GPR data	92
5.3 Cost-benefit analysis	94
5.3.1 Transient flow	95
5.3.2 Flowmeter K	98
5.3.3 Effect of conditioning data density	99
5.3.4 Complementary GPR data	
5.4 Conclusions	104
REFERENCES	107
Chapter 6 Synthesis	
REFERENCES	

LIST OF TABLES

Table 1.1 Inventory of collected GPR data.	14
Table A2.1 Single-sample K-S tests of four HRK profiles for facies and layers identified in full resolution 3D GPR data (see Figures 2.1 and 2.3a for locations). Columns, "SEGMENT", name of segment (facies/sub-facies/layer), "N_SAMPLE", number of HRK measurements used,	
"p_FOR_LOG_K", p values for log ₁₀ K using single-sample K-S test with 95% CI	36
Table A2.1 (cont'd)	37
Table A2.2 Statistical comparison of K values for four identified radar facies and adjacent segments, where p values were calculated using two-sample K-S tests. Columns, "SEGMENT" names of compared consecutive segments (facies/sub-facies/layers), "p_FOR_LOG_K", p values of compared consecutive segments (facies/sub-facies/layers).	
for log ₁₀ K using two-sample K-S test with 95% CI.	37
Table A2.2 (cont'd)	38
Table 5.1 Quantitative measures for the comparison of simulation scenarios and field experimental	ent
(R ² values were calculated comparative to the MADE-1 experiment t=503 days in the first row	

LIST OF FIGURES

Figure 1.1 Number of articles over the years which comprise "aquifer characterization" as keywords. For interpretation of the references to color in this and all other figures, the reader is referred to the electronic version of this dissertation
Figure 1.2 Vertically exaggerated (x5) hydraulic conductivity cross-section along A-A' using 1560 flowmeter <i>K</i> measurements [<i>Boggs</i> , 1991] (see Figure 1.4 for location)
Figure 1.3 Multi level sampler and flowmeter well setup at the MADE site (photo courtesy: stanford.edu).
Figure 1.4 Site map showing the locations for flowmeter <i>K</i> measurements with cross-section line (A-A' in Figure 1.1), multilevel sampler wells, and test boundary
Figure 1.5 Panoramic view of the site showing the source location (metal pipes in the centerfront) and GPR data collection setup (on the right) (photo courtesy: Kaya Diker)
Figure 1.6 Site map showing HRK and GPR measurement locations, and the original MADE test boundary.
Figure 1.7 Side view of DP High Resolution <i>K</i> (HRK) probe (photo courtesy: Kaya Diker) 13
Figure 2.1 (a) Map of the MADE site on Columbus Air Force Base (AFB) with GPR measurement lines. The GPR survey coordinates are shown in blue. The blowup of the ICA cube
(144 m ²) shows DP sites and locations of the 3D GPR cubes in Figures 2.1b and c (yellow shaded area) and the profile in Figure 2.2 (red dashed line); viewing angles are indicated with arrows in corresponding colors. Full-resolution 3D GPR data cubes at (b) 100 MHz and (c) 50 MHz are shown with no vertical exaggeration. An envelope was used to render negative amplitudes transparent; number labels in Figure 2.1b are discussed in the text
Figure 2.2 Interpretation of GPR and HRK data at line 105E (see Figure 2.1 for location). (a) GPR profile with red (positive) to blue (negative) amplitude scale using combined 100 MHz and 50 MHz data; black triangles indicate the zone where the two data sets were averaged. In addition to processing mentioned in the text, these data were plotted with an energy decay gain. (b) Continuous reflections identified using an automated picking algorithm and interpreted GPR facies (color shaded). (c) Qualitative interpretation of GPR facies with HRK data; facies boundaries are marked by horizontal lines.
Figure 2.3 (a) 3D GPR facies boundaries (shaded to visualize topography) with collocated DP HRK profiles. Descriptive statistics of these <i>K</i> data for (b) all saturated material above the aquitard, (c) GPR facies, (d) sub-facies, and (e) layers. Box plots show the sample median,
interquartile range, and positions of extreme values. (f) Variance of $\log_{10} K$ and $\ln K$ values for the data in Figures 2.3b–2.3e, respectively. The red line is a power fit through the medians of the variance values for each group (horizontal axis in log scale)

Figure A2.4 (a) Cross plot of $\log_{10} K$ mean and variance for high resolution K data from four
DP profiles (see Figure 2.1 for location and Figure 2.2 for data). (b) Cross plot of $\log_{10} K$ mean and the slopes of linear trends of the change in $\log_{10} K$ with depth. In these plots, each facies is shown by a different symbol and color. The number next to each symbol indicates the DP profile $(1, 2, 3, 3)$ and 4 represent 111108A, 111108B, 111108C, and 121108A, respectively)
Figure 3.1 Layout of Macro Dispersion Experiment test site, showing key features of MADE experiments, as well as the locations of GPR data collected for this project. The inset of the 12×12 m ICA (Intensively Cored Area) cube shows the locations of the four HRK profiles and the 2D transect discussed in this paper. 47
Figure 3.2 Histogram of $\ln K$ for HRK profile 121108A (see map in Figure 3.1) before (a) and after (b) applying the fractional difference filter (1) with d =0.9. The filtered data are organized into a unimodal distribution with a sharper peak and a heavier tail than the best fitting Gaussian probability density function (black line).
Figure 3.3 Autocorrelation function for $\ln K$ from HRK profile 121108A (see Figure 3.1) before (a) and after (b) applying the fractional difference filter (3.1) with d =0.9. Autocorrelations inside dashed lines are statistically zero.
Figure 3.4 Simulated $\ln K$ field without (a) and with (b) GPR facies (dashed lines), conditioned on four HRK profiles (vertical black lines). Histogram (c, d) of one column (white line at $x = 172$ m) from simulated $\ln K$ field (a, b, respectively) after applying the fractional difference filter (1) with $d=0.9$. The histogram (c) fits a Gaussian model, but the histogram (d) from facies simulation (b) deviates from Gaussian shape, similar to measured HRK data (Figure 3.2b) 53
Figure 3.5 Fractionally differenced ln <i>K</i> data (a) from the shallowest facies at horizontal location 174 m fits a Gaussian distribution. Deepest facies (b) at horizontal location 170 m deviates from the Gaussian model. These probability plots show the sorted data on the horizontal axis, and the corresponding model percentiles for the best fitting Gaussian model on the vertical axis. If the data fits this model, the points will follow the reference line, with some random scatter 55
Figure A3.6 Simulated plume 500 days after the end of injection, using a constant <i>K</i> value in each GPR facies (top), the <i>K</i> field from Figure 3.4a without GPR facies (middle), and the <i>K</i> field from Figure 3.4b with GPR facies (bottom).
Figure A3.7 Normalized concentration profiles (top) 500 days after the end of injection, and normalized concentration breakthrough curves (bottom), measured at location x=172 m, from the three simulations illustrated in Figure A3.6.
Figure 4.1 (a) Map of the MADE site with the test boundary (dashed line) and sampling locations; gray shaded rectangle shows the model domain used for simulations. (b) Model domain with HRK, injection, and observation borehole locations.
Figure 4.2 Relative mass distribution profiles 501 days after the injection. The black line shows the mean of the simulations along with 2σ error range (in gray shaded area); the red line shows the profile for the MADE-1 observations.

Figure 4.3 Vertically integrated contour maps of relative mass 503 days after the start of injection for MADE-1 experiment (a), the mean of the 6 simulations that met the head criteria (b) a sample simulation which matches the head change criteria best (c). All three contour maps were created following the same interpolation procedure, as discussed in the text
Figure 5.1 A detailed map of the model domain with locations of flowmeter <i>K</i> (orange) and HRK measurements (blue) and multi-level sampler (grey) wells. The area of 3D GPR data is given by the rectangle with green dashed line. Injection wells are given with red stars. See Figure 4.1 for the location within the larger MADE site
Figure 5.2 Vertically integrated contour maps of relative mass; (a) MADE-1 experiment at t=503 days, (b) mean of 6 simulations, (c) best head change simulation. <i>K</i> fields for the simulations in (b) and (c) were based on a combination of HRK data and GPR facies (these maps can be compared with Figure 4.2, which presents contour maps of relative mass for <i>K</i> fields based on just HRK data).
Figure 5.3 Relative mass distribution profiles for the MADE-1 experiment at $t=503$ days (red line), and the mean and 2σ range of 6 simulations (black line and gray shaded area, respectively). Simulations used (a) K fields based on just HRK data and (b) K fields based on a combination of HRK data and GPR facies
Figure 5.4 Vertically integrated contour maps of normalized mass; (a) MADE-1 experiment at t=503 days, (b) base simulation, (c) transient flow simulation
Figure 5.5 Normalized mass distribution profiles of the MADE-1 experiment at t=503 days (red line), base simulation (black line), and transient flow scheme (blue line)
Figure 5.6 Vertically integrated contour maps of normalized mass; (a) MADE-1 experiment at t=503 days, (b) base simulation, (c) simulation based on just flowmeter <i>K</i> data
Figure 5.7 Normalized mass distribution profiles of the MADE-1 experiment at $t=503$ days (red line), base simulation (black line), and simulation based on just flowmeter K data (blue line) 99
Figure 5.8 Vertically integrated contour maps of normalized mass: (a) MADE-1 experiment at t=503 days, (b) base simulation based on all 25 HRK profiles, and simulations based on (c) 20, (d) 15, (e) 10, and (f) 5 randomly selected HRK profiles. The randomly selected HRK profiles used to generate the <i>K</i> fields are shown with blue symbols; see Figure 5.1 for the location of all 25
Figure 5.9 Normalized mass distribution profiles of the MADE-1 experiment at t=503 days (red line), base simulation (black line), and simulations based randomly selected number of HRK profiles (blue line). (a) 80% of HRK profiles (#'s 2, 3, 4, 5, 6, 7, 8, 10, 11, 12, 14, 15, 16, 17, 18, 19, 20, 22, 23, 24), (b) 60% of HRK profiles (#'s 2, 3, 4, 8, 10, 11, 12, 13, 14, 16, 17, 18, 20, 21, 24), (c) 40% of HRK profiles (#'s 2, 5, 7, 11, 12, 14, 17, 18, 19, 22) (d) 20% of HRK profiles (#'s 8, 11, 14, 15, 24). See Figure 5.1 for the locations of the HRK profiles

Figure 5.10 Vertically integrated contour maps of normalized mass: (a) MADE-1 experiment at t=503 days, (b) base simulation, and (c) simulation based on a combination of HRK data and GPR facies
Figure 5.11 Normalized mass distribution profiles of the MADE-1 experiment at t=503 days (red line), base simulation (black line), and simulation based on a combination of HRK data and GPR facies

Chapter 1

Prologue

1.1 Introduction

It is an extensive challenge to understand all aspects of underground water such as storage, flow, transport, and interactions with surrounding material, since aquifers constitute the most important natural medium for storage, purification and filtering of fresh water. Hydraulic conductivity (*K*) is the main property that controls water flow in porous media [e.g., *Dagan*, 1989] *K* can simply be defined as the ability of any porous medium to allow the fluids to flow through. It depends on the pore and grain size, their distribution, and sorting. To solve environmental problems, accurately parameterized models that describe the flow of water and solutes in aquifers are critical, since models that can consistently and realistically simulate flow and transport rely on accurate representations of *K*. Although there have been many studies on these topics involving in-situ measurements of aquifer properties and pollution monitoring, the methods utilized in these studies have certain limitations and are mostly invasive. Furthermore, the lack of an in-situ and non-invasive method to directly measure *K* is a major obstacle to create realistic simulations of flow and transport through aquifers.

Even though several characterization methods exist, resolution still remains as an issue. Characterization methods can be combined with Gaussian geostatistical methods to develop 3D K fields to overcome the resolution problem, which at sites with low levels of heterogeneity provides acceptable results [Freyberg, 1986; Mackay et al., 1986, Garabedian et al., 1991; LeBlanc et al., 1991, Hyndman et al., 2000; Phanikumar et al., 2005]. Parameterization of K fields for flow and transport modeling in highly heterogeneous aquifers, however, remains

challenging. Various stochastic and geostatistical methods that have been proposed to improve simulations of highly heterogeneous *K* fields generally rely on conventional in-situ measurement methods that provide limited spatial sampling, and have large support volumes with unknown geometries. Therefore, innovative approaches to measure and interpret *K* are necessary to truly understand flow and transport through highly heterogeneous media.

The main goal of this study is to develop a novel approach for predicting flow and transport in highly heterogeneous porous media with the aid of novel measurement and stochastic methods. If successful, this approach will provide a significant contribution to ameliorate real-world problems related to ground water and aquifers. The principal aspect of this research involves high-resolution characterization of hydraulic conductivity and aquifer structure. Descriptive statistics and distribution tests were used to confirm the consistency of the data sets used in this study. This comparative approach forms the foundation of this research, since there is no known direct relationship between geophysical parameters and K. Consecutively; geophysics-derived information was integrated with in-situ K measurements using stochastic methods. Fractal methods, which are capable of representing the long-memory nature and connectivity of K, were used to populate simulated 3D K fields to run flow and transport models.

In this thesis, detailed *K* data from a heterogeneous site were used to model fluid flow and solute transport utilizing the advection-dispersion equation. A combination of novel and traditional measurements and data processing methods was explored for detailed characterization of shallow, unconfined aquifers.

1.2 Aquifer Characterization

Aquifer characterization is a broad topic addressed by many researchers from different disciplines, including earth science, hydrology, environmental engineering, and statistics. Researchers from these fields have been employing many different tools including laboratory measurements [*Illman et al.*, 2010], in-situ measurements [*Kabala*, 1993], macro-scale field experiments [*Garabedian et al.*, 1991; *Boggs*, 1991], geophysical imaging [*Dafflon et al.*, 2011], and computer simulations [*Gómez-Hernádez and Wen*, 1998]. Figure 1.1 shows the numbers of articles in Google Scholar for the keyword "aquifer characterization". In recent years, the number of the articles has increased significantly, and technological advances promote more interest in this matter. Aquifer characterization methods, involving the measurement and/or estimation of *K*, will be discussed from here on.

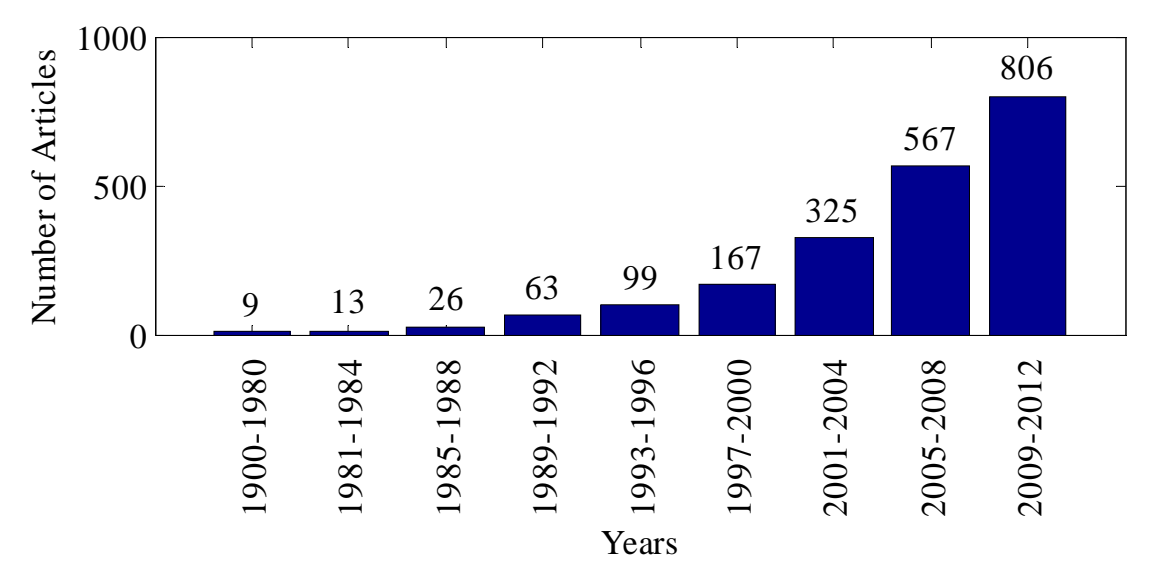


Figure 1.1 Number of articles over the years which comprise "aquifer characterization" as keywords. For interpretation of the references to color in this and all other figures, the reader is referred to the electronic version of this dissertation.

There are several different methods to determine hydraulic conductivity. Empirical approaches involving pedotransfer functions rely on textural analysis for defining the physical

properties of the medium such as pore/grains/fracture size, distribution, and organization.

Textural analysis involves collecting core samples from the aquifer and sieving these samples to get grain size distributions [*Masch and Denny*, 1966]. Although several methods, such as freezing the samples, exist to collect nearly undisturbed cores, it is still an extremely challenging process especially for unconsolidated sediments.

Alternative experimental methods to determine *K* require either laboratory measurements (following Darcy's law) on the core samples or more complicated procedures for in-situ experiments. In both cases, the measured values are affected by the core removal or experimentation procedure since re-sorting due to the vibration and the loss of pore water are almost unavoidable. Flowmeter tests are the most commonly used in-situ experimentation methods since they allow in-situ measurements of bulk parameter *K*. These are capable of measuring *K* averaged over an uncertain volume and have been widely used to map the hydraulic properties of aquifers. Although several existing studies demonstrate the success of flowmeter tests in mildly heterogeneous media, they also have many limitations. Beside the invasiveness, flowmeter tests are relatively slow, and capable to measure the bulk parameter for an unknown volume. Therefore, these tests can provide *K* information with a limited resolution and, are not very sensitive to low *K*.

Indirect measurement procedures also exist, and include slug tests, infiltration and tracer experiments. These methods intend to derive K distribution using other measured parameters rather than attempting to measure the actual K. Infiltration experiments based on the amount of water infiltrated through a limited surface area and only capable of providing the average K estimates for limited and generally unknown depth. Slug tests require addition or removal of a known volume of water from a designated well, with detailed measurements of the associated

changes in the water levels. Tracer experiments intend to derive a [or the] *K* distribution by measuring concentration distribution of the injected tracer. They are capable of providing the largest scale *K* distribution and may require a large amount of sampling.

Several other indirect measurements in the boreholes include well logging methods, that do not require the material removal. However, they require complementary data and an interpretation step since a known relationship between *K* and the measured parameters (i.e., resistivity, seismic velocity, gamma ray exposure) does not exist.

Geophysical methods are another set of techniques which can only provide indirect information related to *K* distribution. However, they often provide the advantage of non-invasiveness and higher resolution than the borehole based methods. The potential benefits of geophysical methods in addition to, or as replacements of, current in-situ methods are very significant. Geophysical methods can be effectively used for measuring bulk properties and mapping certain structures such as fractures, gravel beds, and clay lenses, which may have strong effects on the movement of groundwater either as preferential flow paths or as retardant barriers [*Overmeeren*, 1998; *Streich et al.*, 2006]. Innovative approaches to collect and interpret geophysical data to map these structures, can also contribute to the efforts to derive a quantitative affinity between geophysics-derived parameters and hydraulic conductivity. Besides, improvements of geophysical methods provide data for the non-invasive monitoring of pollution and remediation processes [*Brewster and Annan*, 1994; *Halihan et al.*, 2005].

In recent years, several novel borehole based approaches have emerged to delineate aquifer characteristics at higher resolution than previously possible. These approaches include insitu measurements using direct-push technology, which is a significantly faster alternative to the conventional borehole methods, especially in unconsolidated sediments. A recently developed

direct-push tool, called High Resolution *K* (HRK) tool, which couples direct-push permeameter (DPP) and direct-push injection logger (DPIL), provides cm-scale vertical resolution and partly overcomes an important obstacle related to resolution issues [*Liu et al.*, 2009]. This relatively less destructive tool involves a probe with an injection port and two pressure sensors. Water is injected through the port and the difference in back pressure is measured via pressure sensors. These backpressure measurements are then converted to relative *K* values. Surface-based geophysical methods can be used to provide complementary data to direct-push methods which give high resolution data in vertical profiles.

1.3 The MADE Site

The method developed in the context of this study was applied at the Macro Dispersion Experiment (MADE) site on the Columbus Air Force Base of Mississippi. The MADE site is a highly heterogeneous, unconfined shallow aquifer. Previous research suggests that the sediments consist of meandering fluvial deposits over braided fluvial deposits over a fine-grained sand layer inter-bedded with clay and silt [Bowling et al., 2005].

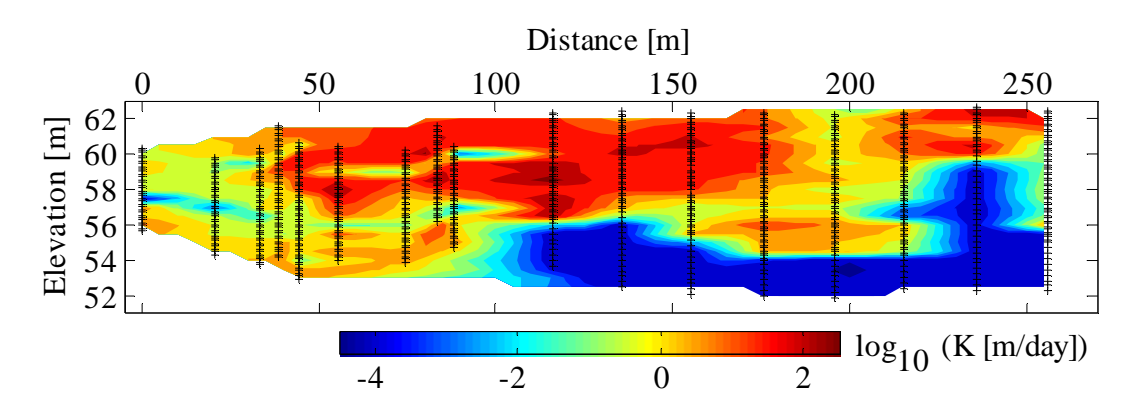


Figure 1.2 Vertically exaggerated (x5) hydraulic conductivity cross-section along A-A' using 1560 flowmeter *K* measurements [*Boggs*, 1991] (see Figure 1.4 for location).

The MADE site is one of the most heavily studied uncontaminated sites, and it represents a high level of heterogeneity in many contaminated sites [*Zheng et al.*, 2010]. It is a secure

facility that has been used to explore flow regimes in an aquifer using macro scale tracer tests and borehole measurements. The research at the site was started with measurements of ground water flow in 1984; later, the MADE-1 experiment was conducted between October 1986 and June 1988 [Boggs, 1991]. It was an extensive natural gradient experiment involving the preliminary flowmeter measurements of K. Figure 1.1 shows a cross section created using these K measurements along a transect (see Figure 1.4 for location), and the variance of ln K was calculated as 4.5. The experiment was monitored using 328 multi-level sampling wells (Figure 1.3) [Zheng et al., 2010; Boggs et al., 1992]. A mixture of several different chemicals, including bromide (in the form of calcium bromide, Cinj=2500 mg/l), pentafluorobenoic acid (PFBA, C_{inj} =400 mg/l), trifluoromethylbenzoic acid (TFBA, C_{inj} =400 mg/l), and orthofluorobenzoic acid (DFDA, C_{inj} =400 mg/l) was used as a tracer. The total mixture volume was 10.03 m 3 and groundwater extracted from the aquifer was used to prepare the mixture. The injection setup consists of five boreholes installed on a linear array with approximately 1 m separation (Figure 1.4) approximately perpendicular to the average down gradient direction. Injection was carried out through a 0.6 m screened interval between the 57.5 and 58.1 m elevations above sea level (7.4-8 m below the surface) during 48.5 hours.

Sampling was done on a snapshots basis, and the sampled area was increased through time for each snapshot. A total of 11446 samples were collected for 8 snapshots, and analyzed for the concentrations of the injected chemicals. Bromide (total injected mass of 25.0 kg) was the primary tracer due to its highly conservative nature and consistency of measured concentrations. Analysis of the measured concentrations suggested rather an interesting outcome, extremely different than what was expected. More than 20 % of the injected mass stayed around the

injection area and did not move any further than 10 meters even 500 days after the injection. In contrast, very low but detectable concentrations moved extremely fast down gradient. This interesting behavior resulted in a concentration profile with several peaks and a heavy tail which did not match the expected Gaussian shape (as predicted by advection-dispersion equation models). Thereafter, the flow behavior at the MADE site became a notorious problem for hydrologists. Two more macro-scale (MADE-2 and -3) and several smaller scale tracer tests were conducted to further investigate the issues at the site.



Figure 1.3 Multi level sampler and flowmeter well setup at the MADE site (photo courtesy: stanford.edu).

The MADE-2 experiment was conducted between June 1990 and September 1991 [Boggs, 1993]. The same injection procedure was followed but a different mixture was used as tracer including tritium (C_{inj} =55,610 pCi/ml), 14 C labeled p-xylene (C_{inj} =2770 pCi/ml), benzene (C_{inj} =68.1 mg/l), p-xylene (C_{inj} =51.5 mg/l), naphthalene (C_{inj} =7.23 mg/l), and odichlorobenzene (C_{inj} =32.8 mg/l). The total injected mixture volume was 9.7 m³ and observed

using 258 multi-level sampling wells. The sampling procedure for the second experiment was improved with additional multi-level sampling wells installed along two transects known as fences, in the vicinity of injection area. However, the recovered mass was still not comparable to the injected mass and the concentration profiles presented the same interesting behavior.

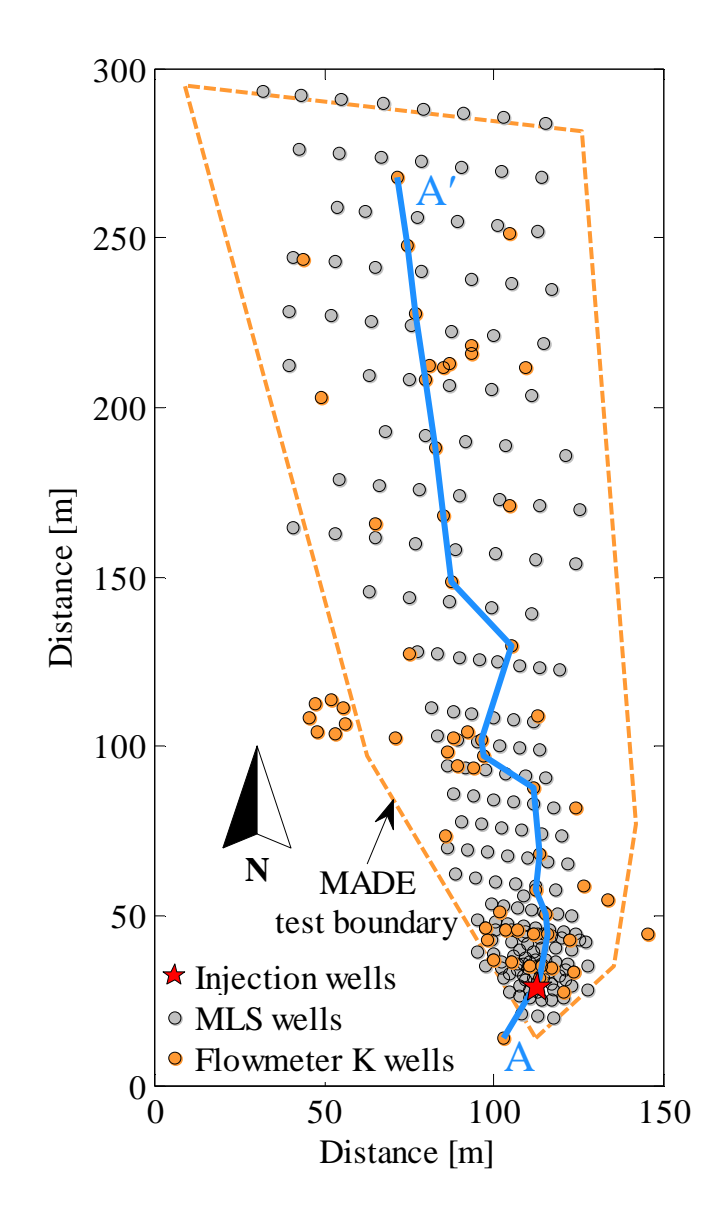


Figure 1.4 Site map showing the locations for flowmeter *K* measurements with cross-section line (A-A' in Figure 1.1), multilevel sampler wells, and test boundary.

Another attempt was made with the MADE-3 experiment. This time, the injection procedure was passive, involving a trench filled with sand and tracer mixture. The natural flow

was allowed to dissolve the tracer and transport [Boggs et al., 1995]. The natural condition of the sediments in the injection area was destroyed and homogenized irreversibly with this experiment. Several smaller scale tracer tests, including a push-pull test and an extensive core sampling procedure following blue dye injection [Liu et al., 2010], were also carried on recently.

Several approaches have been explored to simulate the flow regime at the MADE site following the experiments. Most of the earlier research concluded that the advection-dispersion equation (ADE) based approaches were not capable of reproducing the observed transport behavior at the MADE site [Zheng et al., 2010]. Modeling efforts based on ADE resulted in smooth concentration curves that were not comparable to the experiment outcomes. More exhaustive approaches followed the classic ADE method, including preferential flow paths approach, mass transfer approach between mobile and immobile domains, utilizing the fractal version of the ADE [Benson et al., 2001; Zheng and Gorelick, 2003; Harvey and Gorelick, 2000]. However, these approaches either did not include adequate parameterization due to lack of necessary data or involved naturally undeterminable features and calibration procedures. In conclusion, a successful modeling effort based on solely field data and capable of reproducing the observed transport behavior is still not available.

1.4 Methods

Geophysical methods such as electrical resistivity tomography (ERT) and ground penetrating radar (GPR) are minimally-invasive and can often provide high resolution data. They have been used for mapping hydrologically different structures and more recently for tracking fluid migration during tracer tests [*Johnson et al.*, 2007]. Borehole and surface GPR have been successfully used to map sedimentary structures [*Neal*, 2004], estimate porosity from GPR velocity fields [*Klotzsche et al.*, 2010], track Dense Non-Aqueous Phase Liquid (DNAPL) and

saline tracers [Brewster and Annan, 1994; Birken and Versteeg, 2000; Hwang et al., 2008], and monitor remediation [Halihan et al., 2005]. However, most of these studies lack comparatively high-resolution in-situ measurements of K, which in the absence of a direct relationship is necessary to determine the connection between GPR signal response and K.

GPR reflections originate at interfaces between geological materials with distinctive values of dielectric permittivity, which is directly related to water content, which for saturated media is governed by porosity. The correlation between hydraulic conductivity (which is related to porosity) and dielectric properties of media has been discussed in recent publications [*Chen et al.*, 2001; *Lambot et al.*, 2006; *Kowalsky et al.*, 2005; *Klotzsche et al.*, 2010], but no direct relationship has been established. *Morin* [2006] found an inverse relationship, which contrasts the common belief that *K* is higher for large porosities. Therefore, in this research, GPR data was used to delineate main unit boundaries and different sedimentary facies.

GPR and direct-push (DP) hydraulic conductivity data collection was completed during two field campaigns in 2008 and 2009 (Figure 1.5 and see Figure 1.6 for the locations). Multiple GPR data collection techniques were applied, with most collection using: 2D profiles, full-resolution 3D and 4D data cubes, and cross-borehole tomography (Figure 1.6). GPR data along 2D profiles were collected for broader scale site characterization and three distinct regions were selected for full resolution GPR data cubes for detailed characterization (Table 1.1). Regions to collect full resolution 3D GPR data were selected from previous tracer test sites to take advantage of existing grain size and tracer test data.



Figure 1.5 Panoramic view of the site showing the source location (metal pipes in the centerfront) and GPR data collection setup (on the right) (photo courtesy: Kaya Diker).

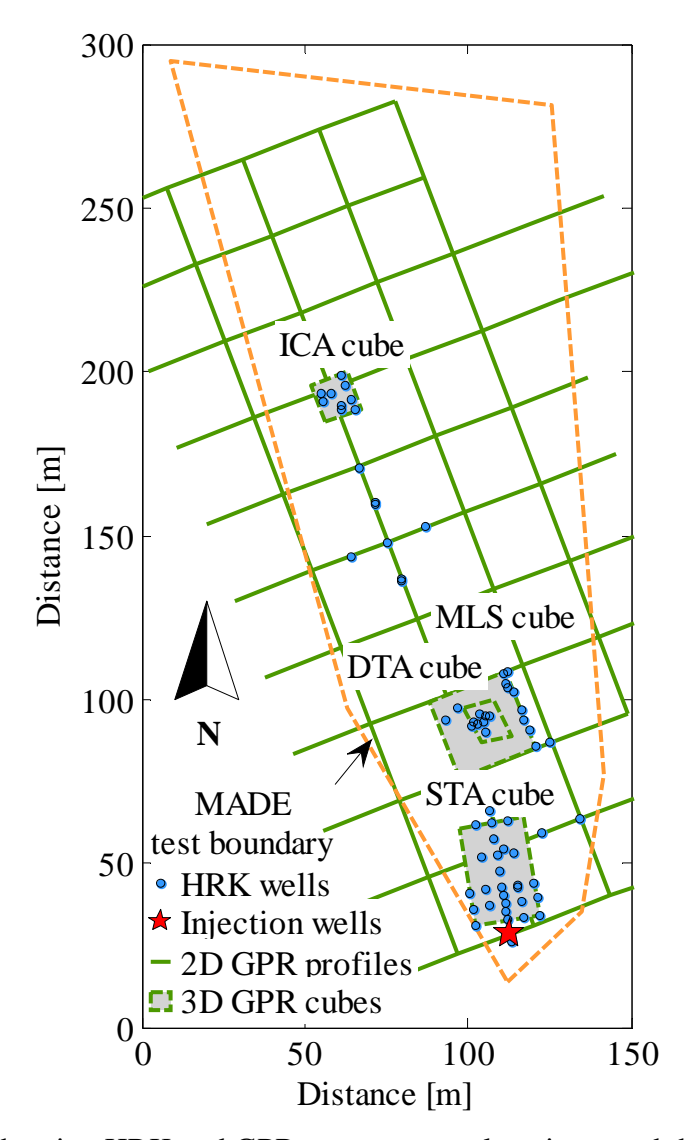


Figure 1.6 Site map showing HRK and GPR measurement locations, and the original MADE test boundary.

58 high resolution vertical *K* profiles were obtained with the new DP High Resolution *K* (HRK) probe (Figure 1.7). This tool, which was developed for rapid characterization of unconsolidated shallow aquifers [*Liu et al.*, 2009], is advanced into the subsurface while water is injected out of a small screened port located a short distance behind the tool tip. The injection rate and injection induced back pressure are recorded every 1.5 cm. The ratio of these quantities is transformed into *K* following the approach described by *Liu et al.* [2009]. Although the calibration of the transform equation is the subject of ongoing work, the spatial patterns of K, which are of greatest interest in this study, would not change with different transformation parameters.



Figure 1.7 Side view of DP High Resolution *K* (HRK) probe (photo courtesy: Kaya Diker).

Table 1.1 Inventory of collected GPR data.

Area	Size	Data Type	Frequencies
MADE site from tracer tests	250x150 m	2D profiles	50-100 MHz
Intensively Cored Area (ICA)	12x12 m	3D data cubes Vertical Radar Profiling	50-100-200-250 MHz 50-100 MHz
Multi-Level Sampler Area (MLS)	25x25 m	3D data cubes Zero Offset Profiling Multi Offset Gathering	50-100 MHz 50-100 MHz 50-100 MHz
Dipole Tracer Test Area (DTA)	5x12 m	4D data cubes Zero Offset Profiling Multi Offset Gathering	50-100 MHz 50-100 MHz 50-100 MHz
Source Trench Area (STA)	30x10 m	3D data cubes	50-100 MHz

1.5 Outline of the thesis/dissertation

This study aims to provide a novel approach to create flow-transport models solely based on field data to reproduce the outcomes of MADE-1 and -2 experiments. This introductory chapter provides the history and the technical details related to the experiments conducted at the MADE site. Below, I present a brief synopsis of the following chapters in this dissertation.

Chapter 2 presents a qualitative comparison of GPR and *K* data on which the remaining chapters are based. This chapter includes a statistical analysis of *K* data as a proof of concept. The objective of this second chapter is to investigate the potential of the geophysical data to delineate the hydrostratigraphically different units and to demonstrate the correlation between the GPR reflections and *K* data. Full-resolution 3D GPR derived facies boundaries were used to define the boundaries of different hydrostratigraphic structures. Descriptive statistics and distribution tests were then used to examine the power of subdivisions to reduce the variances of *K* distributions. This chapter shows that GPR reflections coincide with anomalies in *K* profiles

and separate units with distinct *K* characteristics. The chapter presents a new approach for building high-resolution 3D hydrostratigraphic frameworks of heterogeneous aquifers and to improve the stochastic *K* field creation procedure to better simulate transport through such highly heterogeneous aquifers.

The proof of concept is followed by Chapter 3, which introduces the quantitative and statistical analysis of HRK data along with the fractional differencing approach. The MADE site sediments possess a very complex and widely varied K distribution. Henceforth, conventional statistical approaches cannot be successfully utilized to model the K distribution. In this Chapter, I show that fractional differencing filter serves to remove the long range dependence and reveals the underlying K distribution. Fractal stochastic methods, which are not commonly used for aquifer characterization, were then employed to simulate K fields containing the naturally observed connectivity of the sedimentary structures. This chapter introduces the procedure followed to simulate fractal stochastic K fields and demonstrates the value of fractal methods as well as GPR derived hydrostratigraphy. It concludes that the use of fractal methods in combination with GPR derived facies boundaries, provides improved representations of K created using exclusively data based mixing of Gaussian fields. Chapter 3 is followed by an Appendix that presents a comparative analysis of conditional and unconditional K fields with and the effects of the hydrostratigraphic information obtained from GPR. This comparison includes flow and transport simulations to explore the best suitable method for stochastic K field generation.

Chapter 4 presents the outcomes of 3D flow transport simulations for an area (25x45 m) near the MADE1-3 injection site. This chapter builds on the statistical methods developed in Chapter 3, but are now applied in 3D. The research in this chapter is unique since it provides the

first 2D representations of simulated plumes in comparison to measured concentrations from MADE-1 experiment. For this chapter both data sets published after the experiments were revisited and reanalyzed. Resulting simulations were used to create 2D vertically integrated contour maps and 1D profiles of relative mass distribution. Amount of recovered mass is not comparable to the experimentation due to the limitations of reproducing the sampling procedure in the field. However flow and transport simulations, based on the presented approach, are significantly capable of representing the spatial extent of the observed plume as well as the multi-peak and heavy tail behavior of the observed relative mass distribution along the down gradient direction.

Chapter 5 combines the 3D flow simulations near the injection area with the GPR hydrofacies approach developed in Chapter 2 and investigates the effect of this additional piece of information on the outcomes of flow-transport simulations. This chapter demonstrates that the complementary GPR data improves the representation of tail behavior. The second part of this chapter includes a comparative analysis for simulated plumes for several different scenarios including: use of flowmeter *K* data, a transient flow scheme, and changing densities of HRK profiles. This part of the study showed that: (1) flowmeter *K* data alone is not sufficient to create *K* fields to reproduce the plume behavior successfully, (2) no significant difference exist between steady state and transient flow schemes in simulated plume shape and characteristics, (3) HRK profiles have a significant effect on the simulated plume.

Finally, Chapter 6 lays out a synthesis of the previous chapters and tabulates the conclusions of this research.

REFERENCES

REFERENCES

- Benson, D. A., R. Schumer, M. M. Meerschaert, & S. W Wheatcraft (2001), Fractional dispersion, Lévy motion, and the MADE tracer tests. Transport in Porous Media, 42(1908), 211-240.
- Boggs, J. M. (1993), Database for the second Macrodispersion Experiment (MADE-2). EPRI Topical Rep. TR-10 (Vol. 2072).
- Boggs, J. M., S. C. Young, L. M. Beard, L. W. Gelhar, K. R. Rehfeldt & E. E. Adams (1992), Field study of dispersion in a heterogeneous aquifer: 1. Overview and site description. Water Resources Research, 28(12), 3281-3291. doi:10.1029/92WR01756.
- Boggs, J. M. (1991), Database for the first Macrodispersion Experiment (MADE-1).
- Boggs, J.M., J. A. Schroeder, and S. C. Young (1995), Data to support model development for natural attenuation study. Report No. WR28-2-520-197. TVA Engineering Laboratory, Tennessee Valley Authority, Norris, Tennessee.
- Bowling, J. C., A. B. Rodriguez, D. L. Harry, & C. Zheng (2005), Delineating alluvial aquifer heterogeneity using resistivity and GPR data. Ground Water, 43(6), 890-903.
- Brewster, M. L., & A. P. Annan (1994), Ground-penetrating radar monitoring of a controlled DNAPL release: 200 MHz radar. Geophysics, 59, 1211-1221.
- Birken, R., & R. Versteeg (2000), Use of four-dimensional ground penetrating radar and advanced visualization methods to determine subsurface fluid migration. Journal of Applied Geophysics, 43(2-4), 215-226. doi:10.1016/S0926-9851(99)00060-9.
- Chen, J., S. Hubbard, & Y. Rubin (2001), Estimating the hydraulic conductivity at the south oyster site from geophysical tomographic data using Bayesian Techniques based on the normal linear regression model. Water Resources Research, 37(6), 1603. doi:10.1029/2000WR900392.
- Dafflon, B., J. Irving, and W. Barrash (2011), Inversion of multiple intersecting high-resolution crosshole GPR profiles for hydrological characterization at the Boise Hydrogeophysical Research Site. Journal of Applied Geophysics, 73.4: 305-314.
- Dagan, G. (1989), Flow and transport in porous formations. Springer-Verlag GmbH & Co. KG.
- Garabedian, S. P., D. R. LeBlanc, L. W. Gelhar, and M. A. Celia (1991), Large-scale natural gradient tracer test in sand and gravel, Cape Cod, Massachusetts: 2. Analysis of spatial moments for a nonreactive tracer. Water Resources Research, 27: 911–924.
- Gómez-Hernádez, J. J., and X. -H. Wen (1998), To be or not to be multi-Gaussian? A reflection on stochastic hydrogeology, Adv. Water Resour. 21(1), 47–61.

- Freyberg, D. L. (1986), A natural gradient experiment on solute transport in a sand aquifer: 2. Spatial moments and the advection and dispersion of nonreactive tracers. Water Resources Research, 22: 2031–2046.
- Halihan, T., S. Paxton, I. Graham, T. Fenstemaker, & M. Riley (2005), Post-remediation evaluation of a LNAPL site using electrical resistivity imaging. Journal of Environmental Monitoring □: JEM, 7(4), 283-287. doi:10.1039/b416484a.
- Harvey, C., & S. M. Gorelick (2000), Rate-limited mass transfer or macrodispersion: which dominates plume evolution at the Macrodispersion Experiment (MADE) site? Water Resources Research, 36(3), 637–650. American Geophysical Union.
- Hyndman, D. W., M. J. Dybas, L. Forney, R. Heine, T. Mayottee, M. S. Phanikumar, G. Tatara, J. Tiedje, T. Voice, R. Wallace, D. Wiggert, X. Zhao, and C. S. Criddle (2000), Hydraulic characterization and design of a full-scale biocurtain. Ground Water, 38: 462–474.
- Hwang, Y. K., A. Endres, S. D. Piggott, & B. L. Parker (2008), Long-term ground penetrating radar monitoring of a small volume DNAPL release in a natural groundwater flow field. Journal of Contaminant Hydrology, 97(1-2), 1-12. doi:10.1016/j.jconhyd.2007.11.004.
- Illman, W. A., J. Zhu, A. J. Craig, and D. Yin (2010), Comparison of aquifer characterization approaches through steady state groundwater model validation: A controlled laboratory sandbox study, Water Resources Research, 46, W04502, doi:10.1029/2009WR007745.
- Johnson, T. C., P. S. Routh, W. Barrash, & M. D. Knoll (2007), A field comparison of Fresnel zone and ray-based GPR attenuation-difference tomography for time-lapse imaging of electrically anomalous tracer or contaminant plumes. Geophysics, 72(2), G21-G29. doi:10.1190/1.2431638.
- Kabala, Z. J. (1993), The dipole flow test: A new single-borehole test for aquifer characterization, Water Resources Research, 29(1), 99–107, doi:10.1029/92WR01820.
- Klotzsche, A., J. van der Kruk, G. Meles, J. Doetsch, H. Maurer, & N. Linde (2010), Full-waveform inversion of crosshole ground penetrating radar data to characterize a gravel aquifer close to the Thur River, Switzerland. Ground Penetrating Radar (GPR), 2010 13th International Conference on (pp. 1–5). IEEE.
- Kowalsky, M. B., S. Finsterle, J. Peterson, S. S. Hubbard, Y. Rubin, E. Majer, A. Ward, et al. (2005), Estimation of field-scale soil hydraulic and dielectric parameters through joint inversion of GPR and hydrological data. Water Resources Research, 41(11), 1-19. doi:10.1029/2005WR004237.
- Lambot, S., E. C. Slob, M. Vanclooster, & H. Vereecken (2006), Closed loop GPR data inversion for soil hydraulic and electric property determination. Geophysical Research Letters, 33(21), 1-5. doi:10.1029/2006GL027906.
- LeBlanc, D. R., S. P.Garabedian, K. M.Hess, L. W.Gelhar, R. D.Quadri, K. G.Stollenwerk, and W. W. Wood (1991), Large-scale natural gradient tracer test in sand and gravel, Cape Cod,

- Massachusetts: 1. Experimental design and observed tracer movement. Water Resources Research, 27: 895–910.
- Liu, G., J. J. Butler Jr, G. C. Bohling, E. Reboulet, S. Knobbe, & D. W. Hyndman (2009), A new method for high-resolution characterization of hydraulic conductivity. Water Resources Research, 45(8), W08202. American Geophysical Union.
- Liu, G., C. Zheng, G. R. Tick, J. J. Butler Jr., and S. M. Gorelick (2010), Relative importance of dispersion and rate-limited mass transfer in highly heterogeneous porous media: analysis of a new tracer test at the Macrodispersion Experiment (MADE) site. Water Resources Research 46: W03524. doi:10.1029/2009WR008430.
- Mackay, D. M., D. L. Freyberg, P. V. Roberts, and J. A. Cherry (1986), A natural gradient experiment on solute transport in a sand aquifer: 1. Approach and overview of plume movement. Water Resources Research, 22: 2017–2029.
- Masch, Frank D., and Denny, Kleber J. (1966), Grain size distribution and its effect on the permeability of unconsolidated sands. Water Resources Research, 2.4: 665-677.
- Morin, R. (2006), Negative correlation between porosity and hydraulic conductivity in sand-and-gravel aquifers at Cape Cod, Massachusetts, USA. Journal of Hydrology, 316(1-4), 43-52. doi:10.1016/j.jhydrol.2005.04.013.
- Neal, A. (2004), Ground-penetrating radar and its use in sedimentology: principles, problems and progress. Earth-Science Reviews, 66(3-4), 261-330. doi:10.1016/j.earscirev.2004.01.004.
- Van Overmeeren, R. A. (1998), Radar facies of unconsolidated sediments in The Netherlands: A radar stratigraphy interpretation method for hydrogeology. Journal of Applied Geophysics, 40.1: 1-18.
- Phanikumar, M. S., D. W. Hyndman, X. Zhao, and M. Dybas (2005), A three-dimensional model of microbial transport and biodegradation at the Schoolcraft, Michigan site. Water Resources Research, 41: W05011.
- Streich, R., J. Van Der Kruk, and A. G. Green (2006), Three-dimensional multicomponent georadar imaging of sedimentary structures. Near Surface Geophysics, 4.1: 39-48.
- Zheng, C., M. Bianchi, & S. M. Gorelick (2010), Lessons Learned from 25 Years of Research at the MADE Site. Ground Water, 1-14. doi:10.1111/j.1745-6584.2010.00753.x.
- Zheng, C., & S. M. Gorelick (2003), Analysis of solute transport in flow fields influenced by preferential flowpaths at the decimeter scale. Ground Water, 41(2), 142-155.

Chapter 2

Hydrostratigraphic analysis of the MADE site with full-resolution GPR and direct-push hydraulic profiling

Abstract

Full-resolution 3D Ground-Penetrating Radar (GPR) data were combined with high-resolution hydraulic conductivity (*K*) data from vertical Direct-Push (DP) profiles to characterize a portion of the highly heterogeneous MAcro Dispersion Experiment (MADE) site. This is an important first step to better understand the influence of aquifer heterogeneities on observed anomalous transport. Statistical evaluation of DP data indicates non-normal distributions that have much higher similarity within each GPR facies than between facies. The analysis of GPR and DP data provides high-resolution estimates of the 3D geometry of hydrostratigraphic zones, which can then be populated with stochastic *K* fields. The lack of such estimates has been a significant limitation for testing and parameterizing a range of novel transport theories at sites where the traditional advection-dispersion model has proven inadequate.

This chapter is based on Dogan, M., R. L. Van Dam, G. C. Bohling, J. J. Butler Jr., and D. W. Hyndman (2011), Hydrostratigraphic analysis of the MADE site with full-resolution GPR and direct-push hydraulic profiling, Geophysical Research Letters, 38, L06405, doi:10.1029/2010GL046439.

2.1 Introduction

The transport of solutes through an aquifer is primarily controlled by medium properties, in particular the spatial distribution of hydraulic conductivity (K) [e.g., Gelhar, 1993; Fleckenstein and Fogg, 2008]. Studies of mildly heterogeneous aquifers have demonstrated that solute transport can be reasonably modeled using the classical advection-dispersion equation (ADE) with limited K data [e.g., Mackay et al., 1986; Hess et al., 1992], and that hydrostratigraphic analysis of core material improves transport predictions [e.g., Phanikumar et al., 2005]. In contrast, studies in highly heterogeneous aquifers have shown that the classic ADEbased approach with K data from conventional field methods does not accurately simulate transport in such systems [e.g., Eggleston and Rojstaczer, 1998; Whittaker and Teutsch, 1999]. Indeed, three large-scale natural gradient tracer experiments performed at the MAcro Dispersion Experiment (MADE) site (Figure 2.1) on Columbus Air Force Base, Mississippi, USA, displayed pronounced non-Gaussian behavior [Boggs et al., 1992; Zheng, 2006]. The MADE aquifer consists of highly heterogeneous unconsolidated fluvial sediments (ln K variance = 4.5 from borehole flowmeter data [Rehfeldt et al., 1992]), underlain by a clay aquitard at ~12 m depth. Bowling et al. [2005] used 2D Ground-Penetrating Radar (GPR) lines and information from a nearby quarry to identify three main facies above the aquitard: a meandering fluvial system over a braided fluvial deposit over a fine-grained sand interbedded with clay and silt.

Several approaches have been proposed for simulating the observed tracer transport at MADE by incorporating preferential flow paths [e.g., *Zheng and Gorelick*, 2003] or mass transfer between mobile and immobile domains [e.g., *Harvey and Gorelick*, 2000] into the ADE, or by using a fractional form of the ADE [e.g., *Benson et al.*, 2001]. Although these approaches may provide reasonable representations of the average plume behavior, they do not accurately

replicate concentration histories at observation wells nor can they be parameterized using available data. Novel high-resolution characterization methods, however, may provide the necessary subsurface data to greatly improve traditional transport simulations in such highly heterogeneous systems and aid in the assessment of alternative transport theories.

GPR is a common noninvasive method for high-resolution exploration of spatial variability in the shallow subsurface [e.g., *Jol*, 2009], but it does not provide direct information about *K* [*Hubbard and Rubin*, 2000]. Previous efforts to use GPR to improve flow and transport models have combined GPR facies analysis with modeled *K* fields and stochastic simulations [*Rauber et al.*, 1998; *Moysey et al.*, 2003; *Ezzy et al.*, 2006; *Engdahl et al.*, 2010]. Such studies have not directly combined surface 3D GPR data with high-resolution in-situ *K* estimates to develop hydrofacies models for heterogeneous aquifers, which is the focus of this paper.

In this paper, we present results of a recent field demonstration at the MADE site where full-resolution 3D GPR and cm-scale Direct-Push (DP) K data were collected. Following a description of the approach and methods, we discuss the general reflection patterns in the GPR data cubes. We then present the results of a GPR facies analysis for a 2D plane where four DP K profiles were obtained. Following a qualitative comparison of these collocated data sets, we present the results of statistical tests to evaluate whether GPR facies are also distinct hydrostratigraphic units. The results of this field demonstration indicate that the combination of methods presented here is a promising approach for characterizing 3D hydrostratigraphic structures. These structures, which can then be populated by stochastic simulation of K fields, can serve as the basis for flow and transport models of highly heterogeneous aquifers, such as at the MADE site.

2.2 Methods

GPR is an excellent method to image shallow sedimentary structures because the signal response is controlled by textural properties [*Neal*, 2004]. In saturated low-loss media, such as sand and gravel, the variable most directly linked to GPR signal propagation and reflection is porosity, which is governed by sediment characteristics such as grain size, sorting, and packing. GPR has traditionally been used for 2D and pseudo-3D characterization, but recent studies have demonstrated the added value of full-resolution data, with less than quarter wavelength (λ) sampling for in- and cross-line directions [*Grasmueck et al.*, 2005]. Full-resolution GPR maximizes the potential to characterize 3D subsurface structures. Its vertical resolution depends on signal wavelengths, which depend on by frequencies of propagating waves and dielectric permittivities of the medium. For example, vertical resolution is ~0.145 m ($1/4 \lambda$) for 100 MHz signals in saturated sediments with a relative dielectric permittivity of 23 (EM velocity ~0.058 m/ns). The lateral resolution depends on the Fresnel zone, which gets larger with increasing depth and decreasing frequency.

We used 2D GPR lines to characterize the stratigraphy over the region where three natural-gradient tracer experiments [*Zheng*, 2006] were conducted. We then collected full-resolution 3D GPR data around the Intensively Cored Area (ICA – Figure 2.1a) where a single-well, push-pull tracer test was recently performed [*Liu et al.*, 2010]. A total of 3.8 km of GPR lines were collected in the ICA cube using 50 and 100 MHz antennae, with step sizes of 0.2 and 0.1 m, respectively, which is less than the $1/4 \lambda$ required spacing. Line spacing was equal to step size, thus forming a regular grid of GPR traces. Data were collected using a sampling interval of 800 ps over 550 and 400 ns time windows, and 16 and 32 stacks for the two frequencies, respectively. Accurate positioning was achieved using guidance ropes and odometer-wheel

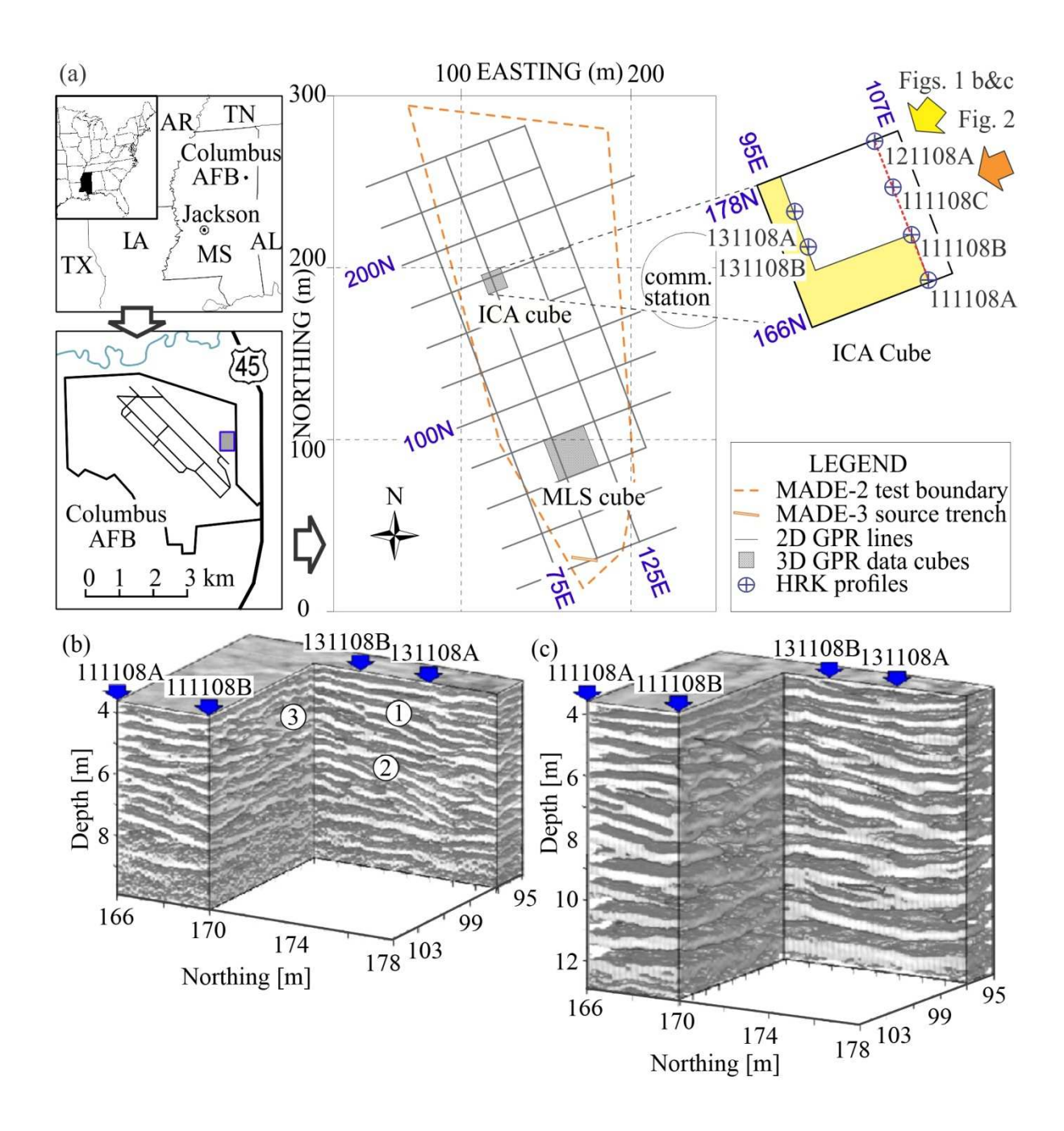


Figure 2.1 (a) Map of the MADE site on Columbus Air Force Base (AFB) with GPR measurement lines. The GPR survey coordinates are shown in blue. The blowup of the ICA cube (144 m²) shows DP sites and locations of the 3D GPR cubes in Figures 2.1b and c (yellow shaded area) and the profile in Figure 2.2 (red dashed line); viewing angles are indicated with arrows in corresponding colors. Full-resolution 3D GPR data cubes at (b) 100 MHz and (c) 50 MHz are shown with no vertical exaggeration. An envelope was used to render negative amplitudes transparent; number labels in Figure 2.1b are discussed in the text.

triggering. All GPR data were collected with a Sensors and Software pulseEKKO 100 system (1000V transmitter) at night and on weekends to avoid flight-time interference with a communication station adjacent to the site (Figure 2.1a).

GPR data were processed with a background removal filter (dewow, 14 and 8 ns for 50 and 100 MHz, respectively) followed by a band-pass filter to eliminate high-frequency noise. Static corrections were then applied to flatten the reflection from the top of the saturated zone, as the measured water table gradient was only ~0.0003 (3.3 cm over 111 m). The reflection times for the saturated zone were converted to depths based on the average measured velocity of 0.058 m/ns, from CMP and cross-borehole data.

A GPR facies approach [Van Overmeeren, 1998] was used to identify zones with distinct reflection characteristics. The primary criteria used to define GPR facies were reflection terminations, dip angle, amplitude, and continuity in 3D. We then compared GPR facies with high-resolution vertical K profiles that were obtained with the new DP High-Resolution K (HRK) probe. This tool, which was developed for rapid characterization of unconsolidated shallow aquifers [Liu et al., 2009], is advanced into the subsurface while water is injected out of a small screened port located a short distance behind the tool tip. The injection rate and injection-induced back pressure are recorded every 1.5 cm. The ratio of these quantities is transformed into K following the approach described in Liu et al. [2009]. Although the calibration of the transform equation is the subject of ongoing work, the spatial patterns of K, which are of greatest interest in this study, would not change with different transformation parameters. We used the Kolmogorov-Smirnov (K-S) test and box plots to evaluate differences among K distributions for different GPR facies and layers.

26

2.3 Results

Cutouts of the 100 and 50 MHz GPR data, with 10 and 12 m of signal penetration, respectively, clearly image the details of 3D structures (Figures 2.1b and c). The 100 MHz north-south oriented cut at 97 m East shows two ~2 m thick packages with northward dipping reflections between 4 and 8 m depth (① and ② in Figure 2.1b). These structures likely represent large-scale clinoforms associated with channel bar migration. This interpretation is corroborated by a reflection pattern along the perpendicular cut at 170 m North that resembles trough cross-stratification (③ in Figure 2.1b). The GPR reflections from the deepest portion of the cube are dominated by sub-horizontal continuous reflectors, but the signal is notably attenuated for the 100 MHz data. The 50 MHz data, which depict the same dipping clinoforms, have reasonable signal strength to the top of the clay aquitard (Figure 2.1c).

We conducted facies analysis across a transect at 105 m East (Figure 2.2), where the general reflection pattern is comparable to the plane at 97 m East. For this analysis, 100 MHz data were used from the water table to 8 m, and 50 MHz data were used below 9 m. The average data from both frequencies were used between 8 and 9 m depth (Figure 2.2a), since picks from both were consistent. To define the spatial distribution of GPR stratigraphy, we developed an algorithm for automated picking of peak amplitudes and identification of laterally continuous reflections (Figure 2.2b). Decisions on how reflections connect and terminate were aided by 3D analysis of the data. Using the procedure outlined earlier, the GPR data were separated into four GPR facies (Figure 2.2b). Facies A (green) consists of sub-horizontal reflections, and can be divided into two sub-facies those appear to be separated by an erosional surface. The underlying Facies B (brown) contains the most notable clinoform sets, and these can again be divided into

two sub-facies. The lowermost two facies are characterized by laterally continuous sub-horizontal reflections. Facies C (blue) has several internal clinoform structures (based on 3D analysis of the GPR data) and gently dipping bounding surfaces; Facies D (tan) has primarily horizontal reflections.

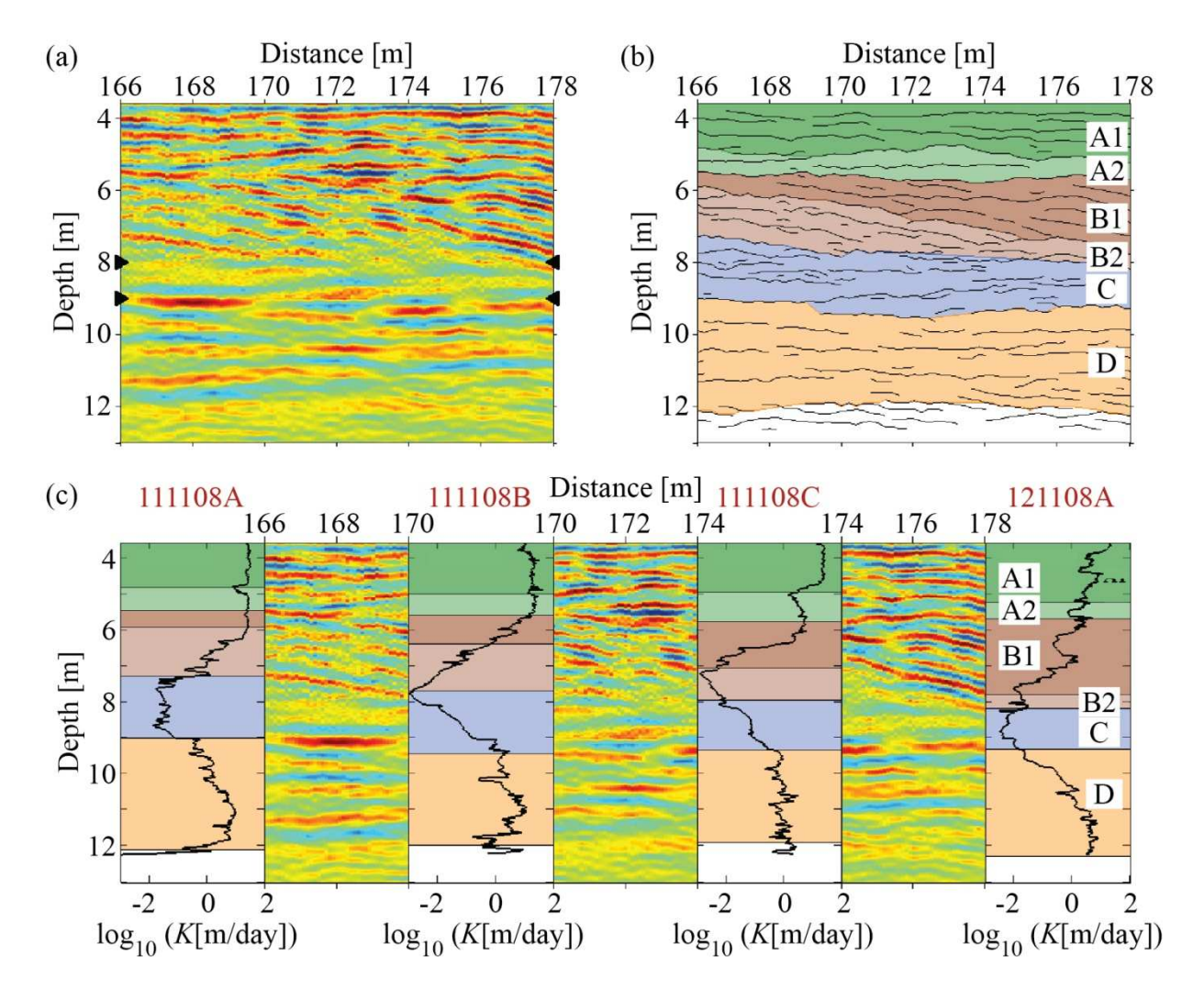


Figure 2.2 Interpretation of GPR and HRK data at line 105E (see Figure 2.1 for location). (a) GPR profile with red (positive) to blue (negative) amplitude scale using combined 100 MHz and 50 MHz data; black triangles indicate the zone where the two data sets were averaged. In addition to processing mentioned in the text, these data were plotted with an energy decay gain. (b) Continuous reflections identified using an automated picking algorithm and interpreted GPR facies (color shaded). (c) Qualitative interpretation of GPR facies with HRK data; facies boundaries are marked by horizontal lines.

Figure 2.2c presents a qualitative comparison of the GPR data and the HRK profiles along this transect. The GPR data show good correlation with the HRK profiles, as is evident from numerous small-scale anomalies that coincide with GPR reflections. In addition, GPR facies are consistent with the main *K* zones across the interpreted portion of the aquifer. Facies A has generally high *K* values, consistent with coarse-grained sediments. The relatively constant *K* values in Facies A in profiles 111108A-C reflect an upper HRK measurement threshold of roughly 10 m/d; the actual *K* values are likely higher and more variable than indicated. In the zone with prominent clinoforms, Facies B shows declining *K* with depth. Facies C shows constant to increasing conductivities with depth, whereas Facies D is characterized by generally high *K* values. There is a clear transition into the low-*K* aquitard at the bottom of HRK log 111108A (Figure 2.2c); in other logs, DP probe advancement was halted at the top of the clay.

The observations from this qualitative evaluation suggest that GPR and HRK methods can be used in tandem for high-resolution hydrostratigraphic analysis (Figure 2.3a). To evaluate this possibility quantitatively, we statistically analyzed the *K* data within GPR facies, sub-facies, and layers. Boxplots in Figures 2.3b-e visualize the descriptive statistics of the *K* data for GPR facies, sub-facies, and layers (collectively called 'segments'), respectively. One-sample K-S tests with 95% confidence intervals (CI) rejected the null-hypothesis that the *K* data from each segment have a log-normal distribution (see Table A2.1 of the appendix); therefore, the common assumption that *K* distributions are log-normal is not valid for these data.

To evaluate differences in *K* distributions, we used two-sample K-S tests with 95% CI.

These tests show that the distribution of *K* data for each of the four GPR facies is distinct (see

Table A2.2 of the Appendix). Similar K-S tests were used to test the difference of *K* distributions

between adjacent segments. These tests show that all adjacent layers as well as sub-facies/facies

have statistically distinct distributions of K (see Table A2.2 of the Appendix). Although this analysis suggests that the individual GPR facies and layers can be translated into statistically distinct hydrofacies, it does not indicate that both are necessarily equivalent. When the K data are separated by individual HRK profiles in a plot of mean versus variance, the between-profile variation in $\log K$ means for each facies is generally significantly smaller than the between-facies variation (see Figure A2.4a of the Appendix). There is, however, considerable overlap between the mean $\log K$ values for Facies B and C, which is expected since they have opposite trends of K with depth. Indeed, a plot of mean $\log K$ versus the slope of $\log K$ values with depth in each facies clearly separates the facies into clusters (see Figure A2.4b of the Appendix). Figure A2.4a also shows that the variance of $\log K$ is low for Facies A (affected by K truncation discussed earlier) and D but higher for Facies B and C, which we argue is related to the depositional environment.

Modeling of flow and transport through heterogeneous aquifers would greatly benefit from detailed characterization of *K*. Figure 2.3f demonstrates that as the aquifer is split into facies, sub-facies, and layers based on our stratigraphic analysis of full-resolution GPR data, the total variance in *K* is drastically reduced. Most of this reduction occurs in the first two splits into facies and sub-facies. Therefore, subdivision into layers may not be required to develop realistic 3D *K* fields at this site. A wide range of stochastic methods can be used to distribute the *K* data through facies/sub-facies shown in Figure 2.3a. Although a stochastic *K* field could be developed for all DP data shown in Figure 2.3a, it would clearly not be possible to fully capture the geometry of the GPR stratigraphy based on the *K* data alone. The value of separating the cube into facies, sub-facies or layers (Figure 2.3f) can then be quantified using simulations of tracer tests through the stochastically derived *K* fields.

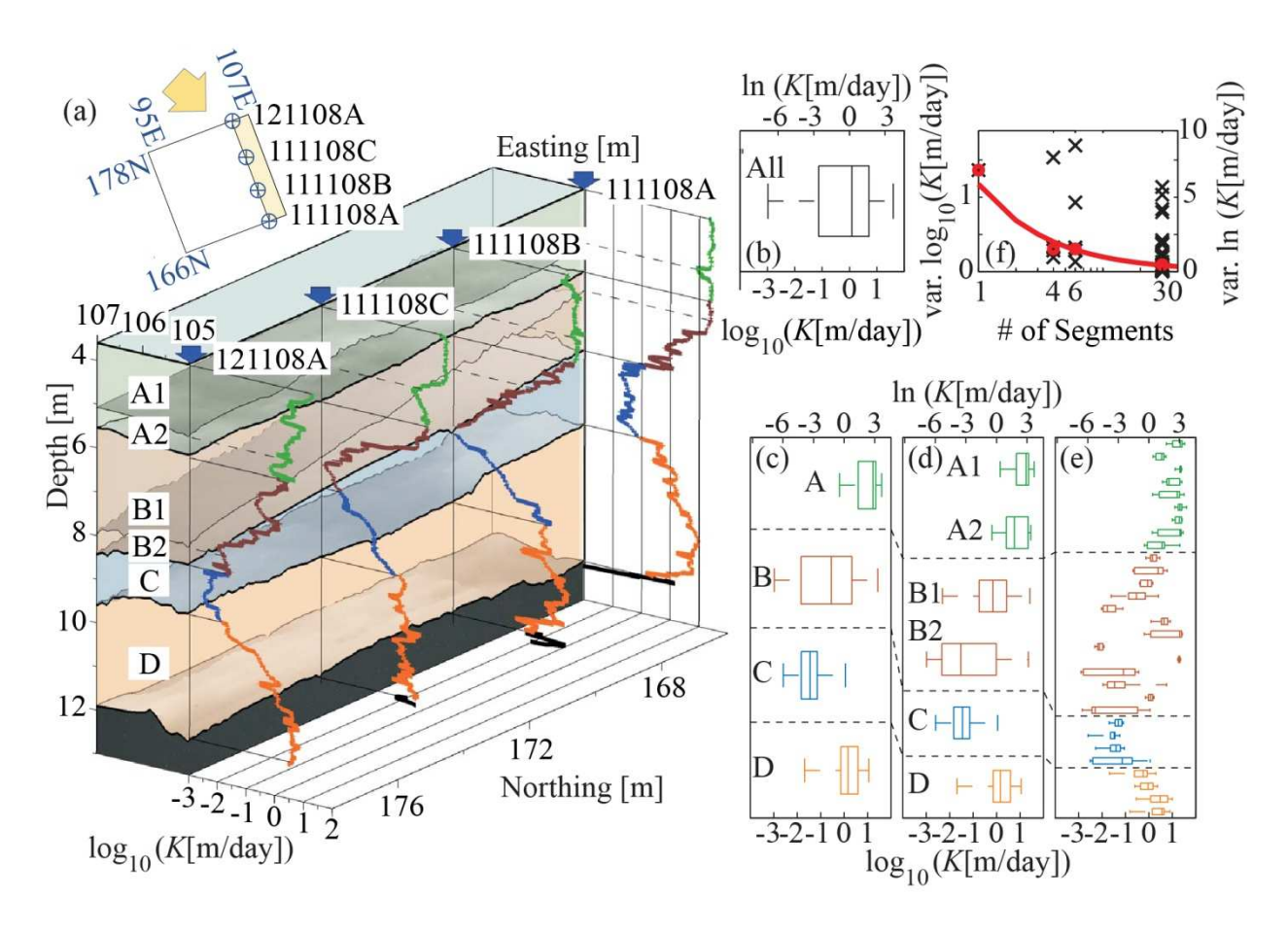


Figure 2.3 (a) 3D GPR facies boundaries (shaded to visualize topography) with collocated DP HRK profiles. Descriptive statistics of these *K* data for (b) all saturated material above the aquitard, (c) GPR facies, (d) sub-facies, and (e) layers. Box plots show the sample median, interquartile range, and positions of extreme values. (f) Variance of $\log_{10} K$ and $\ln K$ values for the data in Figures 2.3b–2.3e, respectively. The red line is a power fit through the medians of the variance values for each group (horizontal axis in log scale).

2.4 Conclusions

Accurate predictions of transport through highly heterogeneous aquifers would greatly benefit from a method to characterize the detailed structure of aquifers; this would be an important first step to populate 3D K fields with high vertical and horizontal resolution. Recently developed DP methods can provide high-resolution K (HRK) data in vertical profiles, yet they cannot provide sufficient spatial density to establish lateral connectivity. In this paper, we present the first comparison of full-resolution 3D GPR and HRK data to develop high-resolution

hydrofacies for highly heterogeneous sediments. Four GPR facies that were identified at the MADE site were determined to be distinct hydrofacies based on statistical analysis of several collocated HRK profile data. The division of these facies into smaller segments (sub-facies, layers) results in zones with lower variance in *K*. These zones can then be used to generate stochastic fields with less uncertainty than previously possible.

We found good agreement between full-resolution GPR stratigraphy and HRK profiles, thus forming a solid foundation for hydrostratigraphic characterization of this site. Our approach provides an opportunity to reconstruct 3D subsurface structures with their correct geometries and hydrologic attributes. The strong connection between the HRK data and GPR facies indicates that at many sites, a 3D *K* field could be generated using GPR data tied to a few HRK profiles. Clearly, as facies change character laterally, additional HRK profiles are needed to intercept these facies and to capture a representative distribution of *K* values.

It should be noted that the approach presented in this paper is not without limitations. The vertical and lateral resolution of GPR data is finite, and reduces with increasing depth. Limiting the variance of *K* within hydrofacies units and layers nevertheless provides the basis for better-constrained stochastic fields for solute transport simulations. In future research, the hydrofacies model described here will be used to test a range of emerging transport theories.

2.5 Acknowledgments

This work was supported by grants from NSF (EAR-0738938 and EAR-0738955); any opinions, findings, and conclusions or recommendations expressed are those of the authors and do not necessarily reflect the views of the NSF. Acknowledgment is made to the Donors of the American Chemical Society Petroleum Research Fund for partial support of this research (PRF-48515-G8). We thank G. Tick, K. Diker, E. Reboulet, S. Knobbe, U. Schneidewind, T.

Viencken, and K. Singha for field support, C. Zheng, P. Dietrich, G. Liu, and M. Meerschaert for insightful discussions, K. Hubbard and Geoprobe Systems for equipment loans, and S. Reed and Columbus AFB personnel for logistical support. Anonymous reviewers are acknowledged for their constructive comments and suggestions.

APPENDIX

Stratigraphic analysis of full-resolution ground-penetrating radar (GPR) data at the MAcro Dispersion Experiment (MADE) aquifer in Mississippi identified 4 radar facies, 2 of which can be subdivided in sub-facies, and 30 individual layers (collectively called 'segments'). In two tables, we present statistical analyses of hydraulic conductivity (*K*) data obtained with the HRK tool for these facies and layers. For each facies- and layer boundary in these tables, data from a transition zone with 1/4 wavelength of the GPR frequency (1/8 wavelength on top and bottom) was excluded from the analysis.

A one-sample Kolmogorov-Smirnov (K-S) test was used to check if K data in any of the segments is log-normally distributed. Probability values larger than 0.05 indicate log normal distribution for a 95% confidence interval. Combining *K* data from four HRK profiles (111108A, 111108B, 111108C, 121108A), Table A2.1 provides the number of data points and p values of the entire aquifer, the four facies (A: layers 1-9, B: layers 10-22, C: layers 23-26, D: layers 27-30), the sub-facies, and individual layers (see Figure 2.2 for location relative to GPR full-resolution data).

Table A2.2 provides the p values calculated using two-sample K-S tests with 95% confidence intervals for the statistical comparison of facies and consecutive sub-facies/layers, respectively. The null hypothesis of this test is that data sets of 2 samples come from the same continuous distribution.

Separated by facies and DP profile, Figure 2.4 presents cross plots of $\log_{10} K$ mean versus (a) variance and (b) the slopes of linear trends of the change in $\log_{10} K$ with depth.

Table A2.1 Single-sample K-S tests of four HRK profiles for facies and layers identified in full-resolution 3D GPR data (see Figures 2.1 and 2.3a for locations). Columns, "SEGMENT", name of segment (facies/sub-facies/layer), "N_SAMPLE", number of HRK measurements used, "p_FOR_LOG_K", p values for log₁₀ K using single-sample K-S test with 95% CI.

SEGMENT	N_SAMPLE	p_FOR_LOG_K
ALL_DATA	2163	3.24E-28
Facies_A	503	6.47E-134
Facies_B	533	3.76E-33
Facies_C	302	1.06E-136
Facies_D	655	1.06E-31
Facies_A1	337	9.70E-109
Facies_A2	128	8.73E-26
Facies_B1	265	1.11E-03
Facies_B2	232	1.04E-41
Facies_C	302	1.06E-136
Facies_D	655	1.06E-31
Layer_01	55	9.08E-30
Layer_02	24	1.21E-07
Layer_03	26	1.84E-18
Layer_04	22	5.39E-11
Layer_05	65	8.40E-21
Layer_06	43	1.36E-29
Layer_07	13	3.29E-09
Layer_08	38	1.40E-11
Layer_09	48	3.26E-08
Layer_10	22	1.40E-04
Layer_11	33	2.68E-02
Layer_12	12	1.44E-02
Layer_13	38	1.85E-04
Layer_14	14	1.97E-10
Layer_15	21	5.78E-08
Layer_16	33	2.86E-08
Layer_17	15	7.84E-14
Layer_18	12	1.41E-09
Layer_19	18	5.94E-08
Layer_20	36	2.06E-13
Layer_21	12	1.13E-02
Layer_22	60	8.76E-20
Layer_23	10	1.13E-07
Layer_24	22	1.12E-16
Layer_25	92	6.56E-60

Table A2.1 (cont'd)

SEGMENT	N_SAMPLE	p_FOR_LOG_K
Layer_26	64	1.16E-17
Layer_27	79	6.41E-11
Layer_28	70	1.50E-08
Layer_29	123	4.47E-12
Layer_30	155	1.94E-18

Table A2.2 Statistical comparison of K values for four identified radar facies and adjacent segments, where p values were calculated using two-sample K-S tests. Columns, "SEGMENT", names of compared consecutive segments (facies/sub-facies/layers), "p_FOR_LOG_K", p values for log₁₀ K using two-sample K-S test with 95% CI.

SEGMENT	p_FOR_LOG_K
Facies_A-B	8.06E-110
Facies_A-C	3.11E-158
Facies_A-D	5.09E-94
Facies_B-C	9.50E-44
Facies_B-D	8.80E-49
Facies_C-D	2.91E-149
Facies_A1-A2	8.67E-08
Facies_A2-B1	1.27E-21
Facies_B1-B2	4.20E-17
Facies_B2-C	1.54E-11
Facies_C-D	2.91E-149
Layer_01-02	5.32E-16
Layer_02-03	3.26E-12
Layer_03-04	5.40E-05
Layer_04-05	5.02E-02
Layer_05-06	7.84E-05
Layer_06-07	2.26E-01
Layer_07-08	1.64E-01
Layer_08-09	1.97E-06
Layer_09-10	6.80E-05
Layer_10-11	2.39E-03
Layer_11-12	1.13E-02
Layer_12-13	1.23E-03
Layer_13-14	6.34E-07

Table A2.2 (cont'd)

SEGMENT	p_FOR_LOG_K
Layer_14-15	1.54E-08
Layer_15-16	7.16E-05
Layer_16-17	2.90E-10
Layer_17-18	5.73E-07
Layer_18-19	1.88E-07
Layer_19-20	1.09E-01
Layer_20-21	4.84E-06
Layer_21-22	2.73E-06
Layer_22-23	6.31E-03
Layer_23-24	1.24E-02
Layer_24-25	3.10E-02
Layer_25-26	1.44E-07
Layer_26-27	2.22E-10
Layer_27-28	2.05E-04
Layer_28-29	7.31E-12
Layer_29-30	2.83E-03

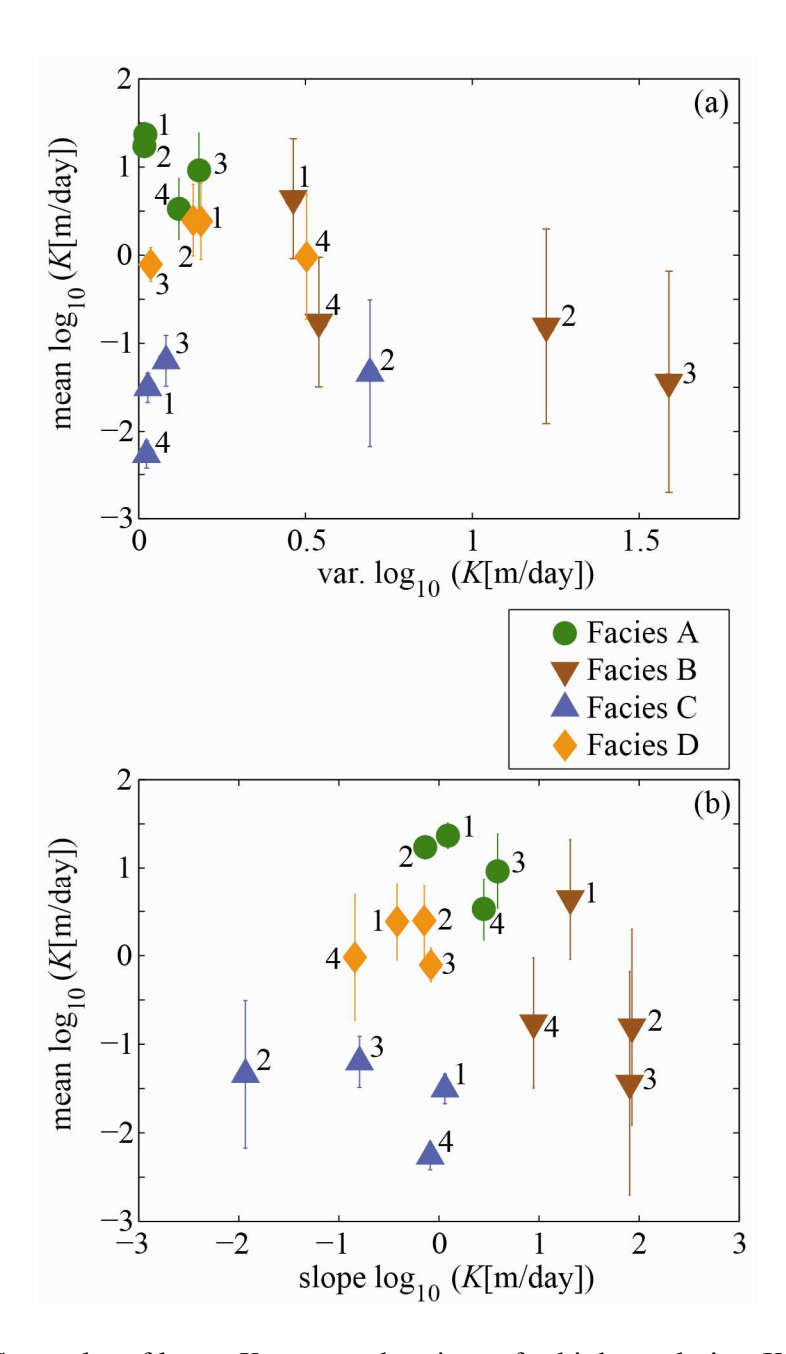


Figure A2.4 (a) Cross plot of $\log_{10} K$ mean and variance for high resolution K data from four DP profiles (see Figure 2.1 for location and Figure 2.2 for data). (b) Cross plot of $\log_{10} K$ mean and the slopes of linear trends of the change in $\log_{10} K$ with depth. In these plots, each facies is shown by a different symbol and color. The number next to each symbol indicates the DP profile (1, 2, 3, 3) and 4 represent 111108A, 111108B, 111108C, and 121108A, respectively).

REFERENCES

REFERENCES

- Benson, D. A., R. Schumer, M. M. Meerschaert, and S. W. Wheatcraft (2001), Fractional dispersion, Lévy motion and the MADE tracer tests, Transp. Porous Media, 42(1-2), 211-240.
- Boggs, J. M., and E. E. Adams (1992), Field study of dispersion in a heterogeneous aquifer: 4. Investigation of adsorption and sampling bias, Water Resources Research, 28(12), 3325-3336.
- Bowling, J. C., A. B. Rodriguez, D. L. Harry, and C. Zheng (2005), Delineating alluvial aquifer heterogeneity using resistivity and GPR data, Ground Water, 43(6), 890-903.
- Eggleston, J., and S. Rojstaczer (1998), Identification of large-scale hydraulic conductivity trends and the influence of trends on contaminant transport, Water Resources Research, 34(9), 2155-2168.
- Engdahl, N. B., G. S. Weissmann, and N. D. Bonal (2010), An integrated approach to shallow aquifer characterization: combining geophysics and geostatistics, Comput. Geosci., 14, 217-229.
- Ezzy, T. R., M. E. Cox, A. J. O'Rourke, and G. J. Huftile (2006), Groundwater flow modelling within a coastal alluvial plain setting using a high-resolution hydrofacies approach; Bells Creek plain, Australia, Hydrogeol. J., 14(5), 675-688.
- Fleckenstein, J. H., and G. E. Fogg (2008), Efficient upscaling of hydraulic conductivity in heterogeneous alluvial aquifers, Hydrogeol. J., 16(7), 1239-1250.
- Gelhar, L. W. (1993), Stochastic Subsurface Hydrology, 390 pp., Prentice-Hall, New Jersey.
- Grasmueck M., R. Weger, and H. Horstmeyer (2005), Full-resolution 3D GPR imaging. Geophysics, 70(1), K12-K19.
- Harvey, C. F., and S. M. Gorelick (2000), Rate-limited mass transfer or macrodispersion: Which dominates plume evolution at the Macrodispersion Experiment (MADE) site?, Water Resources Research, 36(3), 637-650.
- Hess, K. M., S. H. Wolf, and M. A. Celia (1992), Large-scale natural gradient tracer test in sand and gravel, Cape Cod, Massachusetts 3. Hydraulic conductivity variability and calculated macrodispersivities, Water Resources Research, 28(8), 2011-2027.
- Hubbard, S. S., and Rubin, Y. (2000), Hydrogeological parameter estimation using geophysical data: A review of selected techniques, J. Contam. Hydrology, 45, 3-34.
- Jol, H. M. (2009), Ground penetrating radar: Theory and Applications, 524 pp., Elsevier, Amsterdam.

- Julian, H. E., J. M. Boggs, C. Zheng, C. E. Feehley (2001), Numerical simulation of a natural gradient tracer experiment for the natural attenuation study: flow and physical transport, Ground Water, 39(4), 534-545.
- Liu, G., J. J. Butler Jr., G. C. Bohling, E. Reboulet, S. Knobbe, and D. W. Hyndman (2009), A new method for high-resolution characterization of hydraulic conductivity, Water Resources Research, 45, W08202.
- Liu, G., C. Zheng, G. R. Tick, J. J. Butler, and S. M. Gorelick (2010), Relative importance of dispersion and rate-limited mass transfer in highly heterogeneous porous media: Analysis of a new tracer test at the Macrodispersion Experiment (MADE) site, Water Resources Research, 46, W03524.
- Mackay, D. M., D. L. Freyberg, P. V. Roberts, and J. A. Cherry (1986), A natural gradient experiment on solute transport in a sand aquifer 1. Approach and overview of plume movement, Water Resources Research, 22(13), 2017-2029.
- Moysey S., J. Caers, R. Knight, and R. M. Allen-King (2003), Stochastic estimation of facies using ground penetrating radar data, Stochastic Environmental Research and Risk Assessment, 17(5), 306-318.
- Neal, A. (2004), Ground-penetrating radar and its use in sedimentology: principles, problems and progress, Earth-Sci. Rev., 66(3-4), 261-330.
- Phanikumar, M. S., D. W. Hyndman, X. Zhao, and Dybas M. J. (2005), A three-dimensional model of microbial transport and biodegradation at the Schoolcraft, Michigan, site, Water Resources Research, 41, W05011.
- Rauber, M., F. Stauffer, P. Huggenberger, and T. Dracos (1998), A numerical three-dimensional conditioned/unconditioned stochastic facies type model applied to a remediation well system, Water Resources Research, 34, 2225-2233.
- Rehfeldt, K. R., J. M. Boggs, and L. W. Gelhar (1992), Field study of dispersion in a heterogeneous aquifer 3. Geostatistical analysis of hydraulic conductivity, Water Resources Research, 28(12), 3309-3324.
- Van Overmeeren, R. A. (1998), Radar facies of unconsolidated sediments in The Netherlands: A radar stratigraphy interpretation method for hydrogeology. J. App. Geophysics, 40, 1-18.
- Whittaker, J., and G. Teutsch (1999), Numerical simulation of subsurface characterization methods: application to a natural aquifer analogue, Adv. Water Resour., 22(8), 819-829.
- Zheng, C. (2006), Accounting for aquifer heterogeneity in solute transport modeling: a case study from the macrodispersion experiment (MADE) site in Columbus, Mississippi, in Handbook of Groundwater Engineering, edited by J. W. Delleur, 18 pp., CRC Press.
- Zheng, C., and S. M. Gorelick (2003), Analysis of solute transport in flow fields influenced by preferential flow paths at the decimeter scale, Ground Water, 41(2), 142-155.

Chapter 3

Hydraulic conductivity fields: Gaussian or not?

Abstract

Hydraulic conductivity (*K*) fields are used to parameterize groundwater flow and transport models. Numerical simulations require a detailed representation of the *K* field, synthesized to interpolate between available data. Several recent studies introduced high resolution *K* data (HRK) at the MAcro Dispersion Experiment (MADE) site, and used ground-penetrating radar (GPR) to delineate the main structural features of the aquifer. This paper describes a statistical analysis of these data, and the implications for *K* field modeling alluvial aquifers. Two striking observations have emerged from this analysis. The first is that a simple fractional difference filter can have a profound effect on data histograms, organizing non-Gaussian ln *K* data into a coherent distribution. The second is that using GPR facies allows us to reproduce the significantly non-Gaussian shape seen in real HRK data profiles, using a simulated Gaussian ln *K* field in each facies. This illuminates a current controversy in the literature, between those who favor Gaussian ln *K* models, and those who observe non-Gaussian ln *K* fields. Essentially, both camps are correct, but at different scales.

This chapter is based on Meerschaert, M.M., M. Dogan, R. L. Van Dam, D. W. Hyndman, and D. A. Benson (2013), Hydraulic conductivity fields: Gaussian or not? Water Resources Research, doi:10.1002/wrcr.20376.

3.1 Introduction

Groundwater flow and transport simulations require a densely defined hydraulic conductivity (K) field to populate the model grid. Because it is not practical to collect 2-D or 3-D data at this resolution, stochastic simulation methods are commonly used to interpolate between measured data values. Stochastic K field simulation requires a statistical analysis of the available K data, to ensure that the synthesized K field resembles the data in terms of its distribution and correlation structure. The two main simulation steps are: (1) generate an uncorrelated noise field; and (2) apply an appropriate filter to impose a correlation structure. Since random number generators produce only uncorrelated noise, both steps are necessary. To parameterize the simulation model, the process is reversed: (1) apply an appropriate inverse filter to the raw data to remove the correlation; and (2) examine the filtered, uncorrelated data to determine its true underlying distribution. Unless the data is filtered properly to remove correlations, the data histogram can significantly misrepresent the underlying distribution, since a histogram of correlated data need not reflect the true underlying distribution. In this chapter, we will see a remarkable example of this simple and well-known fact.

Hydraulic conductivity data from the Macro Dispersion Experiment (MADE) site, at the Columbus Air Force Base in Mississippi, clearly show a high level of heterogeneity in hydraulic properties [Rehfeldt et al., 1992; Zinn and Harvey, 2003; Llopis-Albert and Capilla, 2009]. The site was recently revisited to obtain K measurements with much higher spatial resolution than previous measurements [Bohling et al., 2012; Liu et al., 2009]. Vertical columns (profiles) of hydraulic conductivity data were measured at approximately 1.5 cm depth increments, using a new direct-push profiling method that couples the direct-push injection logger (DPIL) and the direct-push permeameter (DPP) [Butler Jr et al., 2007; Liu et al., 2009, 2012]. This novel high-

resolution *K* (HRK) tool was advanced into the subsurface, while water was injected out of a small screened port located a short distance behind the tool tip. The injection rate, and injection-induced back pressure, were recorded every 1.5 cm, and the ratio of these quantities was then transformed into *K* estimates [*Liu et al.*, 2009]. The cm-scale spatial resolution of the resulting *K* data is orders of magnitude finer than the data considered in previous studies [*Rehfeldt et al.*, 1992; *Meerschaert et al.*, 2004; *Bohling et al.* 2012] analyzed the resulting *K* data, and compared those measurements to previous flowmeter-based *K* estimates collected at lower resolution across the same site.

A parallel data collection effort used ground- penetrating radar (GPR) to image the related sedimentary structures in the aquifer, called facies, by identifying distinct reflection characteristics, such as reflection terminations, dip angles, amplitudes, and continuity. Such GPR facies have been shown to correlate with hydrogeological units [e.g., see *Van Overmeeren*, 1998; *Heinz and Aigner*, 2003; *Schmelzbach et al.*, 2011]. Full-resolution 3D GPR data using 50 and 100 MHz antennae were obtained with step sizes (and line-spacings) of 0.2 and 0.1 m, respectively, using a Sensors and Software pulseEKKO 100 system. Data processing and analysis to extract facies boundaries was detailed in *Dogan et al.* [2011]. The map in Figure 3.1 outlines the GPR data collection site, and the location of the four HRK profiles that form the basis for our study. The ICA (Intensively Cored Area) cube was the site of a push-pull tracer test described in *Liu et al.* [2010], see also *Zheng et al.* [2011]. The MLS (Multi-Level Sampler) cube was the site of the MADE-5 tracer test reported in *Bianchi et al.* [2011].

The modeling of hydraulic conductivity fields at the MADE site has been the focus of intensive study and modeling for over twenty years. The geostatistical analysis of *Rehfeldt et al.* [1992] documented a high level of heterogeneity, indicated by the variance of 4.5 for ln *K* in

their multi-Gaussian model, as well as anisotropy, indicated by horizontal and vertical correlation scales of 12.8 m, and 1.6 m, respectively. Silliman and Wright [1988] and Rubin and Journel [1991] argued that a Gaussian model with a single covariance function cannot reproduce the preferential pathways (connected regions with the highest ln K values) observed in real aquifers. Gómez-Hernádez and Wen [1998] continued this argument against the multi-Gaussian model, and cautioned against drawing broad conclusions on the basis of one dimensional data distributions. Renard and Allard [2011] survey several methods for characterizing connectivity, and note that the multi-Gaussian model alone is often insufficient to reproduce the connectivity observed in real aquifers. Significant deviations from a Gaussian profile were noted by *Painter* [1996] and Meerschaert et al. [2004], and some alternative non-Gaussian models were proposed. Zinn and Harvey [2003] point out that even in a model with Gaussian ln K profiles, deviation from the usual multi-Gaussian model can lead to connected features. Salamon et al. [2007] discuss the non-monotone variograms in MADE ln K data, and recommend a sequential Gaussian simulation methodology with a non-monotone covariance structure, to reproduce this "hole effect." Llopis-Albert and Capilla [2009] use a gradual conditioning algorithm to produce non-Gaussian ln K fields based on flowmeter, head, and concentration data from MADE-2. This controversy between Gaussian and non-Gaussian ln K fields has profound implications for flow and transport modeling. Heavy tailed ln K distributions support novel approaches including the CTRW [Berkowitz et al., 2006], fractional ADE [Benson et al., 2013], and some related stochastic hydrology models [Cushman and Ginn, 2000; Neuman and Tartakovsky, 2009], while Gaussian ln K models are more consistent with the traditional ADE, mobile-immobile, and dualdomain models.

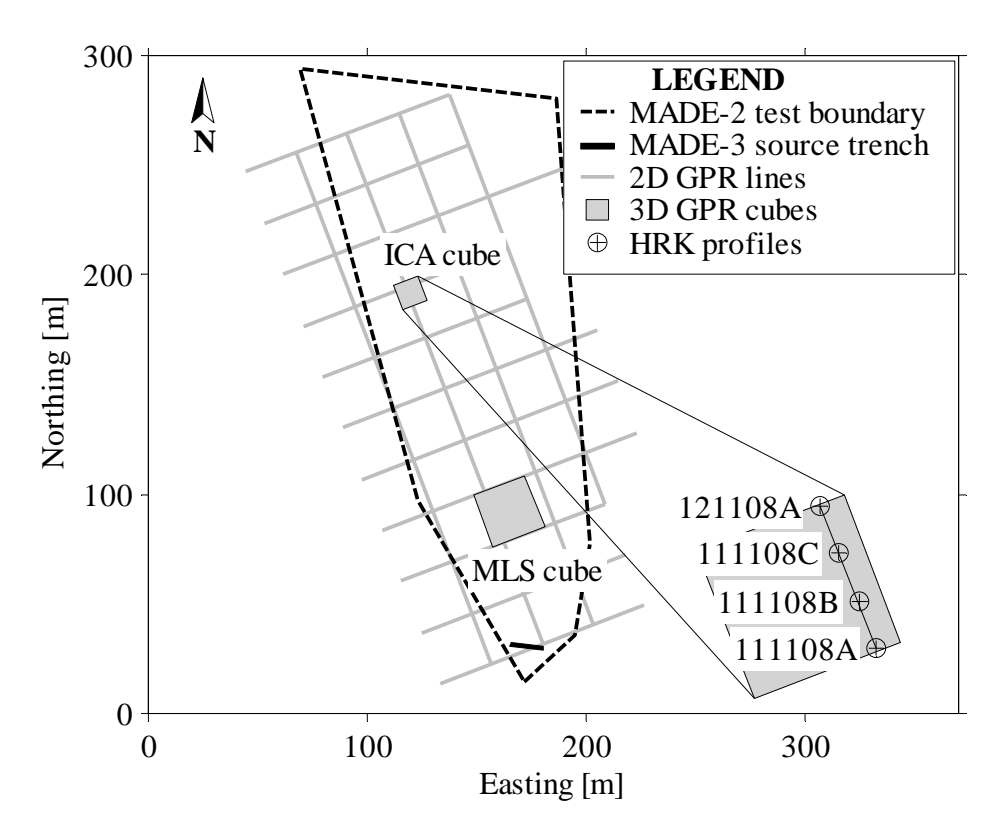


Figure 3.1 Layout of Macro Dispersion Experiment test site, showing key features of MADE experiments, as well as the locations of GPR data collected for this project. The inset of the 12×12 m ICA (Intensively Cored Area) cube shows the locations of the four HRK profiles and the 2D transect discussed in this paper.

The two main findings of this study are that: (1) a fractional difference filter can be useful to reveal the true underlying distribution of highly correlated vertical columns of HRK data; and (2) using GPR facies, a multi-Gaussian simulation method with an appropriate operator scaling correlation structure applied to each facies can reproduce the significantly non-Gaussian profiles seen in columns of filtered HRK data. There remains a significant debate in the literature between those who favor Gaussian models, and others who believe that a non-Gaussian approach is needed. In our view, both groups are correct, albeit at different scales. Within a single facies, an appropriate multi-Gaussian model can be effective, and when different facies are combined, a non-Gaussian profile with a sharper peak and a heavier tail will emerge.

3.2 Statistical analysis

Many studies have analyzed the statistical properties of low-resolution *K* data profiles; see *Meerschaert et al.* [2004] for a brief review. A typical field experiment collects *K* data at a vertical resolution of 1 – 3 m. Since the vertical resolution of the new HRK data is orders of magnitude finer, it is useful to reconsider the results of past analysis. For relatively homogeneous aquifers, it has been common to employ a log-normal distribution for *K*: the distribution of ln *K* is assumed to be normal, and aquifer heterogeneity is inferred from the variance of ln *K* [*Rehfeldt et al.*, 1992]. A more detailed analysis suggests a departure from normality, with a sharper peak and heavier tails [e.g., *Lu et al.*, 2002; *Meerschaert et al.*, 2004]. This deviation becomes more significant for aquifers that display a higher degree of heterogeneity.

Typical values for ln *K* are highly correlated, leading many researchers to employ models such as a fractional Brownian motion. The MADE site is highly heterogeneous, with ln *K* variance greater than 4.5. Several novel models have been proposed to try and capture this combination of non-Gaussian distributions and strong correlations [e.g., *Painter*, 1996; *Herrick et al.*, 2002; *Molz and Boman*, 1993; *Kohlbecker et al.*, 2006].

Figure 3.2a shows a histogram of ln *K* data from HRK profile 121108A (see map in Figure 3.1). The histogram suggests a complex underlying distribution, widely varying with several peaks, and no simple discernible shape. A fractional difference filter was applied to remove the correlations, resulting in the histogram in Figure 3.2b. The filtered data show no significant serial correlations, indicating that fractionally integrated noise is a reasonable model for this vertical column of ln *K* data. Fractional models have been applied in hydrology since pioneering work of *Hurst* [1951] on flood levels of the Nile river. In these models, observations

 X_n are related to a sequence of independent and identically distributed random variables Z_n (white noise) by the fractional difference relation

$$Z_{n} = \sum_{j=0}^{\infty} w_{j} X_{n-j}$$
 (3.1)

where the fractional binomial coefficients w_j can be computed recursively using w_n =1 and w_j = $w_{j-1}(j-1-d)/j$ for $j\ge 1$. If the underlying noise sequence Z_n is Gaussian, then the sequence X_n is a fractional Brownian motion with Hurst index H=d-1/2. See the Appendix 3.1 for more details.

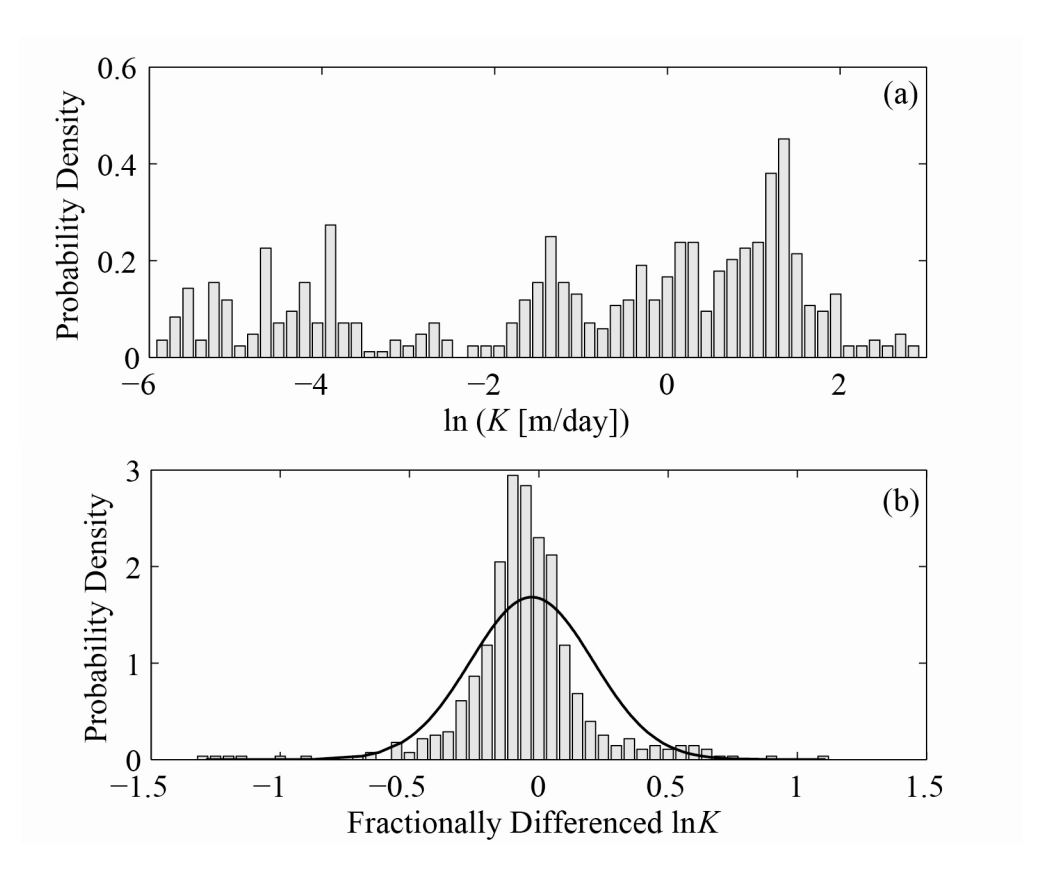


Figure 3.2 Histogram of $\ln K$ for HRK profile 121108A (see map in Figure 3.1) before (a) and after (b) applying the fractional difference filter (1) with d=0.9. The filtered data are organized into a unimodal distribution with a sharper peak and a heavier tail than the best fitting Gaussian probability density function (black line).

Figure 3.2b was obtained using a fractional difference filter with d=0.9. The parameter d was gradually increased until the autocovariance plot showed no significant correlations, see Figure 3.3. The same value of d was effective in removing correlation in all four vertical HRK columns 111108A, 111108B, 111108C, and 121108A (see Figure 3.1) that formed the basis for our study. A fractional difference filter of order d=0.89 was used in Lu et al. [2002] to remove correlations in laboratory ln K data from a vertical sandstone core; a value of d=0.9 was found suitable for a sandstone slab in Major et al. [2011]; Meerschaert et al. [2004] used d=0.74 for lower resolution ln K values from three horizontal profiles in a sandstone facies at a site in Utah.

The effect of fractional differencing on the histogram is striking. The filtered HRK data in Figure 3.2b form a coherent shape, with a sharper peak and a heavier tail than a Gaussian (the data fail the Anderson-Darling test for normality, p<0.0005. It is known that correlation can distort a histogram, but we have never seen such a clear example in real data. The fractional difference filter transforms a highly complex histogram into a form amenable to statistical modeling, by removing the correlation. This is the first major finding of our statistical analysis: A simple fractional difference filter is sufficient to capture and remove the correlation structure of a vertical $\ln K$ profile. This filter reveals the underlying noise distribution needed to design a faithful $\ln K$ field simulation.

The dramatic transformation between Figures 3.2a and 3.2b has not been observed previously, perhaps because the available data were either more homogeneous (e.g., laboratory studies of a sandstone slab) or more widely spaced (e.g., flowmeter data from field studies) than the data considered in this study. Since our data are closely spaced, many similar *K* values tend to clump together due to high correlations, creating histogram peaks. These high correlations are evident in Figure 3.3a. Mathematically, this strong correlation is a fractional integration. Since

each vertical section spans several different facies, with significantly different material properties, multiple peaks can occur in a single HRK profile. The fractional difference filters out the correlations by reversing the fractional integration.

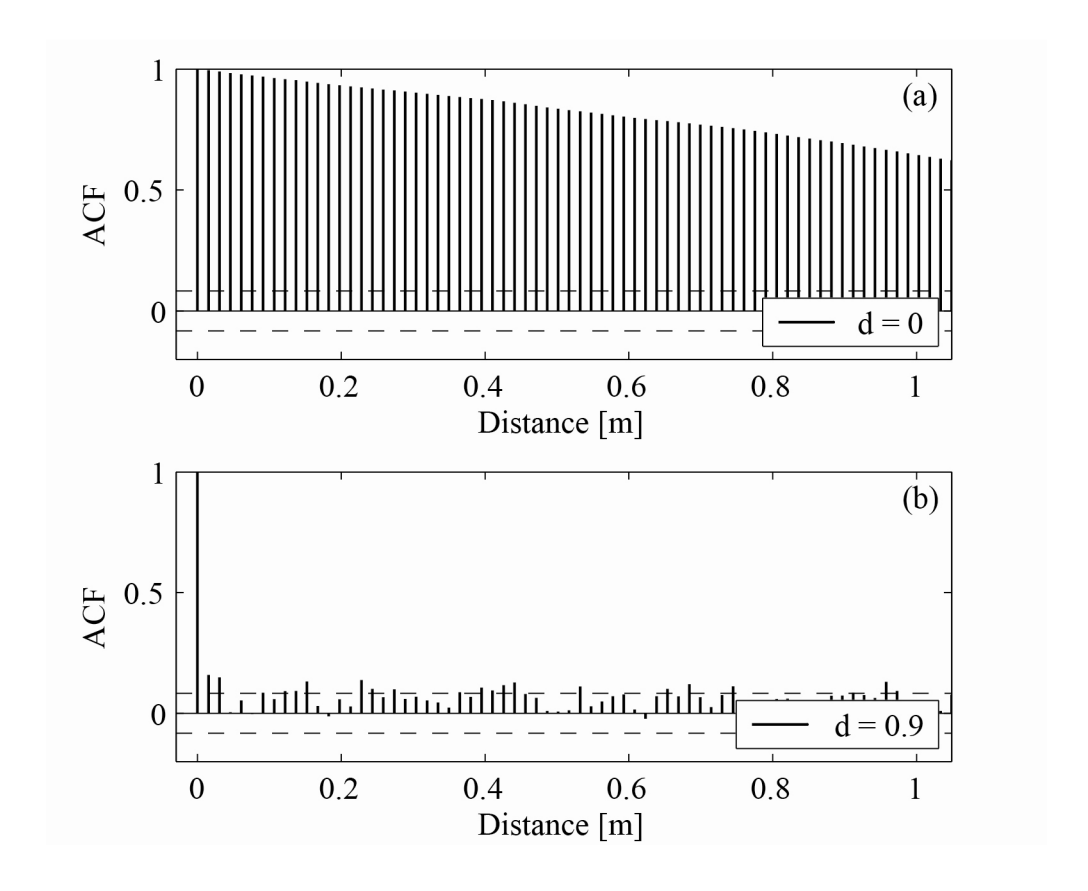


Figure 3.3 Autocorrelation function for $\ln K$ from HRK profile 121108A (see Figure 3.1) before (a) and after (b) applying the fractional difference filter (3.1) with d=0.9. Autocorrelations inside dashed lines are statistically zero.

Next, we discuss our simulation scheme. Since the $\ln K$ data exhibit long range dependence, with a shorter correlation length in the vertical direction, we applied the anisotropic random field generator of *Benson et al.* [2006]: Fourier transformed Gaussian white noise on a 1.5 cm grid was multiplied by a Fourier filter $\psi(k) = \left[\sum_i C_i |k \cdot \theta_i|^2\right]^{\frac{H+1}{2}}$ with Hurst index H=0.4, θ_1 horizontal, θ_2 vertical, and correlation length parameters $C_1=10$ and $C_2=1$ to produce anisotropic $\ln K$ fields with a longer correlation length in the horizontal direction. In this

simulation, any horizontal row or vertical column of simulated data represents a fractional Brownian motion with Hurst index H=0.4. The horizontal autocorrelation parameter C_1 was chosen to match measured autocorrelations between the four vertical HRK profiles 111108A, 111108B, 111108C, and 121108A used in this study, but due to the 4 m horizontal spacing, this represents only a very rough fit. The simulated $\ln K$ field was then adjusted to impose the same mean and standard deviation as the log-transformed HRK data. The conditioning algorithm of Benson et al. [2013] was then applied, to make the simulated $\ln K$ field agree with available HRK data. Figure 3.4a shows the results of this simulation procedure for the combined HRK data, without subdividing into GPR facies.

Next the HRK data were segregated by facies, using the GPR method discussed in Section 3.1. Both the mean and the standard deviation of $\ln K$ were found to vary significantly between facies. Separate $\ln K$ fields with the same mean and standard deviation as the log-transformed HRK data were generated over the entire model domain for each facies, using the same method of *Benson et al.* [2006, 2013] with the same filter, and the same white noise sequence as in Figure 3.4a, with dip angle θ_1 matched to the orientation of GPR reflections for each facies. Then, GPR facies boundaries were used to cut out the relevant portions of the simulated $\ln K$ field for each facies, resulting in the $\ln K$ field shown in Figure 3.4b. The multiscaling fractal filter used in this simulation methodology produces enhanced connectivity, as compared to a traditional multi-Gaussian model. Connectivity is further enhanced by our facies approach, since $\ln K$ statistics vary by facies.

52

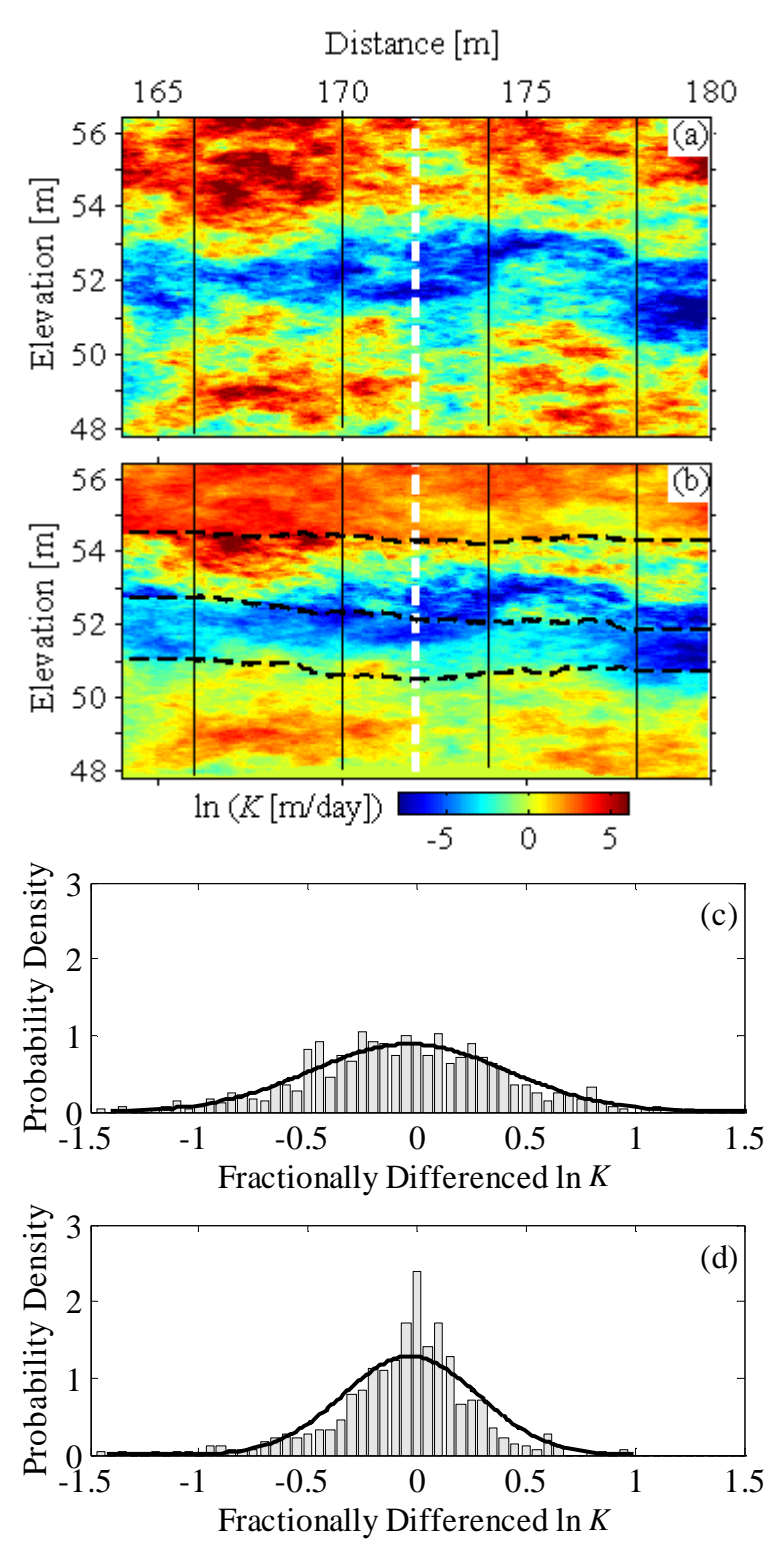


Figure 3.4 Simulated $\ln K$ field without (a) and with (b) GPR facies (dashed lines), conditioned on four HRK profiles (vertical black lines). Histogram (c, d) of one column (white line at x = 172 m) from simulated $\ln K$ field (a, b, respectively) after applying the fractional difference filter (1) with d=0.9. The histogram (c) fits a Gaussian model, but the histogram (d) from facies simulation (b) deviates from Gaussian shape, similar to measured HRK data (Figure 3.2b).

Figure 3.5 shows the Gaussian fit to fractionally differenced ln K data in a single facies, using the facies boundaries shown in Figure 3.4b. The data from facies A (shallowest) at horizontal location 174 m had the smallest standard deviation (σ =0.0110). The probability plot in Figure 3.5a shows that these data fit a Gaussian distribution reasonably well, except for a single outlier (0.7244, removed). The histogram (not shown) is similar to Figure 3.4c. Figure 3.5b shows the corresponding plot for facies D (deepest) at horizontal location 170 m, which had the largest standard deviation (σ =0.3637). Since the points on the probability plot in Figure 3.5b show a significant and systematic deviation from the reference line, a lack of fit to the Gaussian model is indicated. The histogram (not shown) is similar to Figure 3.4d. We attribute this deviation from the Gaussian model in our data to the existence of sub-facies and smaller sedimentary variations with significantly different material properties [Dogan et al., 2011]. In this study, we employ only a few of the most definitive and connected GPR reflection boundaries, to subdivide the model domain into four distinct facies. However, the full geostatistical analysis reported in *Dogan et al.* [2011] did uncover additional substructures. Zhang et al. [2013], and others referenced in Section 3.5 of that paper, find that sub-facies heterogeneity has only a secondary influence on transport, hence the importance of accurately modeling sub-facies is unclear.

As noted by *Silliman and Wright* [1988] and further discussed in *Gómez-Hernádez and Wen* [1998], a multi-Gaussian simulation with a single covariance function will not produce continuous regions where the highest or lowest ln *K* values occur. However, in our model, the facies with the highest or lowest mean ln *K* value produce just such features. This is no contradiction, because our model employs a different multi-Gaussian mean and covariance structure in each facies. In our opinion, the "hole effect" in the variograms of *Rehfeldt et al*.

[1992] and *Salamon et al.* [2007] can be the result of combining data from distinct facies, which will naturally cause a deviation from a single multi-Gaussian model with a fixed mean and covariance structure. Furthermore, combining the simulated multi-Gaussian ln *K* values from different facies does produce the kind of non-Gaussian histogram, with a sharper peak and a heavier tail, frequently seen in column data.

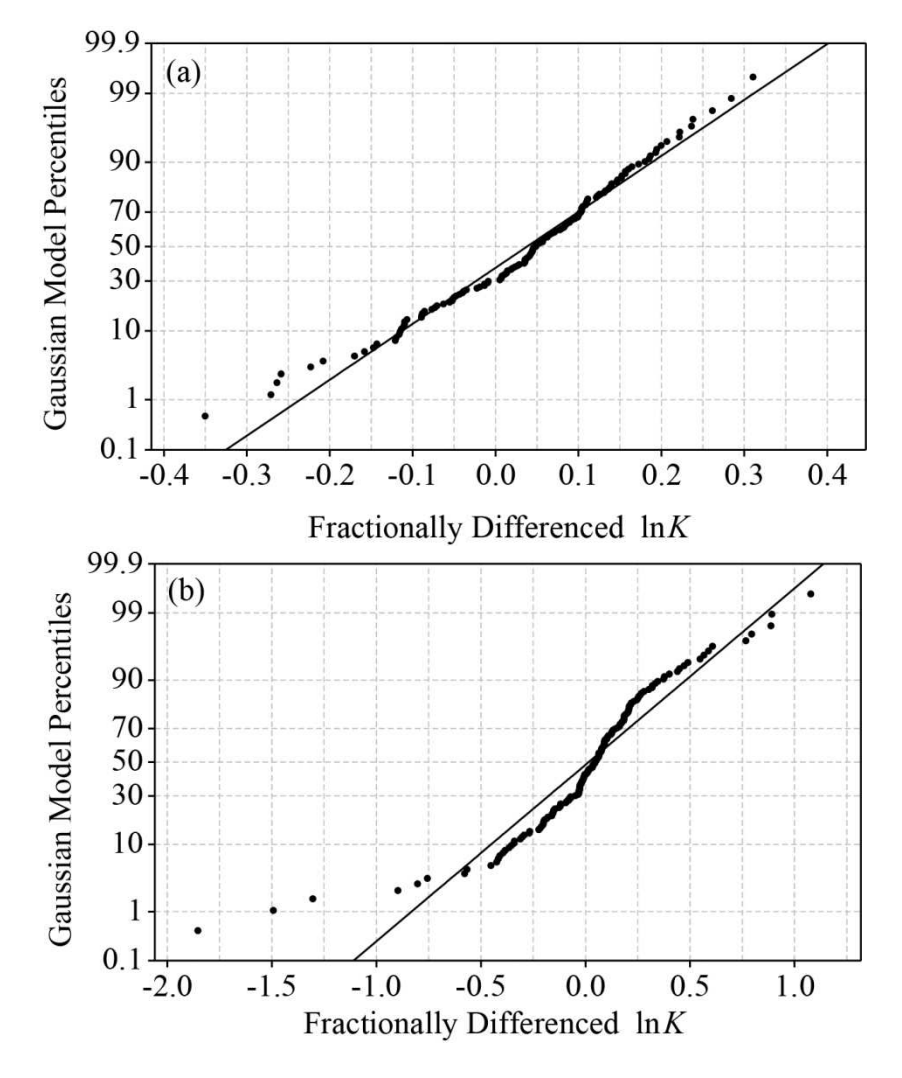


Figure 3.5 Fractionally differenced $\ln K$ data (a) from the shallowest facies at horizontal location 174 m fits a Gaussian distribution. Deepest facies (b) at horizontal location 170 m deviates from the Gaussian model. These probability plots show the sorted data on the horizontal axis, and the corresponding model percentiles for the best fitting Gaussian model on the vertical axis. If the data fits this model, the points will follow the reference line, with some random scatter.

This simulation methodology used to produce the ln *K* field in Figure 3.4b produces results similar to the indicator geostatistics method of *Fogg et al.* [1998], which has been successfully applied in both groundwater hydrology [*Weissmann et al.*, 1999] and surface water hydrology [*Rubin et al.*, 2006]. The idea of combining fractal simulation methods with a facies model is already present in *Lu et al.* [2002]. The difference in our approach is that we use GPR to determine the facies boundaries. Since the actual facies boundaries are known, there is no need to resort to an indicator simulation method to synthesize the facies boundaries. *Ritzi* [2000] notes that lithofacies data can also be used to determine facies boundaries, but if aquifer lithology is not available at sufficient resolution to parameterize a flow and transport model, then a combination of GPR facies and HRK profiles can provide a useful modeling approach for highly detailed *K* field synthesis.

3.3 Model validation

If a simulated $\ln K$ profile exhibits the statistical features of a measured $\ln K$ data profile, then this validates the simulation methodology. The histogram shown in Figure 3.4c represents a single column (81st column, at 172 m) of values from the simulated $\ln K$ field without GPR facies in Figure 3.4a, fractionally differenced with d=0.9 as in Figure 3.2b. Without facies, the fractionally differenced simulated HRK profile fits a Gaussian distribution, and hence does not resemble the measured HRK data. Figure 3.4d shows the corresponding histogram from a single column of the simulated $\ln K$ values with GPR facies in Figure 3.4b, fractionally differenced with d=0.9. Before fractional differencing, the simulated profile histogram (not shown) appeared similar to Figure 3.2a. After fractional differencing, the histogram of simulated values in Figure 3.4d appears quite similar to the corresponding histogram in Figure 3.2b, with a sharper peak and a heavier tail than the best-fitting Gaussian. There are also some significant differences between

Figure 3.4d and Figure 3.2b, including a higher peak and some asymmetry in Figure 3.2b, but the overall shape seems to support our conclusion that combining simulated Gaussian $In\ K$ values from different facies can reproduce a significantly non-Gaussian shape, similar to what is seen in real HRK data profiles. Even though the simulated noise is normal in each facies, the histogram in Figure 3.4d does not fit a normal probability density (Anderson- Darling test p < 0.0005). This is due to the well-known fact that a mixture of Gaussian random variates with different mean and/or standard deviation cannot be normally distributed. Indeed, many non-Gaussian distributions that have been used to model $In\ K$ data, including the Laplace and symmetric stable, are Gaussian mixtures [$Kotz\ et\ al.$, 2001; $Guadagnini\ et\ al.$, 2012; $Riva\ et\ al.$, 2013a]. We conclude that GPR facies are useful in this simulation, as they provide a data-based procedure for delineating statistically distinct regions of K values, leading to the more sharply peaked and non-Gaussian profile evident in Figure 3.4d. The facies approach also allows us to preserve observed correlation structures and angles.

In order to gain a practical appreciation for the accuracy of d estimates, we then simulated a number of statistically identical $\ln K$ fields, and applied automatic d estimation to the resulting $\ln K$ profiles. Using a standard maximum likelihood estimation routine for fractional ARIMA models, we found typical estimates of the d parameter to vary from the true (input) value of d=0.9 by \pm 0.2 in those simulations. Hence we cannot rule out other values of d (including d=1.0, a simple difference), and the estimated d value from any single profile should only be taken as a rough indicator of the true value. However, since the value d=0.9 resulted in no significant serial correlation in any of the four HRK profiles in this study, this value was deemed adequate for our purposes. It is certainly possible that more significant variations in d could emerge on a larger scale, or at a different site.

We believe that the departure from a Gaussian distribution, commonly observed in many ln *K* data profiles from alluvial aquifers, can be attributed to mixing. Although our simulated ln *K* field is based on Gaussian noise, the distribution of any single column exhibits a significant non-Gaussian shape, because different facies are mixed. This leads to the second major finding of our statistical analysis: A simulation that uses GPR facies, with a fractional Brownian motion within each facies, generates ln *K* fields whose fractionally differenced vertical profiles have a strongly non-Gaussian distribution, with a sharper peak and a broader tail, consistent with non-Gaussian ln *K* models applied in previous studies [*Meerschaert et al.*, 2004; *Painter*, 1996]. The GPR data are valuable in this simulation method, since they delineate facies boundaries that allow the Gaussian simulation to reproduce non-Gaussian ln *K* profiles.

3.4 Discussion

Modeling and simulation of *K* fields is challenging, especially in highly heterogeneous aquifers including the MADE site, where the ln *K* fields exhibit anisotropy [*Boggs et al.*, 1990; *Riva et al.*, 2008], long-range correlations [*Neuman*, 2003; *Ritzi et al.*, 2000], non-monotone variograms [*Ritzi et al.*, 2004; *Salamon et al.*, 2007], and a significantly non-Gaussian shape [*Ritzi et al.*, 2004]. The standard model of ln *K* is based on a normal distribution, but many studies have found significant deviations from the Gaussian shape in increments of low resolution ln *K* field data, with a sharper peak and/or heavier tails [*Meerschaert et al.*, 2004; *Painter*, 1996, 2001]. Some researchers have suggested that accurate representation of the *K* data at the smallest scale may be a critical component of solute transport simulation, particularly regarding the distribution and long-range dependence [*Zheng et al.*, 2003; *Ritzi et al.*, 2004; *Dai et al.*, 2004; *Ramanathan et al.*, 2008]. Based on the statistical analysis reported in this paper, we find that the observed non-Gaussian distribution of fractionally differenced ln *K* data from

alluvial aquifers can be reproduced using a Gaussian ln K field in each facies. The combination of ln K data from different facies at different depths combines into a data profile with a non-Gaussian shape (e.g., *Painter*, 2001). The non-Gaussian ln K distributions used in previous studies are also Gaussian mixtures of this type. It is well known that mixing of data from different populations changes the histogram shape, but it is usually impossible to reconstruct the Gaussian components. This has led to popular indicator geostatistics methods that synthesize facies boundaries (e.g., Weissmann et al., 1999). Using GPR facies, it does seem possible to delineate the actual facies boundaries without resorting to simulations, and thereby reduce measured ln K data to a reasonably Gaussian form. This allows a simple method for interpolating highly variable and non-stationary ln K fields. Another advantage of facies modeling is laid out in [Winter et al., 2002, 2003]: It facilitates efficient perturbation-based stochastic methods based on locally homogeneous ln K fields. Riva et al. [2013b] has reported a significantly non-Gaussian distribution of log permeability for the two faces parallel to bedding in a relatively homogeneous sandstone slab, while the distribution on the other four faces was close to Gaussian. Hence the Gaussian facies model promoted here may not be universally applicable.

3.5 Conclusions

In this paper, ground-penetrating radar (GPR) reflections were used to delineate facies boundaries, and a high resolution fractal $\ln K$ field was simulated within each facies to interpolate between available K data. There were two main findings of this study. First, a fractional difference filter can be useful to capture the correlation structure of $\ln K$ profiles. The unfiltered data histogram from one profile is severely distorted, but the filter uncovers a coherent noise distribution, required for simulation design. Second, GPR data can be used to delineate facies boundaries for the K field model. While the overall distribution of $\ln K$ profiles in a typical

alluvial aquifer deviates significantly from Gaussian, it is reasonable to model the ln K field within each GPR facies as Gaussian. The deviation from Gaussian in the combined profile is the result of mixing, since the combination of data from different Gaussian distributions will no longer fit a Gaussian model. In past research, many investigators have assumed a Gaussian model for ln K, while many others have presented strong evidence for non-Gaussian alternatives. Our analysis indicates that both groups are correct, albeit at different scales, consistent with the findings of Lu et al. [2002]. A Gaussian model with an appropriate correlation structure can be adequate for a single facies. For a highly heterogeneous aquifer, comprised of significantly different facies, the combination of ln K values with a different mean and variance in each facies will produce significantly non-Gaussian profiles.

3.6 Acknowledgments

Support for this research was provided by NSF grants DMS-1025486, DMS-0803360, EAR-0738938, EAR-0738955, NIH grant R01-EB012079, and PRF grant 48515-G8. Any opinions, findings, and conclusions or recommendations expressed are those of the authors and do not necessarily reflect the views of the funding agencies. We thank Geoff Bohling and Jim Butler Jr. at the Kansas Geological Survey for insightful discussions. Thanks also to Hans-Peter Scheffler at the University of Siegen for providing the computer simulation code for operator scaling random fields.

APPENDICES

APPENDIX 3.1: Fractional difference filter

The fractional difference filter was pioneered by Hurst [1951] to remove correlation in river flood level data. It has now become a standard tool in one dimensional time series analysis [Brockwell and Davis, 1991] and multidimensional spatial statistics [Beran, 1994]. Given a correlated time series X_n (or a spatial series collected at equally spaced intervals along a one dimensional line), the backward shift operator $BX_n = X_{n-1}$ facilitates a simple notation for the fractional difference

$$\Delta^d X_n = (I-B)^d X_n = \sum_{j=0}^{\infty} w_j X_{n-j},$$
 (A3.1)

where the fractional binomial coefficients

$$w_{j} = (-1)^{j} {d \choose j} = \frac{(-1)^{j} \Gamma(d+1)}{j! \Gamma(d-j+1)}$$
(A3.2)

using the natural extension of the integer order binomial coefficients. Using the well-known property $\Gamma(x+1)=x\Gamma(x)$ of the gamma function, one can also write

$$w_{j} = \frac{-d(1-d)\cdots(j-1-d)}{j!}$$
 (A3.3)

from which the recursive formula $w_j = w_{j-1}(j-1-d)/j$ follows. Hence in the special case where d is a positive integer, the sum (A3.1) is finite, since $w_j = 0$ when j > d. Integer order derivatives are defined as the limit of difference quotients using these operators. In the same way, fractional derivatives can be defined as the limit of fractional difference quotients [Meerschaert and Sikorskii, 2012].

In time series and spatial statistics, an integer order difference is also useful to remove trends, since for example the first order difference of a linear trend is a constant, and the second order difference of a quadratic trend is also a constant. Since the goal is to filter out the correlation (and possibly a trend), an effective fractional difference filter will output an uncorrelated white noise $Z_n = \Delta^d X_n$. This is tested in practice by computing the sample autocorrelation defined by $\hat{\rho}(h) = \hat{\gamma}(h)/\hat{\gamma}(0)$ where the sample autocovariance is defined by

$$\hat{\gamma}(h) = \sum_{n=1}^{N-h} (Z_{n+h} - \overline{Z})(Z_n - \overline{Z}) \quad \text{with} \quad \overline{Z} = \frac{1}{N} \sum_{n=1}^{N} Z_n$$
(A3.3)

for a data set of length N. Standard statistical theory [*Brockwell and Davis*, 1991] shows that, for large N, the sample autocorrelation of an uncorrelated white noise at any lag h is approximately normally distributed with mean zero and variance 1/N. Since this random quantity lies between $\pm 1.96/\sqrt{N}$ approximately 95% of the time, the autocorrelation plots in Figure 3.3 show dashed lines at $\pm 1.96/\sqrt{N}$. Then the correlation in the data is judged to be statistically insignificant (statistically zero) if 95% of the sample autocorrelations $\hat{\rho}(h)$ lie within these bounds, and the remaining sample correlations do not lie very far outside these bounds. In this case, there is no compelling evidence to contradict the (null) hypothesis that the correlation is zero at any lag $h \neq 0$. The data Z_n in Figure 3.2b was obtained from equation (3.1) using the data X_n from Figure 3.2a, and the optimal value of d=0.9 was determined by increasing d gradually until the autocorrelation (Figure 3.3) was reduced to be statistically zero. It is also possible to obtain an estimate of d for a single time series using standard maximum likelihood estimation routines for fractional ARIMA models [*Brockwell and Davis*, 1991].

63

For spatial data in 2 or 3 dimensions collected at equally spaced grid points, a fractional difference filter can be applied in each coordinate. The order *d* of the fractional difference filter can vary with the coordinate to remove spatial correlations. The entire data set can be used to estimate the order(s) of the fractional difference [*Beran*, 1994; *Guo et al.*, 2009], which facilitates a more accurate estimate of the *d* parameter(s).

APPENDIX 3.2: Flow-Transport Simulations

The work presented in this chapter demonstrates the advantages and the details of fractional differencing and fractal stochastic simulation methods for creating K fields. It also emphasizes the contribution of GPR derived facies boundaries to define hydrologically different parts of the aquifer. Although the K fields generated using a combination of GPR and HRK data sets using fractal statistical methods exhibit a better statistical representation of K data, it is important to also see the effects of these different K realizations on flow and transport simulations. Therefore, this section involves flow transport simulations through the simulated K fields to investigate the distinct effects of each data set.

Macro-scale tracer experiments at the MADE site resulted in the well-known non-Gaussian behavior of tracer concentrations with multiple peaks and a heavy tail, as explained in detail in Chapter 1.3. However, most of the earlier modeling efforts were not successful to reproduce both components of the behavior simultaneously. This additional study also aims to test whether it is possible to reproduce these components using new data sets (HRK and GPR) and K fields.

Based on K fields discussed in this chapter, MODFLOW and MT3D software were used to model hydraulic heads and conservative tracer transport. The model domain had 160x570 (width x height) cells representing a 16 by 9.8 m (width x height) vertical cross section of the aquifer. The entire model was saturated during the simulation, with specified head boundaries on the two sides of the domain, and no-flow boundaries above and below. The tracer was injected at x=166 m with 100 mg/l concentration over the entire depth for two days to minimize potential boundary related artifacts. Figure A3.6 (top) shows the simulated plume through the simple K

This appendix is not included in the manuscript.

65

model, assuming a constant *K* values in each facies, set to the median of the measured *K* values in that facies, 500 days after the injection. Figure A3.6 (middle) shows the same plume simulated through the *K* field (shown in Figure 3.4a) populated without using facies boundaries. Figure A3.6 (bottom) shows the plume simulated through the *K* field populated using both HRK data and facies boundaries. Flow and transport through the top and bottom facies is significantly faster, with more dispersion than the middle two facies.

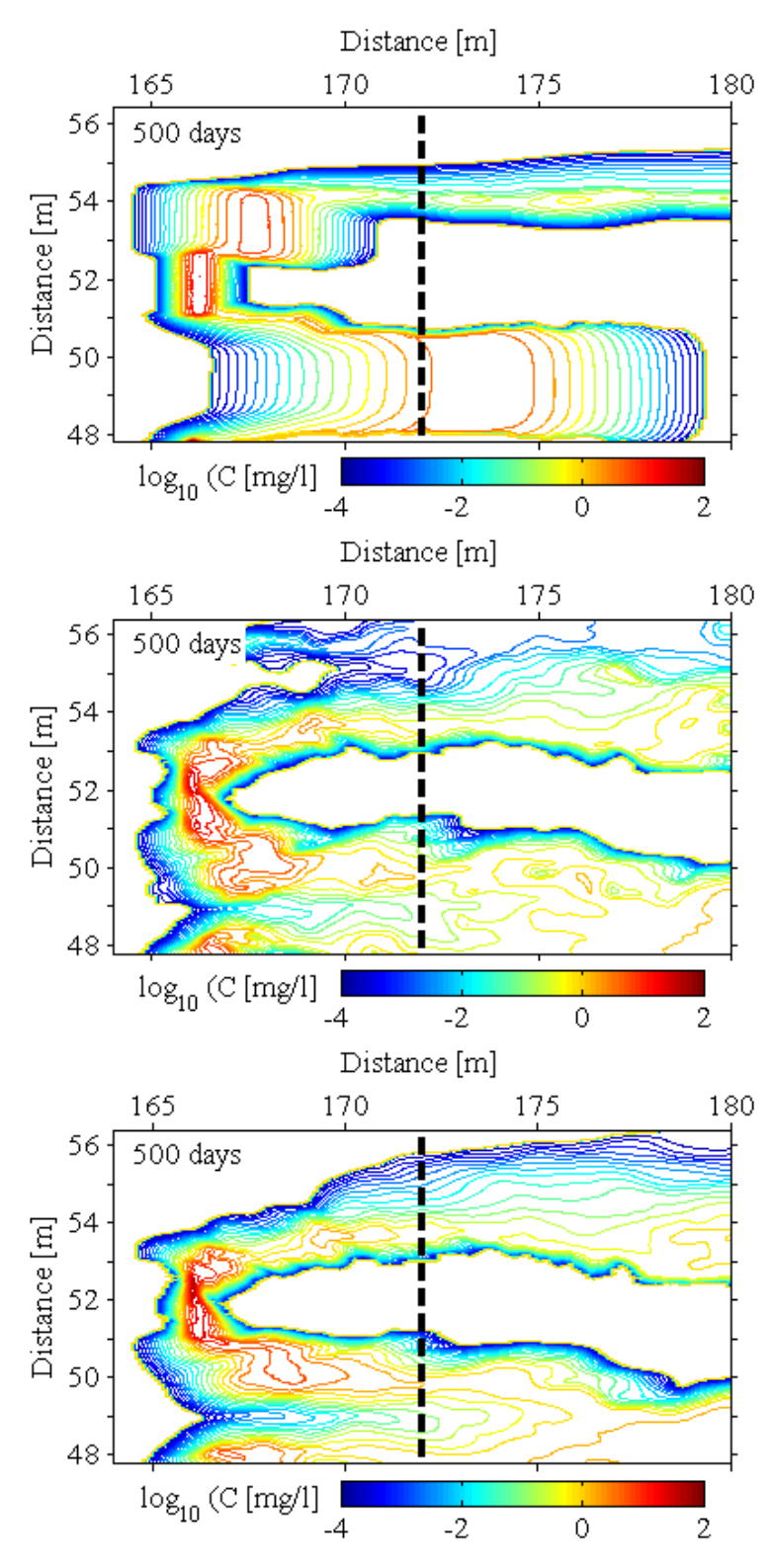


Figure A3.6 Simulated plume 500 days after the end of injection, using a constant *K* value in each GPR facies (top), the *K* field from Figure 3.4a without GPR facies (middle), and the *K* field from Figure 3.4b with GPR facies (bottom).

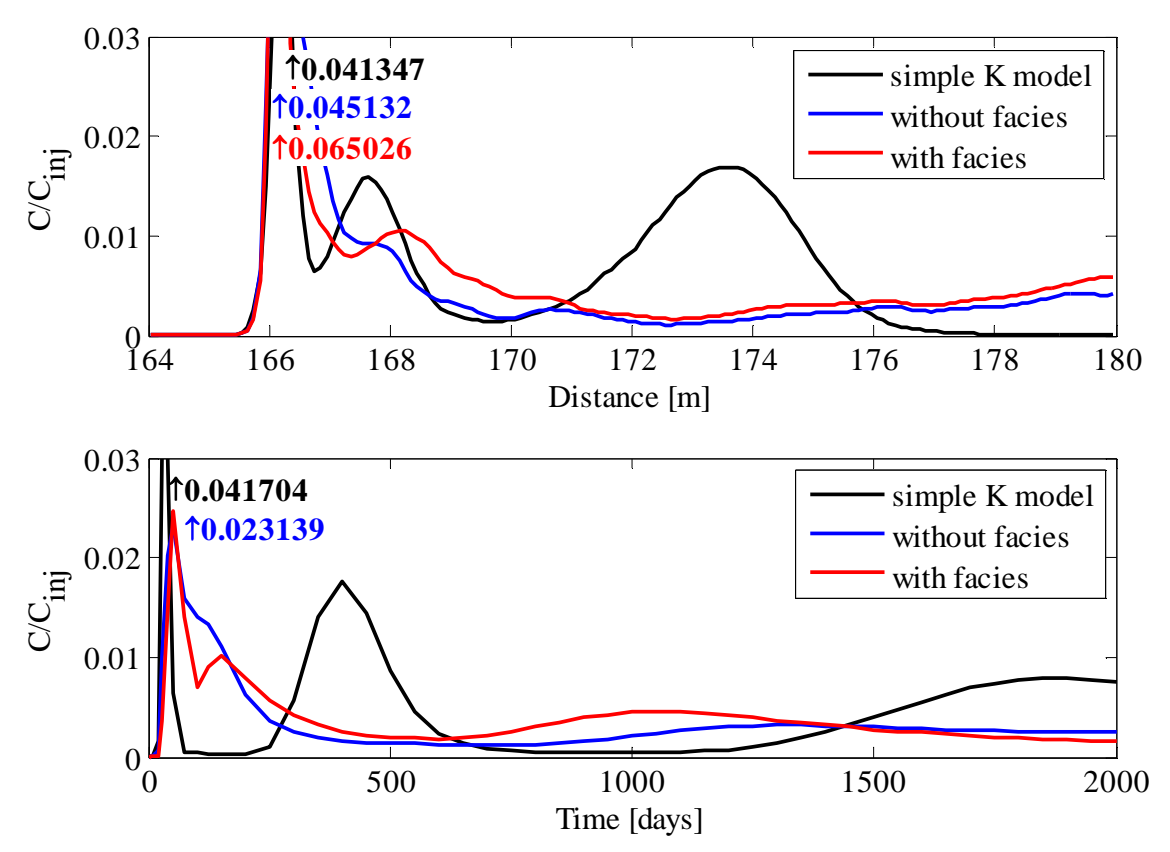


Figure A3.7 Normalized concentration profiles (top) 500 days after the end of injection, and normalized concentration breakthrough curves (bottom), measured at location x=172 m, from the three simulations illustrated in Figure A3.6.

In order to achieve a detailed comparison of the three simulations illustrated in Figure A3.6, concentration histories and profiles were created. Figure A3.7 (top) shows the normalized concentration profiles for the simulated plumes. Figure A3.7 (bottom) shows the normalized concentration histories at location x=172 m, black dashed lines in Figure A3.6. These curves demonstrate the impact of each data set (GPR and HRK) on plume behavior. The simple *K* model represents what can be accomplished using only GPR facies. The resulting curves show smooth, symmetrical variations in concentration that do not compare favorably to the field measurements at the MADE site. This demonstrates the value of detailed HRK conditioning data for capturing natural plume roughness. The simulated curves without facies seem more realistic, but significantly smoother than the model with facies. The breakthrough curve has multiple

peaks and a heavy tail, consistent with tracer tests at the MADE site. I conclude that HRK data is important for characterizing micro-scale variations, and GPR facies are useful for delineating meso-scale variation. Together, they allow a simple Gaussian ln K model in each facies to reproduce a realistic K field, consistent with the measured HRK data, and resulting in plausible simulated plume behavior.

REFERENCES

REFERENCES

- Benson, D. A., M. M. Meerschaert, B. Baeumer, and H. P. Scheffler (2006), Aquifer operator-scaling and the effect on solute mixing and dispersion, Water Resources Research, 42(1), doi:10.1029/2004WR003755.
- Benson, D. A., M. M. Meerschaert, and J. Revielle (2013), Fractional calculus in hydrologic modeling: A numerical perspective, Advances in Water Resources, 51, 479–497, doi:10.1016/j.advwatres.2012.04.005.
- Beran, J. (1994), Statistics for long-memory processes. Chapman & Hall/CRC Press, Boca Raton, Florida.
- Berkowitz, B., A. Cortis, M. Dentz, and H. Scher (2006), Modeling non-Fickian transport in geological formations as a continuous time random walk, Rev. Geophys., 44, RG2003.
- Bianchi, M., C. Zheng, G. R. Tick, and S. M. Gorelick (2011), Investigation of small-scale preferential flow with a forced-gradient tracer test, Ground Water, 49(4), 503–514.
- Boggs, J. M., S. C. Young, D. J. Benton, and Y. C. Chung (1990), Hydrogeologic characterization of the MADE site, epri en-6915, research project 2485-5, interim report, Electric Power Research Institute, Palo Alto, CA.
- Bohling, G. C., G. Liu, S. J. Knobbe, E. C. Reboulet, D. W. Hyndman, P. Dietrich, and J. J. Butler Jr (2012), Geostatistical analysis of centimeter-scale hydraulic conductivity variations at the MADE site, Water Resources Research, 48(2), doi:10.1029/2011WR010791.
- Brockwell, P. J. and R. A. Davis (1991), Time Series: Theory and Methods, 2nd ed. New York: Springer-Verlag.
- Butler Jr, J. J., P. Dietrich, V. Wittig, and T. Christy (2007), Characterizing hydraulic conductivity with the direct-push permeameter, Ground Water, 45(4), 409–419.
- Cushman, J. H., and T. R. Ginn (2000), Fractional advection-dispersion equation: A classical mass balance with convolution-Fickian flux, Water Resources Research, 36(12), 3763–3766.
- Dai, Z., R. W. Ritzi Jr., C. Huang, Y. N. Rubin and D. F. Dominic (2004), Transport in heterogeneous sediments with multimodal conductivity and hierarchical organization across scales, J. Hydrology, 294(1–3), 68–86.
- Dogan, M., R. L. Van Dam, G. C. Bohling, J. J. Butler Jr, and D. W. Hyndman (2011), Hydrostratigraphic analysis of the MADE site with full-resolution GPR and direct-push hydraulic profiling, Geophys. Res. Lett., 38(6), doi:10.1029/2010GL046439.
- Fogg, G. E., C. D. Noyes, and S. F. Carle (1998), Geologically based model of heterogeneous hydraulic conductivity in an alluvial setting, Hydrogeology J., 6(1), 131–143.

- Gómez-Hernádez, J. J., and X.-H. Wen (1998), To be or not to be multi-Gaussian? A reflection on stochastic hydrogeology, Adv. Water Resour. 21(1), 47–61.
- Guadagnini, A., M. Riva, and S. P. Neuman (2012), Extended power-law scaling of heavy-tailed random air-permeability fields in fractured and sedimentary rocks. Hydrol. Earth Syst. Sci. 16, 3249–3260, doi:10.5194/hess-16-3249-2012.
- Guo, H., C. Y. Lim, and M. M. Meerschaert (2009), Local Whittle estimator for anisotropic random fields. J. Multivariate Anal. 100(5), 993–1028.
- Heinz, J., and T. Aigner (2003), Hierarchical dynamic stratigraphy in various Quaternary gravel deposits, Rhine glacier area (SW Germany): implications for hydrostratigraphy, International Journal of Earth Sciences, 92(6), 923–938.
- Herrick, M. G., D. A. Benson, M. M. Meerschaert, and K. R. McCall (2002), Hydraulic conductivity, velocity, and the order of the fractional dispersion derivative in a highly heterogeneous system, Water Resources Research, 38(11), 1227.
- Hurst, H. E. (1951), Long-term storage capacity of reservoirs, Trans. Amer. Soc. Civil Eng., 116, 770–808.
- Kohlbecker, M. V., S. W. Wheatcraft, and M. M. Meerschaert (2006), Heavy-tailed log hydraulic conductivity distributions imply heavy-tailed log velocity distributions, Water Resources Research, 42(4), doi:10.1029/2004WR003815.
- Kotz, S., T. J. Kozubowski, and K. Podgorski (2001), The Laplace Distribution and Generalizations: A Revisit with Applications to Communications, Economics, Engineering, and Finance, Birkhäuser, Boston.
- Liu, G., J. J. Butler Jr, G. C. Bohling, E. Reboulet, S. Knobbe, and D. W. Hyndman (2009), A new method for high-resolution characterization of hydraulic conductivity, Water Resources Research, 45(8), doi:10.1029/2009WR008319.
- Liu, G., C. Zheng, G. R. Tick, J. J. Butler Jr, and S. Gorelick (2010), Relative importance of dispersion and rate-limited mass transfer in highly heterogeneous porous media: Analysis of a new tracer test at the Macrodispersion Experiment (MADE) site, Water Resources Research, 46(3), W03524.
- Liu, G., J. J. Butler Jr, E. Reboulet, and S. Knobbe (2012), Hydraulic conductivity profiling with direct-push methods, Grundwasser, 17(1), 19–29.
- Llopis-Albert, C., and J. E. Capilla (2009), Gradual conditioning of non-Gaussian transmissivity fields to flow and mass transport data. 3 Application to the Macrodispersion Experiment (MADE-2) site, on Columbus Air Force Base in Mississippi (USA) J. Hydro. 371, 75–84.
- Lu, S., F. J. Molz, G. E. Fogg, and J. W.Castle (2002), Combining stochastic facies and fractal models for representing natural heterogeneity, Hydrogeology J., 10(4), 475–482.

- Major, E., D. A. Benson, J. Revielle, H. Ibrahim, A. Dean, R. M. Maxwell, E. Poeter, and M. Dogan (2011), Comparison of Fickian and temporally nonlocal transport theories over many scales in an exhaustively sampled sandstone slab, Water Resources Research, 47(10), W10519.
- Meerschaert, M. M., T. J. Kozubowski, F. J. Molz, and S. Lu (2004), Fractional Laplace model for hydraulic conductivity, Geophys. Res. Lett., 31, 1–4.
- Meerschaert, M. M. and A. Sikorskii (2012), Stochastic Models for Fractional Calculus. De Gruyter Studies in Mathematics 43, De Gruyter, Berlin.
- Molz, F. J., and G. K. Boman (1993), A fractal-based stochastic interpolation scheme in subsurface hydrology, Water Resources Research, 29(11), 3769–3774.
- Neuman, S. P. (2003), Relationship between juxtaposed, overlapping, and fractal representations of multimodal spatial variability, Water Resources Research, 39(8), 1205.
- Neuman, S. P., and D. M. Tartakovsky (2009), Perspective on theories of non-Fickian transport in heterogeneous media, Adv. Water Resour., 32, 670-680.
- Painter, S. (1996), Evidence for non-Gaussian scaling behavior in heterogeneous sedimentary formations, Water Resources Research, 32(5), 1183–1195.
- Painter, S. (2001), Flexible scaling model for use in random field simulation of hydraulic conductivity, Water Resources Research, 37(5), 1155–1163.
- Ramanathan, R., R. W. Ritzi, and C. Huang (2008), Linking hierarchical stratal architecture to plume spreading in a Lagrangian-based transport model, Water Resources Research, 44(4), W04503.
- Rehfeldt, K. R., J. M. Boggs, and L. W. Gelhar (1992), Field study of dispersion in a heterogeneous aquifer: 3. Geostatistical analysis of hydraulic conductivity, Water Resources Research, 28(12), 3309–3324.
- Renard, P., and D. Allard (2011), Connectivity metrics for subsurface flow and transport, Adv. Water Resour., 51, 168–196.
- Ritzi, R. W., D. F. Dominic, A. J. Slesers, C. B. Greer, E. C. Reboulet, J. A. Telford, R. W. Masters, C. A. Klohe, J. L. Bogle, and B. P. Means (2000), Comparing statistical models of physical heterogeneity in buried-valley aquifers, Water Resources Research, 36(11), 3179–3192.
- Ritzi, R. W. (2000), Behavior of indicator variograms and transition probabilities in relation to the variance in lengths of hydrofacies, Water Resources Research, 36(11), 3375–3381.
- Ritzi, R. W., Z. Dai, D. F. Dominic, Y. N. Rubin (2004), Spatial correlation of permeability in cross-stratified sediment with hierarchical architecture, Water Resources Research, 40(3), W03513.

- Riva, M., A. Guadagnini, D. Fernàndez-Garcia, X. Sanchez-Vila, and T. Ptak (2008), Relative importance of geostatistical and transport models in describing heavily tailed breakthrough curves at the Lauswiesen site, J. Contam. Hydrol., 101(1-4), 1–13.
- Riva, M., S.P. Neuman, and A. Guadagnini (2013), Sub-Gaussian model of processes with heavy tailed distributions applied to permeabilities of fractured tuff. Stoch. Environ. Res. Risk Assess. 27, 195–207, doi:10.1007/s00477-012-0576-y.
- Riva M., S.P. Neuman, A. Guadagnini (2013), Anisotropic scaling of Berea sandstone log air permeabilities statistics, Vadose Zone Journal, in press, doi: 10.2136/vzj2012.0153.
- Rubin, Y. and A. G. Journel (1991), Simulation of non-Gaussian space random functions for modeling transport in groundwater. Water Resources Research, 27, 1711–1721.
- Rubin, Y., I. A. and Lunt, and J. S. Bridge (2006), Spatial variability in river sediments and its link with river channel geometry, Water Resources Research, 42, W06D16.
- Salamon, P., D. Fernàndez-Garcia, and J. J. Gómez-Hernández (2007), Modeling tracer transport at the MADE site: the importance of heterogeneity. Water Resources Research, 43, W08404.
- Schmelzbach, C., J. Tronicke, P. Dietrich (2011), Three-dimensional hydrostratigraphic models from ground-penetrating radar and direct-push data. Journal of Hydrology, 398, 235-245.
- Silliman, S. E., and A. L. Wright (1998), Stochastic analysis of paths of high hydraulic conductivity in porous media. Water Resources Research, 24, 1901–1910.
- Tennekoon, L., M. C. Boufadel, D. Lavalee, and J. Weaver (2003), Multifractal anisotropic scaling of the hydraulic conductivity, Water Resources Research, 39(7), 1193, doi:10.1029/2002WR001645.
- Van Overmeeren, R. A. (1998), Radar facies of unconsolidated sediments in the Netherlands: A radar stratigraphy interpretation method for hydrogeology, Journal of Applied Geophysics, 40(1), 1–18.
- Weissmann, G. S. and G. E. Fogg (1999), Multi-scale alluvial fan heterogeneity modeled with transition probability geostatistics in a sequence stratigraphic framework, J. Hydrology, 226(1), 48–65.
- Winter, C.L., D.M. Tartakovsky, and A. Guadagnini (2002), Numerical solutions of moment equations for flow in heterogeneous composite aquifers. Water Resources Research, 38(5), 10.1029/2001WR000222.
- Winter, C.L., D.M. Tartakovsky, and A. Guadagnini (2003), Moment differential equations for flow in highly heterogeneous porous media, Surveys in Geophysics, 24(1), 81–106.
- Zhang, Y., C. T. Green, and G. E. Fogg (2013), The impact of medium architecture of alluvial settings on non-Fickian transport, Adv. Water Resour., 54, 78-99.

- Zheng, C., and S. M. Gorelick (2003), Analysis of Solute Transport in Flow Fields Influenced by Preferential Flowpaths at the Decimeter Scale, Ground Water, 41(2), 142–155.
- Zheng, C., M. Bianchi, and S. M. Gorelick (2011), Lessons learned from 25 years of research at the MADE site, Ground Water, 49(5), 649–662.
- Zinn, B., and C. F. Harvey (2003), When good statistical models of aquifer heterogeneity go bad: A comparison of flow, dispersion, and mass transfer in connected and multivariate Gaussian hydraulic conductivity fields, Water Resources Research, 42(3), 1051.

Chapter 4

Novel characterization method provides a major advance for

flow and transport prediction

Abstract

Predicting the fate and transport of solutes in aquifers is a societal grand challenge [Cantor, 1997] that requires characterization of aquifer properties. Although many studies have reasonably explained transport through mildly heterogeneous aquifers, transport through highly heterogeneous aquifers has yet to be accurately predicted. The complex transport behavior in highly heterogeneous aquifers has fueled an ongoing debate in the hydrology community for more than two decades [e.g., Berkowitz et al., 2002; Boggs et al., 1992; Dagan et al., 1992; Dagan and Neuman, 1997; Zimmerman et al., 1998]. A wide range of modeling approaches have been used to simulate tracer and contaminant transport at such sites, ranging from the classical advection-dispersion equation (ADE) to dual-domain mass transfer and methods that impart preferential flow paths to describe the observed complex behavior. A striking outcome of this research to date has been the inability of approaches to reasonably predict transport in highly heterogeneous systems based solely on field data. Here we demonstrate that when supported by direct push high-resolution characterization data, advection dispersion equation can accurately predict flow and transport without the need for calibration or addition of features that have not been observed in the field. The ramifications for practical issues, such as the design of effective remediation schemes and reliable risk assessments, are profound.

4.1 Introduction

Hydraulic conductivity (*K*) is the main property that controls solute transport in subsurface flow systems [e.g., *Dagan*, 1989]. Thus, accurate predictions of flow and transport through porous media require good representations of the *K* distribution [e.g., *Molz et al.*, 1986]. Examples of successful applications of ADE models based on statistical distributions of *K* data from mildly heterogeneous aquifers include those from Borden Ontario [e.g., *Freyberg*, 1986; *Mackay et al.*, 1986], Cape Cod, MA [e.g., *Garabedian et al.*, 1991; *LeBlanc et al.*, 1991], and Schoolcraft, MI [*Hyndman et al.*, 2000, *Phanikumar et al.*, 2005].

However, flow and transport through highly heterogeneous sites has proven to be much more challenging [e.g., $Eggleston\ and\ Rojstaczer$, 1998; $Whittaker\ and\ Teutsch$, 1999]. The MAcro-Dispersion Experiment (MADE) site in Columbus, Mississippi is one of the best-studied highly heterogeneous sites (variance of $\ln\ K = 4.5$) [$Boggs\ et\ al.$, 1992]. Much of the debate about the applicability of the ADE at highly heterogeneous sites started with the experiments at the MADE site. The outcome of the natural gradient tracer tests at this site highlighted the limitations of existing and new modeling approaches.

Two large-scale tracer tests were performed at the site; in this paper we focus on the most studied experiment called MADE-1, conducted from October 1986 to June 1988 [Boggs, 1991]. This test involved injection of bromide solution through an array of five boreholes, approximately perpendicular to natural gradient of groundwater flow. The injection was followed by collection of thousands of samples from 258 monitoring wells that were later analyzed for tracer concentrations. The resulting data showed non-Gaussian tracer migration that was very different than predicted using the ADE model based on K data from borehole flowmeters. Low concentrations were detected far down gradient starting soon after the injection, yet more than

20% of the mass stayed within 6-7 meters of the injection wells for the duration of the experiments [*Adams and Gelhar*, 1992].

Several approaches have been proposed to explain the observed tracer transport at the site including: incorporating preferential flow paths [Zheng and Gorelick, 2003], multi-indicator models [Fiori et al., 2013], mass transfer between mobile and immobile domains [Harvey and Gorelick, 2000], and using a fractional form of the ADE [Benson et al., 2001]. Although some of these approaches reasonably represented the average plume behavior in one dimension, they did not accurately replicate several important characteristics of the plume including the spatial extent. In addition, these methods would be difficult to use in a predictive sense as they are not easily parameterized based solely on field data. We postulate that the difficulty in predicting solute transport at heterogeneous sites like MADE is at least partly due to the absence of sufficient high-resolution hydraulic property data to parameterize the models.

4.2 Methods

Here we present an approach to reproduce spatial extent of the tracer plume measured during the MADE experiments. To this effect, we collected a novel suite of high-resolution K data using a recently developed in-situ measurement method called the High-Resolution Hydraulic Conductivity (HRK) tool [*Liu et al.*, 2009]. This direct push tool can collect a 10 m long profile in two to four hours, providing hydraulic conductivity estimates with an unprecedented 1.5 cm vertical resolution. This allows important characterization of much smaller scale transport features than previously possible [*Dogan et al.*, 2011; *Bohling et al.*, 2012].

In this study, we exploit the power of this novel tool along with fractal stochastic methods to populate 3D hydraulic conductivity fields. Several studies have demonstrated that

fractional differencing can remove long range dependence, which allows the investigation of the underlying distribution of *K* data [e.g., *Benson et al.*, 2001]. Moreover, fractals are well-suited to represent the connectivity of natural phenomena. Parameters for the fractal *K* field generation were calculated based on autocorrelation and variogram analysis of the HRK data [*Meerschaert et al.*, 2013], which were also used as hard conditioning values for the stochastic fields.

The flow and transport model domain for this study includes a region of high density HRK data near the tracer injection area of the MADE experiments (Figure 4.1). The model grid was defined with over 3.2 million $0.25 \times 0.25 \times 0.05$ m (length x width x height) cells oriented with the long axis parallel to the average downgradient direction of the observed plumes. The east and west edges of the model, which are approximately along flow paths, were assumed to be no flow boundaries. The north and south edges of the model were assumed constant head boundaries, and were assigned head values based on the average measured heads during the first 503 days of the MADE-1 tracer experiment. The maximum measured water level increase (0.64 m; *Boggs et al.* [1992]) across the five injection wells was used as a test of the reasonableness of simulated K fields. Of the 20 generated stochastic K fields, the 6 that provided maximum simulated head increases within 25% of the measured value (0.64 \pm 0.16 m) were selected for transport simulations.

Transport simulations, based on the classical ADE, were performed in MT3D [*Zheng and Wang*, 1999] without any calibration or parameter estimation. Parameters for the transport simulations were defined based on literature as follows: longitudinal dispersivity of 0.05 m [*Gelhar*, 1993], transverse horizontal and vertical dispersivity ratios of 0.1 and 0.01; effective molecular diffusion coefficient of 10⁻⁶; vertical and horizontal anisotropy in hydraulic conductivity of 1 since we assume that the anisotropy will be introduced by our highly

heterogeneous and high-resolution K fields; and constant porosity of 0.35 [Adams and Gelhar, 1992]. Transport simulations were based on the 3rd order Total Variation Diminishing scheme, which is mass conservative with minimal numerical dispersion. Total injected mass in the six simulations averaged 25.1 kg with a standard deviation of 0.143 kg, which compares favorably with the injected mass of 25.0 kg during the experiment.

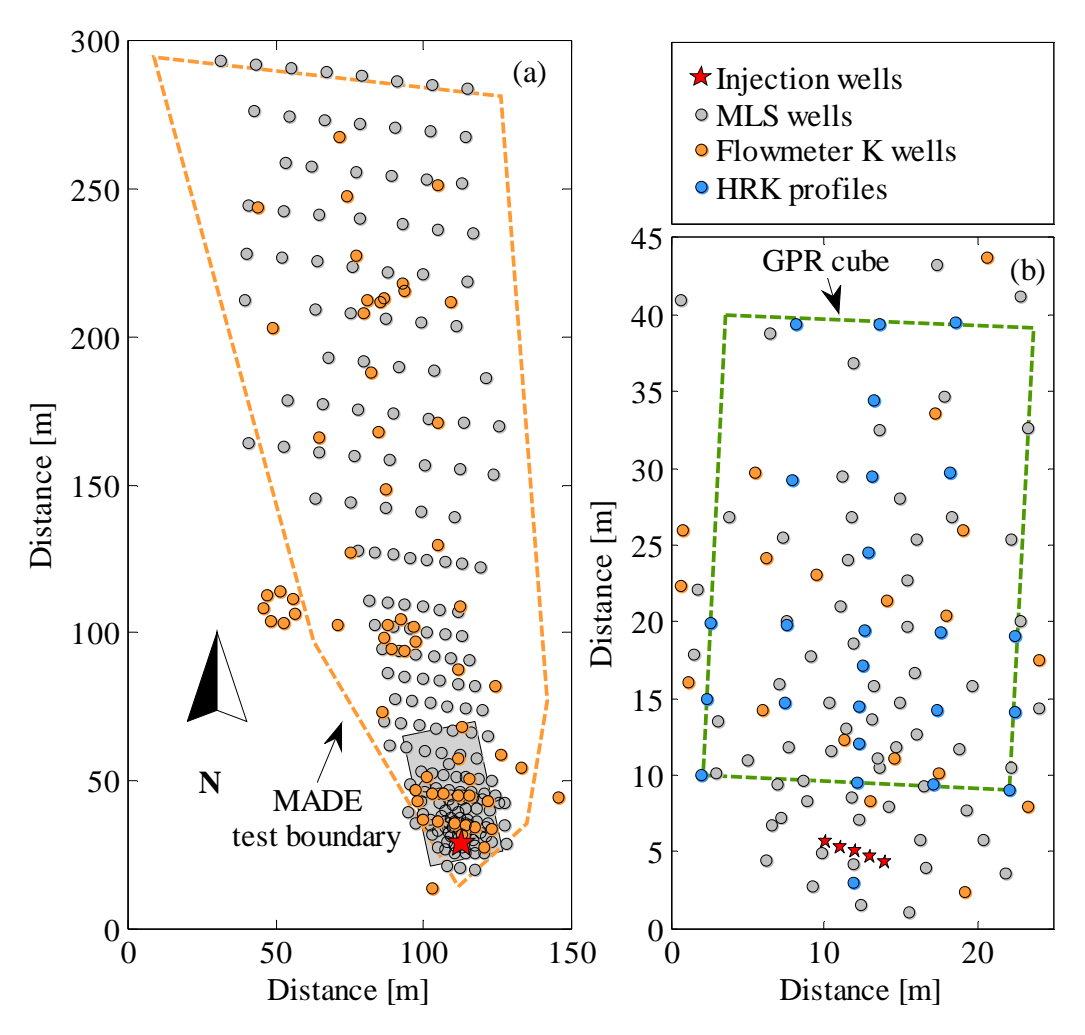


Figure 4.1 (a) Map of the MADE site with the test boundary (dashed line) and sampling locations; gray shaded rectangle shows the model domain used for simulations. (b) Model domain with HRK, injection, and observation borehole locations.

4.3 Results

We first compare the simulated versus observed transport using 1D mass distribution profiles, which has been the community standard for this site [e.g., *Adams and Gelhar*, 1992; *Fiori et al.* 2013]. We then provide the first ever 2D comparison. Only concentration measurements and simulated values that were larger than specified detection limits (0.01 mg/l for the presented snapshot) were used in this analysis. To replicate the experimental procedure we sampled the simulations at the location and depth of every multi-level sampler included in the field experiment. The sampled concentrations were then interpolated in 3D using a 1 x 1 x 0.5 m (dx, dy, dz) grid, and integrated vertically (along z-axis) and horizontally (along y-axis) following the procedure in *Adams and Gelhar* [1992].

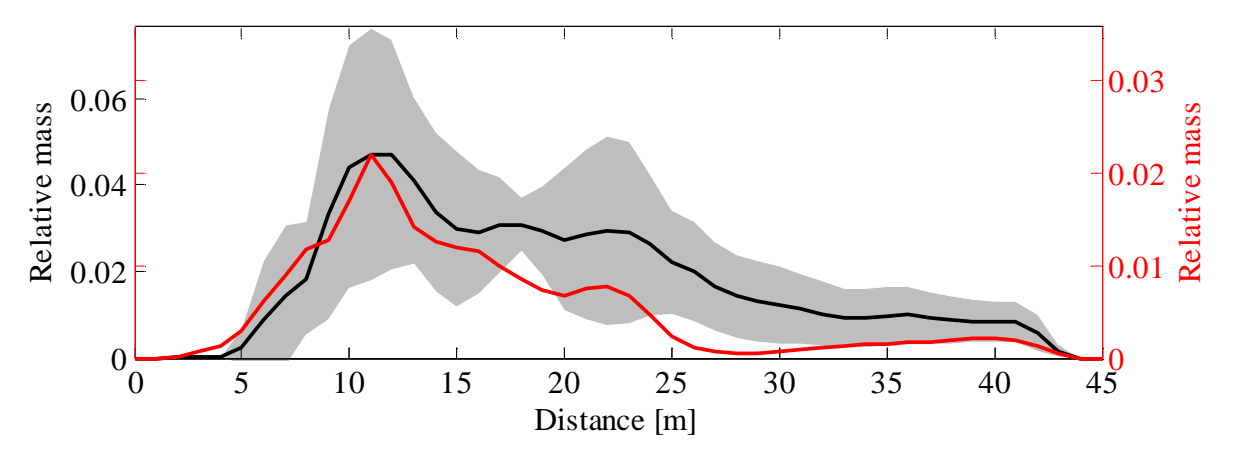


Figure 4.2 Relative mass distribution profiles 501 days after the injection. The black line shows the mean of the simulations along with 2σ error range (in gray shaded area); the red line shows the profile for the MADE-1 observations.

The t=503 day snapshot was chosen for comparison as it is the most commonly presented in publications with MADE-1 simulations (Figure 4.2) in comparison to the measured relative mass distribution profile. The shape of the mean simulated curve is strikingly similar to the experiment. The location, extent of the peaks and the tailing behavior of the mean simulated curve reasonably represent the measured mass distribution, although the average of the

simulations shows somewhat heavier tails than was observed. Both could be improved by optimization or calibration of porosity, but this would reduce the predictive power of the approach.

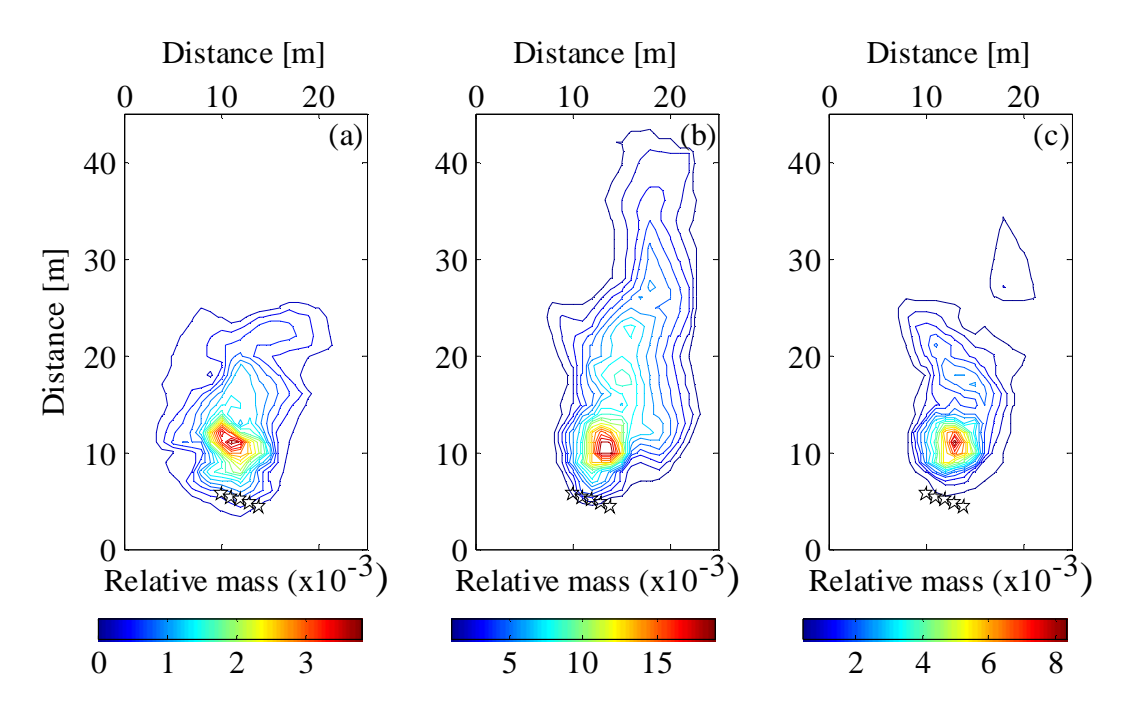


Figure 4.3 Vertically integrated contour maps of relative mass 503 days after the start of injection for MADE-1 experiment (a), the mean of the 6 simulations that met the head criteria (b) a sample simulation which matches the head change criteria best (c). All three contour maps were created following the same interpolation procedure, as discussed in the text.

Despite the large quantity of research that has focused on the MADE site tracer test data, literature contains no examples comparing simulation results with experimental data in two dimensions. Figure 4.3a shows a map of vertically integrated relative mass for the experiment data, which can be compared to the mean of 6 simulations that match the head change criteria (Figure 4.3b) and to the simulation that best matches the observed head increase during the tracer injection (Δh =0.637 m; Figure 4.3c). The measured extent of the plume, defined by the relative mass parallel and transverse to flow as 22 and 17 m, respectively, is similar to the simulated

values of 28 and 15 m (Figure 4.3a, c). Also, the measured plume center of mass is very similar to those of the simulated plumes.

4.4 Discussion and Conclusions

In this paper we demonstrate that, contrary to common belief, the classic ADE can reproduce the measured distribution of MADE tracer concentrations. Our approach is different from previous research to address this problem in that it uses a novel set of high-resolution K data in combination with a fractal method to generate stochastic K fields. No calibration or parameter estimation was used to improve the fit to measured data.

As with any transport modeling approach, there are differences between simulated and observed concentrations. The total mass of the simulations is approximately twice the measured mass. Other studies have shown similar observations, which may be due to a range of factors including entrapment of tracer in the vadose zone [Adams and Gelhar, 1992]. We tested the influence of transient flow behavior using almost two years of temporal water level measurements, and found that this did not explain the difference. Other possible reasons include differences between the simulated and field sampling procedure, which involves pumping sample out from different levels of boreholes where small scale mixing of water with higher and lower tracer concentrations will occur. Another possible explanation for the difference is due to the absence of HRK profiles in close proximity to the injection wells. However, these data could not be collected as the injection area was dug out and homogenized for the MADE 3 tracer test in the 1990s. Inclusion of K data from flowmeter measurements from this area did not significantly improve the recovered mass discrepancy.

Overall, the approach presented here successfully reproduced nearly all aspects of the observed tracer plume without calibration. This includes the heavy tails that have previously only been reproduced using transport theories such as dual domain mass transport or imposed high K pathways. Predictive solute transport based solely on field data, such as done here, has immense value for improving the ability to design more effective remediation schemes.

REFERENCES

REFERENCES

- Adams, E. E., and L. W. Gelhar (1992), Field study of dispersion in a heterogeneous aquifer: 2. Spatial moments analysis, Water Resources Research, 28(12), 3293–3307, doi:10.1029/92WR01757.
- Benson, D. A., R. Schumer, M. M. Meerschaert, and S. W. Wheatcraft (2001), Fractional dispersion, Levy motion, and the MADE tracer tests. Transport in Porous Media 42: 211.
- Berkowitz, B., J. Klafter, R. Metzler, H. Scher (2002), Physical pictures of transport in heterogeneous media: Advection-dispersion, random-walk, and fractional derivative formulations. Water Resources Research, 38: 1191.
- Bohling, G. C., G. Liu, S. J. Knobbe, E. C. Reboulet, D. W. Hyndman, P. Dietrich, and J. J. Butler Jr. (2012), Geostatistical analysis of centimeter-scale hydraulic conductivity variations at the MADE site, Water Resources Research, 48: W02525.
- Boggs, J. M. (1991), Database for the First Macrodispersion Experiment (MADE-1). Electric Power Research Institute.
- Boggs, J. M., S. C. Young, L. M. Beard, L. W. Gelhar, K. R. Rehfeldt, and E. E. Adams (1992), Field study of dispersion in a heterogeneous aquifer: 1. Overview and site description. Water Resources Research, 28, 3281-3291.
- Cantor, K. P. (1997), Drinking water and cancer. Cancer Causes and Control 8: 292-308.
- Dagan, G. (1989), Flow and Transport in Porous Formations. Springer-Verlag GmbH & Co.KG.
- Dagan, G., and S. P. Neuman (1997), Subsurface flow and transport: A stochastic approach. International Hydrology Series.
- Dagan, G., V. Cvetkovic, and A. Shapiro (1992), A solute flux approach to transport in heterogeneous formations. 1. The general framework. Water Resources Research, 28: 1376.
- Dogan, M., R. L. Van Dam, G. C. Bohling, J. J. Butler Jr., D. W. Hyndman (2011), Hydrostratigraphic analysis of the MADE site with full-resolution GPR and direct-push hydraulic profiling. Geophysical Research Letters 38: L06405.
- Eggleston, J., and S. Rojstaczer (1998), Identification of large-scale hydraulic conductivity trends and the influence of trends on contaminant transport, Water Resources Research, 34: 2155–2168.
- Fiori, A., G. Dagan, I. Jankovic, and A. Zarlenga (2013), The plume spreading in the MADE transport experiment: Could it be predicted by stochastic models? Water Resources Research, 49.

- Freyberg, D. L. (1986), A natural gradient experiment on solute transport in a sand aquifer: 2. Spatial moments and the advection and dispersion of nonreactive tracers. Water Resources Research, 22: 2031–2046.
- Garabedian, S. P., D. R. LeBlanc, L. W. Gelhar, and M. A. Celia (1991), Large-scale natural gradient tracer test in sand and gravel, Cape Cod, Massachusetts: 2. Analysis of spatial moments for a nonreactive tracer. Water Resources Research, 27: 911–924.
- Gelhar, L. W. (1993), Stochastic subsurface hydrology. Prentice-Hall Inc., Englewood, NJ.
- Harvey, C., and S. M. Gorelick (2000), Rate-limited mass transfer or macrodispersion: Which dominates plume evolution at the Macrodispersion Experiment (MADE) site? Water Resources Research, 36: 637–650.
- Hess, K. M., S. H. Wolf, and M. A. Celia (1992), Large-scale natural gradient tracer test in sand and gravel, Cape Cod, Massachusetts: 3. Hydraulic conductivity variability and calculated macrodispersivities. Water Resources Research, 28: 2011–2027.
- Hyndman, D. W., M. J. Dybas, L. Forney, R. Heine, T. Mayottee, M. S. Phanikumar, G. Tatara, J. Tiedje, T. Voice, R. Wallace, D. Wiggert, X. Zhao, and C. S. Criddle (2000), Hydraulic characterization and design of a full-scale biocurtain. Ground Water 38: 462–474.
- Liu, G., C. Zheng, G. R. Tick, and J. J. Butler Jr., and S. M. Gorelick (2010), Relative importance of dispersion and rate-limited mass transfer in highly heterogeneous porous media: Analysis of a new tracer test at the macrodispersion experiment (MADE) site. Water Resources Research, 46: W03524.
- Liu, G., J. J. Butler Jr., G. C. Bohling, E. Reboulet, S. Knobbe, and D. W. Hyndman (2009), A new method for high-resolution characterization of hydraulic conductivity. Water Resources Research, 45: W08202.
- Koltermann, C. E., and S. M. Gorelick (1996), Heterogeneity in sedimentary deposits: A review of structure-imitating, process-imitating, and descriptive approaches. Water Resources Research, 32: 2617–2658.
- LeBlanc, D. R., S. P. Garabedian, K. M. Hess, L. W. Gelhar, R. D. Quadri, K. G. Stollenwerk, and W. W. Wood (1991), Large-scale natural gradient tracer test in sand and gravel, Cape Cod, Massachusetts: 1. Experimental design and observed tracer movement. Water Resources Research, 27: 895–910.
- Mackay, D. M., D. L. Freyberg, P. V. Roberts, and J. A. Cherry (1986), A natural gradient experiment on solute transport in a sand aquifer: 1. Approach and overview of plume movement. Water Resources Research, 22: 2017–2029.
- Meerschaert, M. M., M. Dogan, R. L. Van Dam, D. W. Hyndman, and D. A. Benson (2013), Hydraulic conductivity fields: Gaussian or not? Water Resources Research, 49, doi:10.1002/wrcr.20376.

- Molz, F. J., O. Güven, J. G. Melville, R. D. Crocker, and K. T. Matteson (1986), Performance, analysis, and simulation of a two-well tracer test at the mobile site. Water Resources Research, 22: 1031–1037.
- Phanikumar, M. S., D. W. Hyndman, X. Zhao, and M. Dybas (2005), A three-dimensional model of microbial transport and biodegradation at the Schoolcraft, Michigan site. Water Resources Research, 41: W05011.
- Sudicky, E. A. (1986), A natural gradient experiment on solute transport in a sand aquifer: Spatial variability of hydraulic conductivity and its role in the dispersion process. Water Resources Research, 22: 2069–2082.
- Whittaker, J., and G. Teutsch (1999), Numerical simulation of subsurface characterization methods: application to a natural aquifer analogue. Advances in Water Resources, 22: 819-829.
- Zheng, C., and S. M. Gorelick (2003), Analysis of solute transport in flow fields influenced by preferential flowpaths at the decimeter scale. Ground Water 41: 142–155.
- Zheng, C., and P. Wang (1999), MT3DMS: A modular three-dimensional multispecies transport model for simulation of advection, dispersion, and chemical reactions of contaminants in groundwater systems; documentation and user's guide.
- Zimmerman, D. A., G. de Marsily, C. A. Gotway, M. G. Marietta, C. L. Axness, R. L. Beauheim, R. L. Bras, J. Carrera, G. Dagan, P. B. Davies, D. P. Gallegos, A. Galli, J. Gómez-Hernández, P. Grindrod, A. L. Gutjahr, P. K. Kitanidis, A. M. Lavenue, D. McLaughlin, S. P. Neuman, B. S. RamaRao, C. Ravenne, and Y. Rubin (1998), A comparison of seven geostatistically based inverse approaches to estimate transmissivities for modeling advective transport by groundwater flow. Water Resources Research, 34: 1373-1413.

Chapter 5

Quantifying the value of different data sets and modeling schemes for flow and transport simulations

5.1 Introduction

Depending on the level of heterogeneity, flow and transport modeling through aquifers can be an extremely challenging task. Previous research has shown that improvement of modeling results can be achieved in multiple ways, including: (1) different modeling approaches to account for some of the behavior observed in tracer experiments, (2) a better knowledge of the (statistical) distribution of hydraulic conductivity (*K*) by collecting more or better field data, and (3) addition of complementary data that give information on the structural characteristics of the aquifer.

Regarding the different modeling approaches, when the classic ADE approach does not produce acceptable results, alternatives have been proposed. These approaches include, amongst others, preferential flow paths [*Zheng and Gorelick*, 2003] and mass transfer between mobile and immobile domains [*Harvey and Gorelick*, 2000]. The difficulty with these approaches is that they are difficult to parameterize based on field data and are thus non-predictive.

Regarding the statistical distribution of subsurface properties, direct measurements of *K* have traditionally been done using flowmeters. This is a common, easily accessible, and relatively cheap method that requires installation of a groundwater well. This method is not sensitive to low *K*, but is very capable of measuring high *K* values [*Bomana et al.*, 1997]. Disadvantages of this method include an unknown support volume, sensitivity to well bore disturbance, and low vertical resolution. In recent years a new method, the High Resolution

Hydraulic Conductivity (HRK) tool has been developed, which allows measurements of K for smaller support volumes and higher vertical resolution than flowmeters. This method, which is sensitive to low K, but cannot yet measure K above 60 m/d, has been discussed in considerable detail in the previous chapters and in $Liu\ et\ al.$ [2009, 2012]. A disadvantage of this method is that it is not yet not widely accessible and relatively expensive.

Many researchers have shown that complimentary data can greatly improve modeling results. These data can be derived from geophysical measurements, such as electrical resistivity [e.g., *Atekwana et al.*, 2000; *Cassiani et al.*, 2006], nuclear magnetic resonance (NMR) measurements [*Legchenko et al.*, 2002], seismic [*Hyndman, et al.*, 1994; *Hyndman and Gorelick*, 1996], and surface and cross borehole ground-penetrating radar (GPR) [e.g., *Tronicke et al.*, 2002]. GPR is very sensitive to textural changes, porosity and water content, and can be used to obtain structural information of an aquifer; GPR can thus provide complementary data to direct measurements of *K*.

Of the different methods presented above, each has different levels of detail, cost, and benefit. Previous chapters in this dissertation have discussed the relative benefits of various alternative approaches and added data sets for modeling flow and transport at the MADE site. The objective of this chapter is to compare the various additions or improvements to modeling the flow and transport behavior at the MADE site, as observed during the MADE-1 tracer test [Boggs, 1991]. The comparisons presented here are only a subset of possibilities, and are based on the available data in the injection area (Figure 5.1).

The first comparison of modeling results in this chapter is between simulations through *K* fields parameterized with HRK data and through fields parameterized with a combination of HRK data and GPR facies. This section is a natural follow up on Chapter 4. The next section of

this chapter is a cost-benefit analysis of different options, which focuses on (1) the effects of transient simulation (of the water table), (2) a *K* field parameterized with only flowmeter data measured during the MADE studies [*Boggs*, 1991, 1992], (3) the amount of HRK information, and 4) GPR facies. All results are compared with the MADE-1 measurements and a single base simulation that used steady-state flow and parameterization based on 25 HRK profiles (this base simulation was discussed in Chapter 4 – Figure 4.3c).

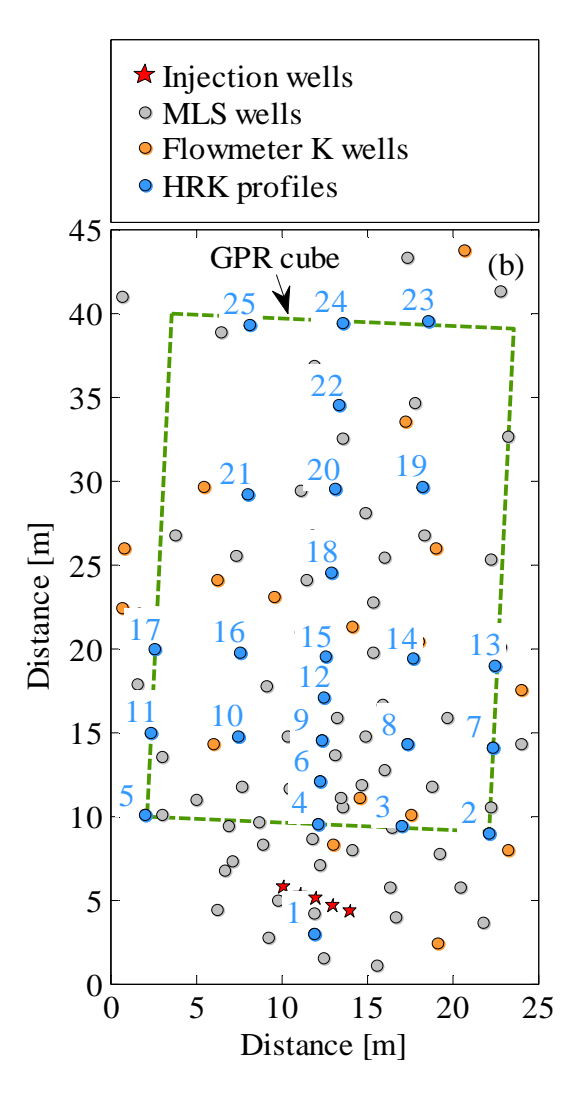


Figure 5.1 A detailed map of the model domain with locations of flowmeter *K* (orange) and HRK measurements (blue) and multi-level sampler (grey) wells. The area of 3D GPR data is given by the rectangle with green dashed line. Injection wells are given with red stars. See Figure 4.1 for the location within the larger MADE site.

5.2 Complementary GPR data

In this research, 3D full-resolution GPR data were used as complementary data to measurements of *K* using the HRK tool. GPR data were collected with 50 and 100 MHz antennas using a trigger wheel and ropes for positional guidance (details in Chapter 2). The profile separation was selected as equal to step size and smaller than a 1/4 of the GPR signal wavelength [*Grasmueck et al.*, 2005]. Data were processed using a de-wow function and a low pass filter. Time-depth conversion was made using the velocities derived from common-mid-point and cross borehole measurements. An automated search algorithm was used to pick the reflectors. Reflectors were then grouped using another automated algorithm to create the facies boundaries.

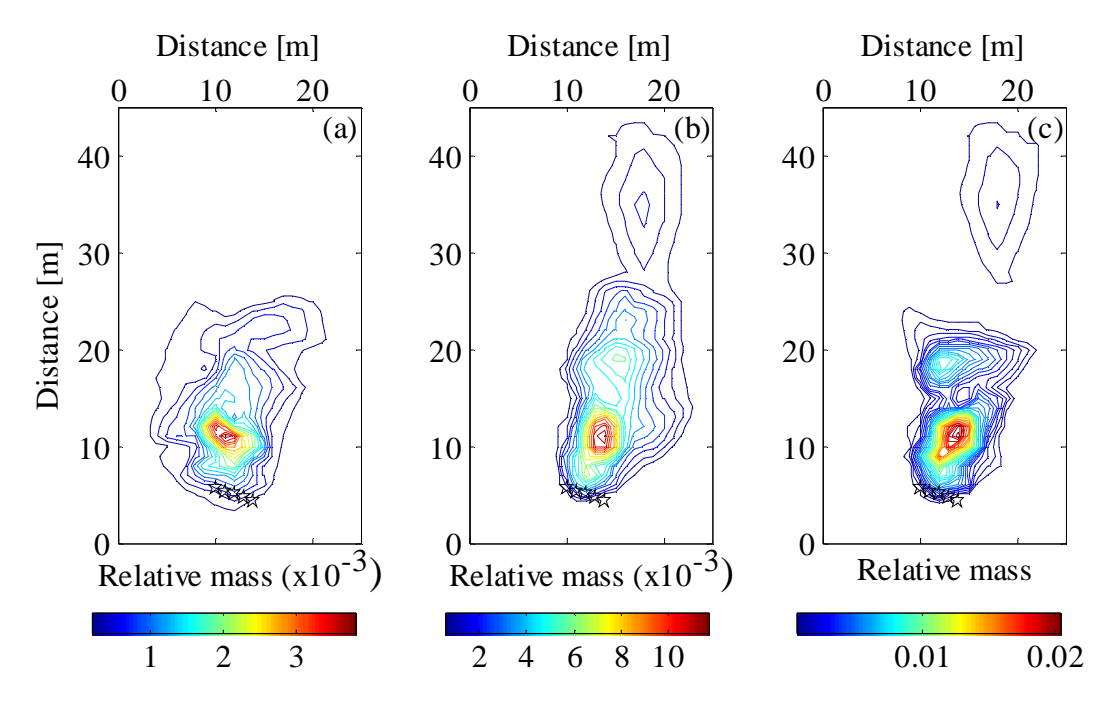


Figure 5.2 Vertically integrated contour maps of relative mass; (a) MADE-1 experiment at t=503 days, (b) mean of 6 simulations, (c) best head change simulation. *K* fields for the simulations in (b) and (c) were based on a combination of HRK data and GPR facies (these maps can be compared with Figure 4.2, which presents contour maps of relative mass for *K* fields based on just HRK data).

The *K* field simulation procedure was similar to the one for the scenario with HRK data alone (see Chapter 4), but now separated by facies (see Chapter 3). For each facies, *K* fields were

generated using appropriate depth interval from the same noise field. *K* fields for each facies were then stitched together to create a 3D model for the flow and transport simulations in MODFLOW and MT3D [*Zheng and Wang*, 1999]. From the simulation results, 2D vertically integrated contour maps and 1D concentration profiles were created following the same procedure as in Chapter 4.

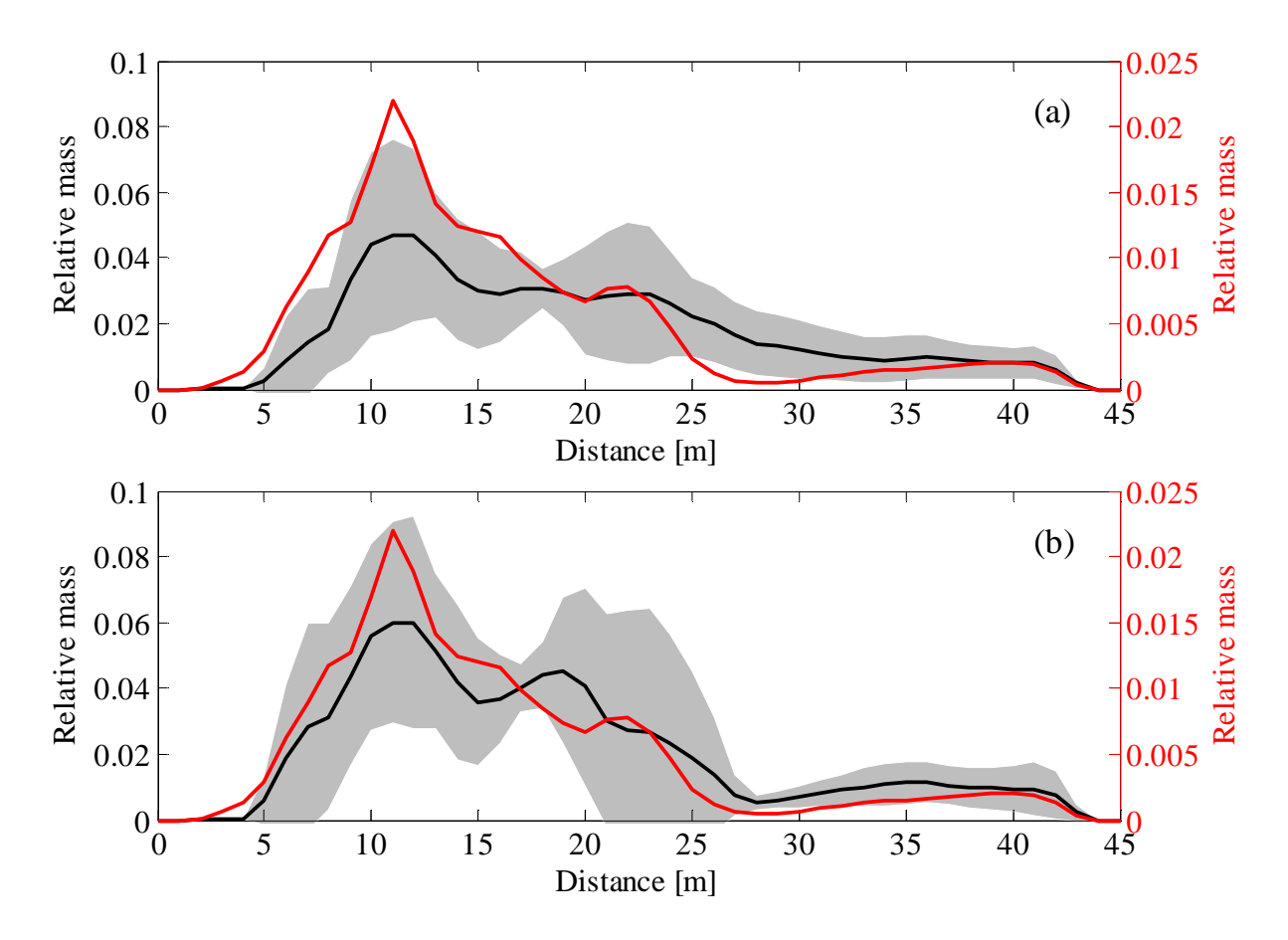


Figure 5.3 Relative mass distribution profiles for the MADE-1 experiment at t=503 days (red line), and the mean and 2σ range of 6 simulations (black line and gray shaded area, respectively). Simulations used (a) K fields based on just HRK data and (b) K fields based on a combination of HRK data and GPR facies.

Similar as with the *K* fields based on just the HRK data (Chapter 4) in these simulations the recovered mass is significantly larger than the mass recovered during the experiment.

However, the extent of the plume was very comparable to the measured data (Figure 5.2) and the location of maximum relative mass was similar to what was observed (Figure 5.3). Most

importantly, the facies-based approach resulted in a much better characterization of the plume tail (Figure 5.3b). This improvement is because the facies boundaries allow one to determine the high-*K* zones of the aquifer in more detail. In summary, this comparison shows that the simulations that incorporate structural information from GPR-derived hydrofacies better reproduce the part of the tracer that rapidly moved down-gradient.

5.3 Cost-benefit analysis

The objective of this section is to compare the relative benefits and disadvantages of different modeling approaches, use of flowmeter *K* data, different densities of HRK information, and addition of a complementary data set (GPR facies). The results are compared to the MADE-1 experiment data and to the base simulation, which had the best match to the head-change criterion (Figure 4.3b). This base simulation used steady state flow, all 25 HRK data for conditioning, and no flowmeter data or GPR facies. For all compared *K* fields, the same noise field was used.

The results are presented qualitatively using 2D vertically integrated mass distribution maps (contour maps) and 1D mass distribution profiles. Additionally, for quantitative comparison of the results, Table 5.1 lists the details of each simulation (down-gradient distance to maximum mass peak, peak and tail shapes, injected mass, and mass recovery for each simulation), and compares the RMS error between simulation and field data. All contour maps and 1D concentration profiles have been normalized by total mass so that the results can be more easily compared.

94

Table 5.1 Quantitative measures for the comparison of simulation scenarios and field experiment (R^2 values were calculated comparative to the MADE-1 experiment t=503 days in the first row).

	Peak	\mathbb{R}^2			Mass [grams]		
	loc. [m]	Total (0-45m)	Peak (0-25m)	Tail (25-45m)	Injected	Simulated	Recovered
Data (MADE-1, t=503 days)	11.5	1	1	1	25000.00 (100 %)	N/A	5326.5 (23.7 %)
Base simulation	11.5	0.899	0.880	0.101	25183.49 (100 %)	23722.07 (94.2 %)	21969 (87.2 %)
Transient flow	11.5	0.879	0.843	0.000	24917.69 (100 %)	14342.35 (57.5 %)	21899.35 (87.9 %)
Flowmeter K	19.5	0.002	0.001	0.002	25173.43 (100 %)	12193.20 (48.4 %)	14469 (57.5 %)
GPR data	11.5	0.830	0.783	0.760	25181.85 (100 %)	24634.42 (97.8 %)	24363 (96.7 %)
80% HRK	11.5	0.924	0.895	0.445	25161.81 (100 %)	19296.71 (76.7 %)	18583.3 (76.8 %)
60% HRK	11.5	0.893	0.874	0.102	25177.01 (100 %)	23045.80 (91.5 %)	21632.7 (85.9 %)
40% HRK	8.5	0.397	0.236	0.267	25161.48 (100 %)	21670.72 (86.1 %)	25013.7 (99.4 %)
20% HRK	8.5	0.712	0.624	0.049	25174.02 (100 %)	25111.05 (99.7 %)	27940.6 (110.9 %)

5.3.1 Transient flow

Since the flow-transport simulations are computational experiments, simplification is required. Simplification is also beneficial due to lower computational costs. In hydrologic simulations it is common to use steady state solutions. However, under natural conditions, flow and transport is more complicated than is typically achieved by simplified models. Unconfined aquifers are especially challenging to model with precision, since such aquifers are usually very shallow, highly heterogeneous and open to recharge through the surface via infiltration and discharge. Thus, flow and transport simulations in unconfined aquifers may require transient solutions to reproduce the effect of changing water table depth. Transient solutions require

periodically collected piezometric measurements to specify the changes in water table depth along boundaries of models. Computational power and time for transient simulations are also more intense than for steady state simulations.

Comparative analysis of flow-transport simulations involving transient and steady state flow schemes are presented in this section. The objective of this comparison is to test the effect of possible tracer entrapment in vadose zone due to water level changes, as was hypothesized by *Adams and Gelhar* [1992]. The transient flow simulation was based on the piezometric measurements collected during the MADE-1 experiment. This simulation used the same *K* field as the base simulation; only the head conditions were changed.

The results shown in the contour maps of normalized mass (Figure 5.4) and 1D concentration profiles (Figure 5.5) suggest that the transient flow had very little effect. The transient flow simulations were almost identical to the ones using steady state flow. It is hypothesized that this small difference is in part due to the fact that the injection screen was located at a depth of 7.4-8 meters (around 3.8 meters below the depth of the water table at the start of the experiment and simulation). Considering that the transient simulation took significantly more computer time and required the additional piezometric data, this modification of the approach presents very little additional value.

Quantitative measures presented in Table 5.1 show that the transient flow simulation is very similar to the base simulation, except the percentage of mass that stayed in the model domain after 503 days of simulation (57.5 % versus 94.2% for the base simulation). Higher gradient periods during the flow simulation may be the cause of this difference since the seasonal changes in the water table promote faster flow in the model domain and more mass leaves through the northern boundary of the domain. Although mass entrapment in vadose zone could

be another reason, it was not captured by the simulation and numerical sampling procedure of the simulated plume.

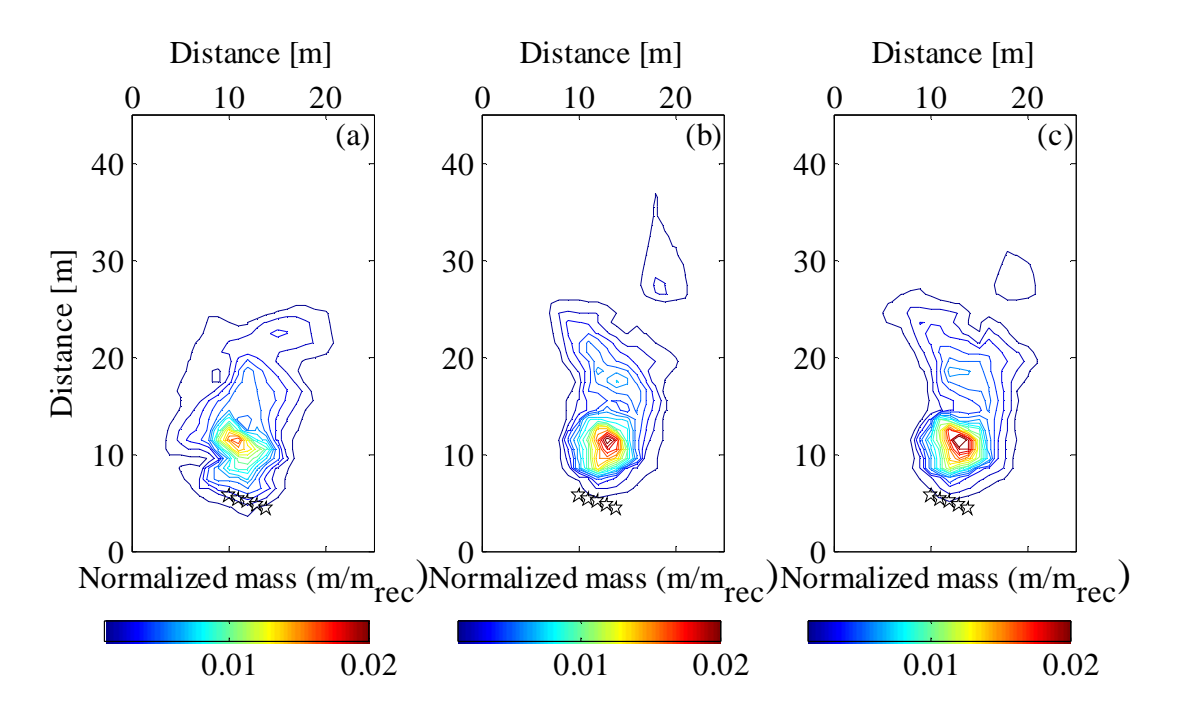


Figure 5.4 Vertically integrated contour maps of normalized mass; (a) MADE-1 experiment at t=503 days, (b) base simulation, (c) transient flow simulation.

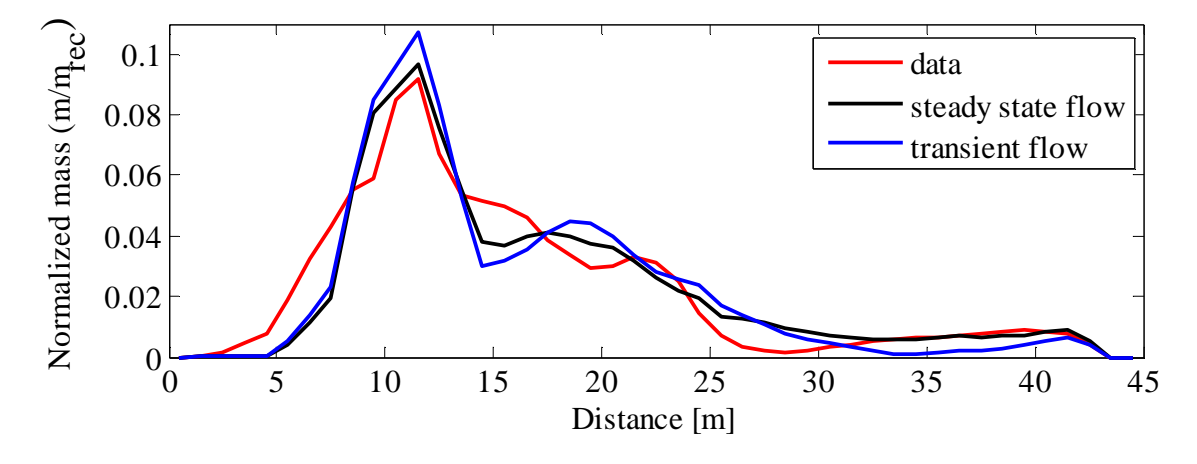


Figure 5.5 Normalized mass distribution profiles of the MADE-1 experiment at t=503 days (red line), base simulation (black line), and transient flow scheme (blue line).

5.3.2 Flowmeter K

Direct measurements of *K* have traditionally been done using flowmeters. At the MADE site many flowmeter measurements were conducted during the MADE field experiments in the 1980s and 1990s (see Figure 5.1 for the locations of flowmeter wells in the study domain). Flowmeter measurements in heterogeneous media are not very sensitive to low *K*, but very sensitive to high *K* zones [*Bomana et al.*, 1997]. Disadvantages of this method include the unknown support volume, low vertical resolution, and averaging over a bulk volume of different *K* zones.

Here, a direct comparison is given between simulations through K fields based on (1) flowmeter data, and (2) the more recently introduced HRK tool. The stochastic K fields were created using the same fractal methods discussed in Chapter 4 with the flowmeter K data as hard conditioning points.

The results show that for the simulation based on the flowmeter data (Figure 5.6c and 5.7), the mass moves much faster down-gradient than for the simulations based on the HRK data (Figure 5.6b and 5.7). In fact, a significant portion of the tracer mass moved outside the model domain (Table 5.1). Flowmeter measurements are not sensitive to the low K, which explains why the average K is higher than HRK.

Quantitative measures provided in Table 5.1 suggest that the flowmeter *K* based simulation cannot reproduce the observed plume shape at the MADE site. This simulation resulted in the most incomparable plume shape, peak location, and tail behavior of all scenarios tested.

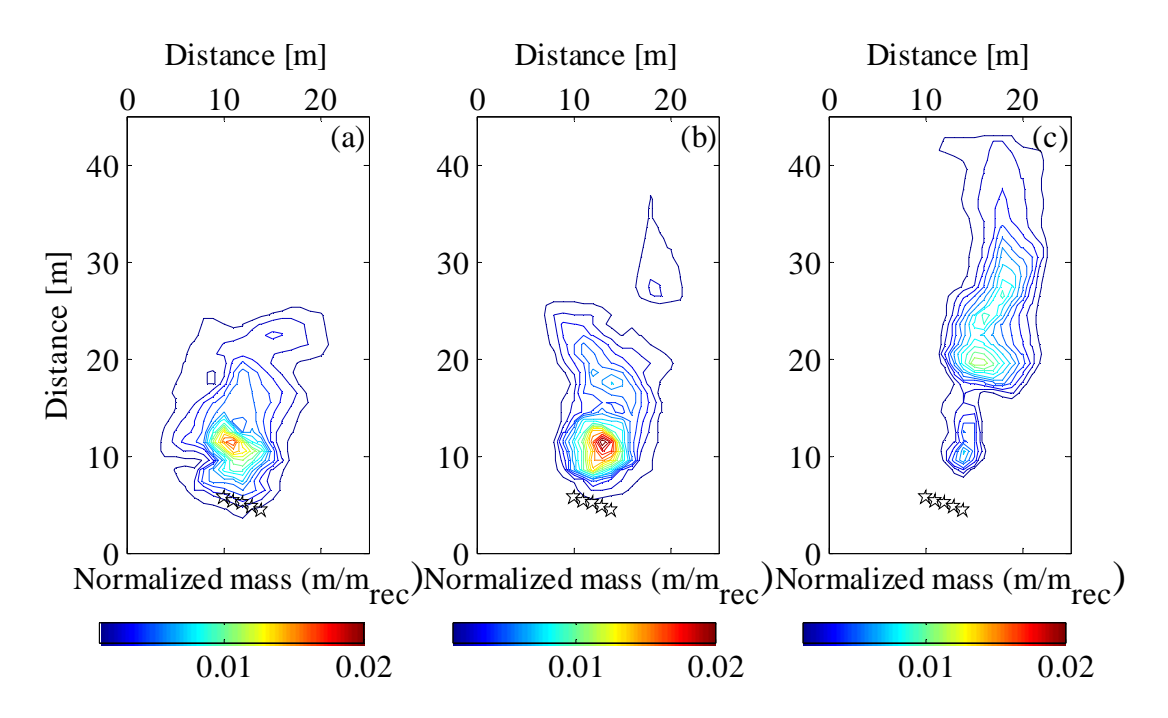


Figure 5.6 Vertically integrated contour maps of normalized mass; (a) MADE-1 experiment at t=503 days, (b) base simulation, (c) simulation based on just flowmeter K data.

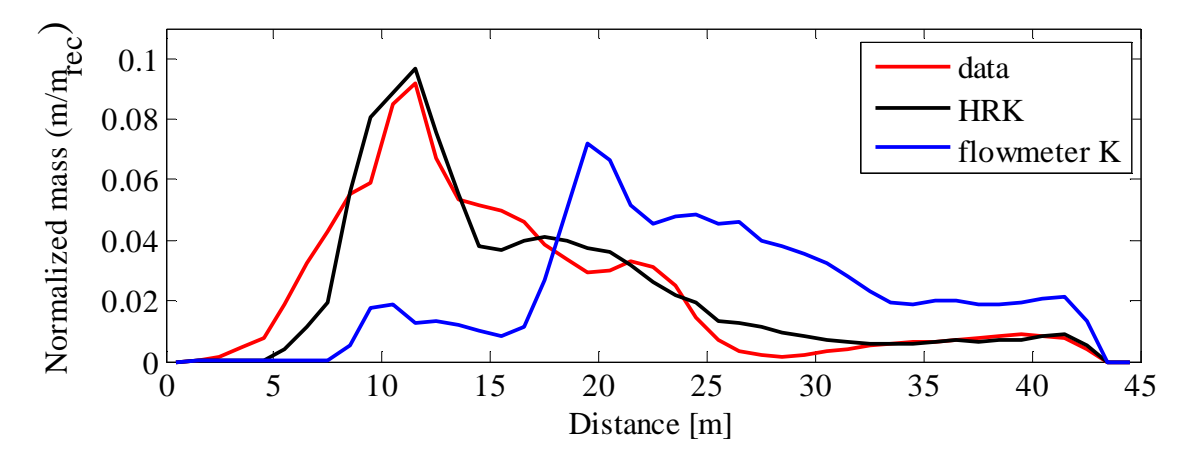


Figure 5.7 Normalized mass distribution profiles of the MADE-1 experiment at t=503 days (red line), base simulation (black line), and simulation based on just flowmeter *K* data (blue line).

5.3.3 Effect of conditioning data density

A random number generator was used to create subsets of HRK measurement profiles in the modeling domain. The number of HRK profiles used for the K field parameterization was decreased from 25 (the base simulation) to 20 (80%), 15 (60%), 10 (40%), and 5 (20%). HRK

profile #1, which is located very near to the injection location (see Figure 5.1) was removed from each of parameterized fields. The same noise field was used to generate each *K* field.

A visual comparison of 2D vertically integrated mass distribution maps (Figure 5.8c-f) shows that decreasing the number of HRK profiles has a significant effect on both the plume extent and shape. Although the locations of randomly selected HRK profiles have an effect on the results, it is clear that the accuracy of modeled plumes generally decreases with number of HRK profiles. As expected, the plume simulated using 80 % of the HRK profiles was most comparable to the base simulation.

The effects of reducing the HRK profile density on the peak and tail shapes of simulated plumes is also clear from the 1D mass distribution profiles (Figure 5.9). HRK profiles located near the injection location control the quality of peak representation. The simulation with 40% of HRK profiles has no nearby HRK profiles (Figure 5.8e), which resulted in a highly distorted peak shape (Figure 5.9c). It is also notable that although 1D mass distribution profiles (in this case: 60% HRK profiles; Figure 5.9b) may look nearly unchanged from the base simulation and the situation with more HRK profiles, the corresponding integrated mass distribution map (Figure 5.8d) shows a strong deviation from the base simulation.

The simulations with 20 and 40 % of the HRK profiles provided poor correlation with the base simulation results for both the peak and the tail shape of the mass distribution profiles (Table 5.1). The mass recoveries for these simulations also significantly deviated from the base simulation.

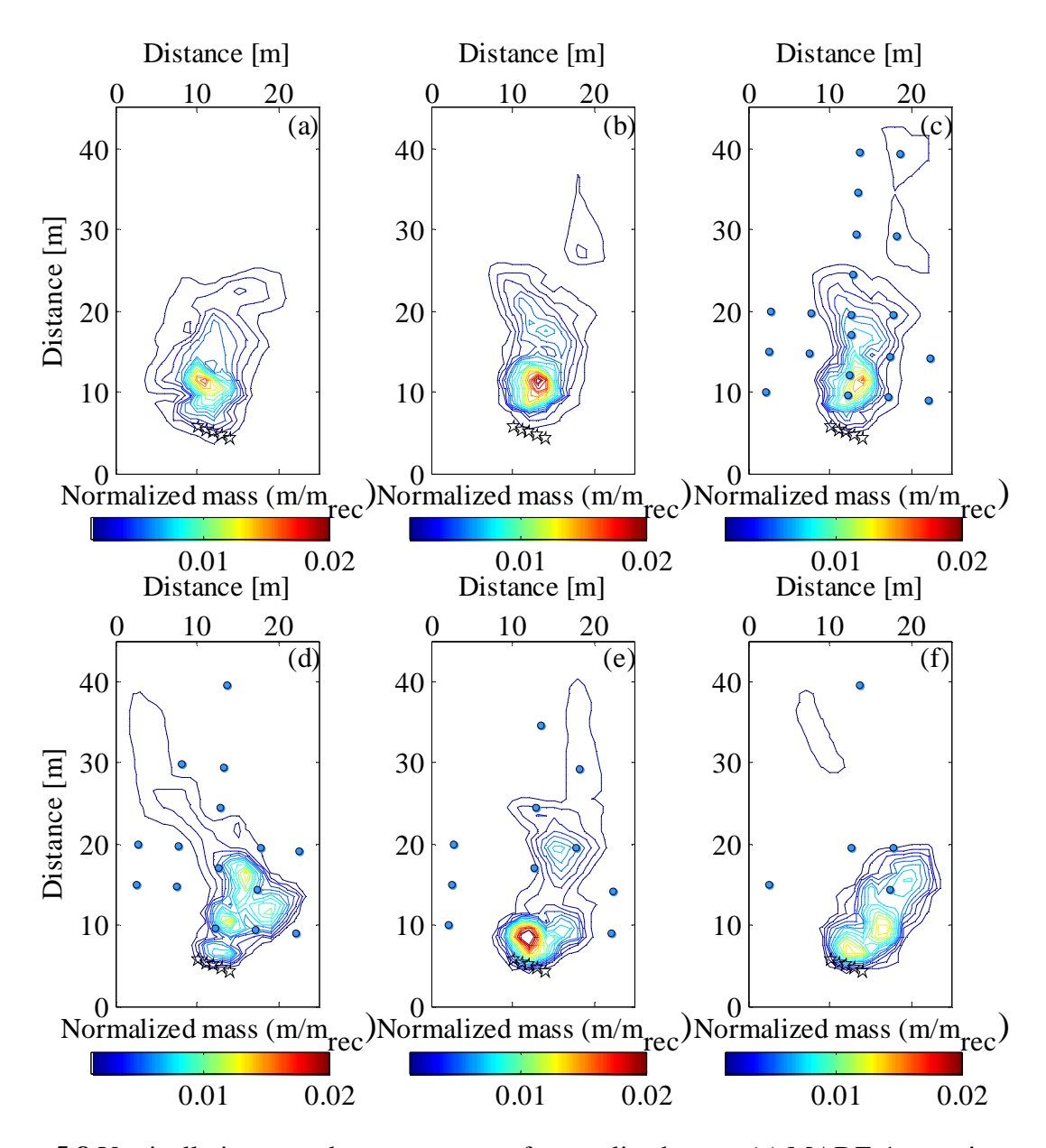


Figure 5.8 Vertically integrated contour maps of normalized mass: (a) MADE-1 experiment at t=503 days, (b) base simulation based on all 25 HRK profiles, and simulations based on (c) 20, (d) 15, (e) 10, and (f) 5 randomly selected HRK profiles. The randomly selected HRK profiles used to generate the K fields are shown with blue symbols; see Figure 5.1 for the location of all 25.

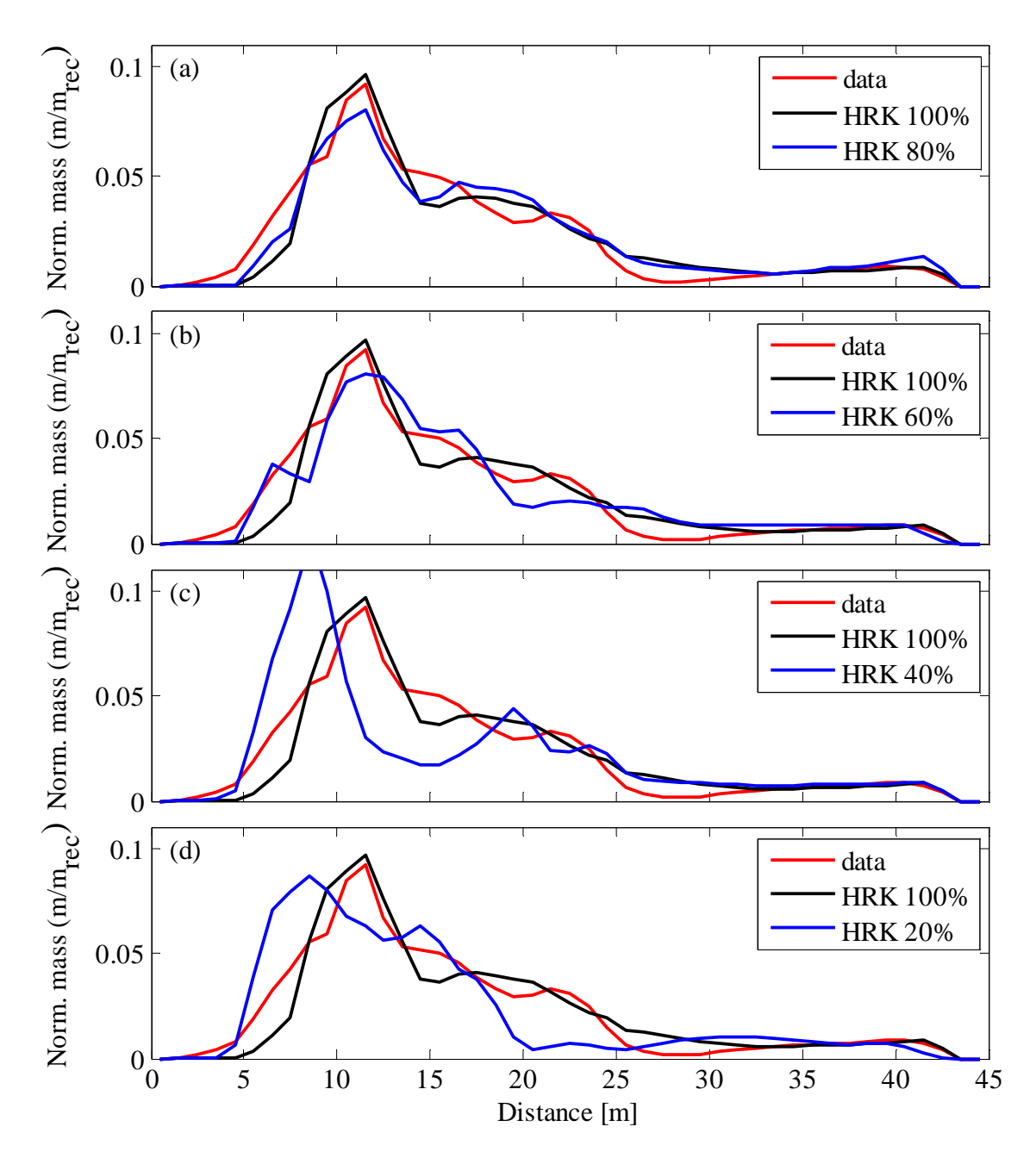


Figure 5.9 Normalized mass distribution profiles of the MADE-1 experiment at t=503 days (red line), base simulation (black line), and simulations based randomly selected number of HRK profiles (blue line). (a) 80% of HRK profiles (#'s 2, 3, 4, 5, 6, 7, 8, 10, 11, 12, 14, 15, 16, 17, 18, 19, 20, 22, 23, 24), (b) 60% of HRK profiles (#'s 2, 3, 4, 8, 10, 11, 12, 13, 14, 16, 17, 18, 20, 21, 24), (c) 40% of HRK profiles (#'s 2, 5, 7, 11, 12, 14, 17, 18, 19, 22) (d) 20% of HRK profiles (#'s 8, 11, 14, 15, 24). See Figure 5.1 for the locations of the HRK profiles.

5.3.4 Complementary GPR data

To allow comparison with the previous sections, one simulation for a *K* field partially based on GPR facies is presented. Rather than using the average of 6 simulations (Section 5.2), only the simulation for the noise field that best matched the head-change criterion is presented here.

As already discussed in Section 5.2, when GPR facies are used to help construct the *K* field, the mass contour maps do not differ much from those based on just HRK data (Figure 5.10). However, the tail of the tracer plume is much better characterized (Figure 5.11).

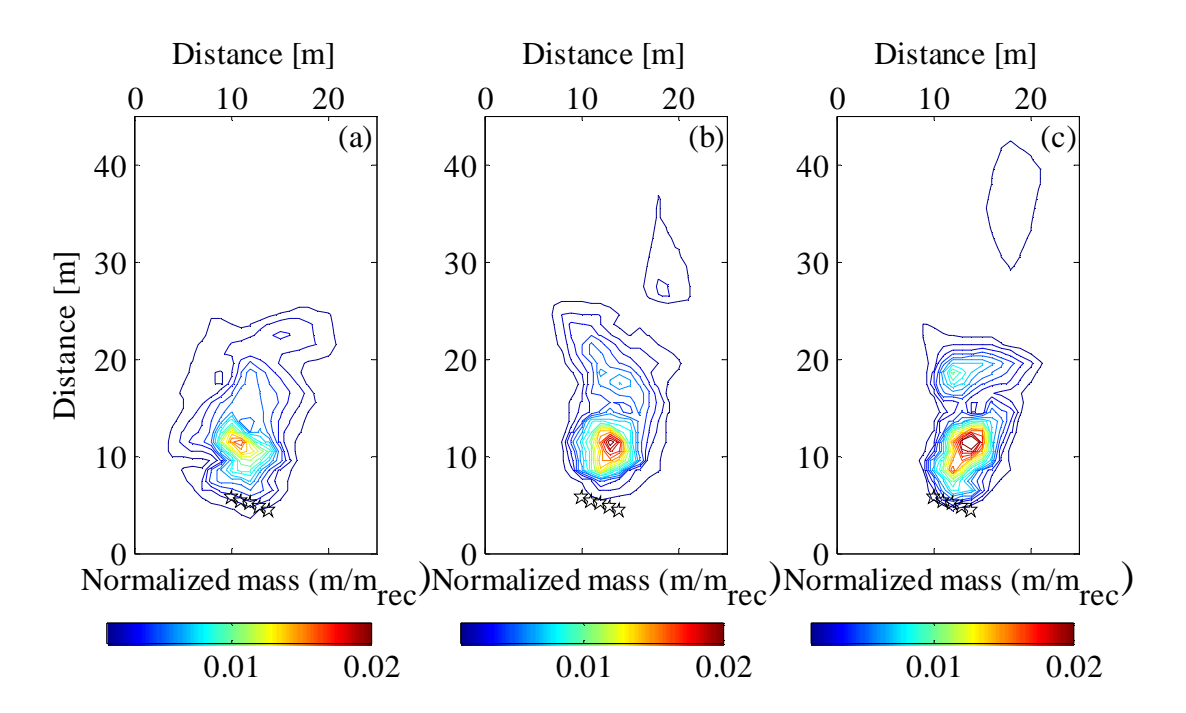


Figure 5.10 Vertically integrated contour maps of normalized mass: (a) MADE-1 experiment at t=503 days, (b) base simulation, and (c) simulation based on a combination of HRK data and GPR facies.

Correlation coefficients provided in Table 5.1 shows that the simulation with GPR data exhibits the best representation of heavy tail behavior observed in the mass distribution curves. However, the peak representation is not quite as good as the base simulation. This can be

explained by the lack of GPR data around the injection area (Figure 5.1). As mentioned earlier in Chapter 1, the source area was dug out during the MADE-3 macro scale experiment in the 1990s. Therefore, 3D GPR data were not collected in the vicinity of the source wells, which limits the effective use of GPR-derived facies boundaries around the injection area.

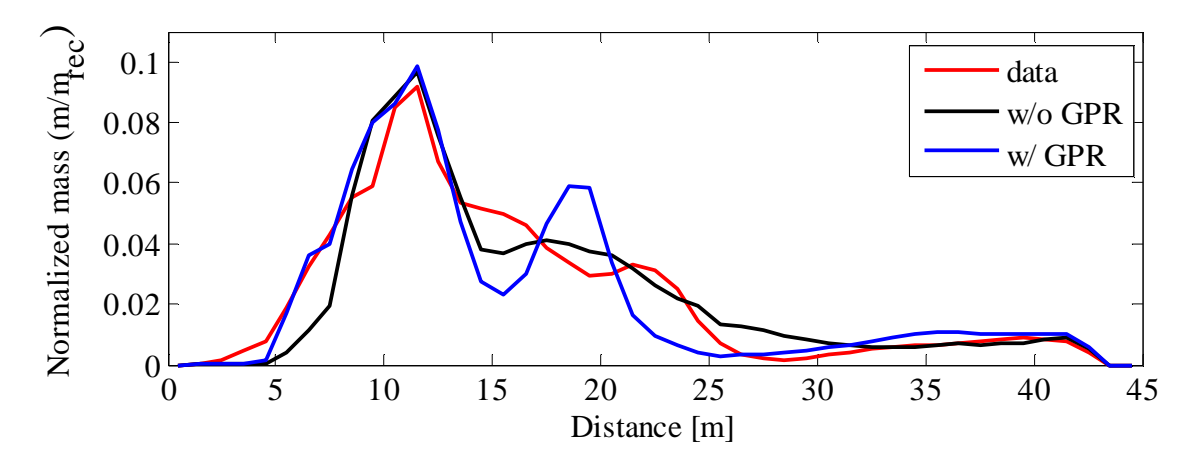


Figure 5.11 Normalized mass distribution profiles of the MADE-1 experiment at t=503 days (red line), base simulation (black line), and simulation based on a combination of HRK data and GPR facies.

5.4 Conclusions

The first section of this chapter introduces the use of GPR data in combination with HRK data and presents the results of simulations for both types of *K* fields. The mean of the flow and transport simulations involving the GPR data exhibits a better representation of the tailing behavior. However, for the simulations based on the facies boundary information the standard deviation of the simulation means was somewhat higher than for the simulations without facies. This might be explained by the fact that the criterion used to select the noise fields was based on a maximum head-change (Chapter 4). Here, the same noise fields were used without taking into account any effects on the head changes (due to a low *K* facies around the injection depth, they increased from a mean of 0.67 m to 1.03 m with a larger standard deviation).

In the second section of this chapter, the effects of complementary data, transient flow, use of conventional flowmeter *K* data, and different densities of HRK data were examined.

Based on these comparisons, the following conclusions can be drawn:

- Good representations of peak behavior were obtained in the base simulation, in transient flow simulations, and in the simulation with the aid of GPR data.
- Flowmeters are the most common tool to collect *K* information in field investigations, but the results presented here show that they are incapable of representing the *K* field in sufficient detail, resulting in wrong plume behavior in the transport simulations.
- The best representation of tail behavior was obtained using GPR facies as
 complementary data. This outcome shows that in cases where heavy tail behavior exists,
 GPR facies boundaries can help identify the preferential flow paths through an aquifer.
- Reducing the density of HRK profiles resulted in less comparable simulation results. In this case, 60% of HRK profiles were required to obtain reasonable 1D mass profiles, but 80% were required for a good 2D mass distribution. However, it is important to point out that the locations of the selected HRK profiles had a critical effect on the simulation results. Omission of the HRK profiles close to the source area had a strong negative effect on representation of the peak behavior.

- Adams, E. E., and L. W. Gelhar (1992), Field study of dispersion in a heterogeneous aquifer: 2. Spatial moments analysis. Water Resources Research, 28(12), 3293–3307, doi:10.1029/92WR01757.
- Atekwana, E. A., W. A. Sauck, and D. D. Werkema (2000), Investigations of geoelectrical signatures at a hydrocarbon contaminated site. Journal of Applied Geophysics, 44: 167-180.
- Boggs, J. M., S. C. Young, L. M. Beard, L. W. Gelhar, K. R. Rehfeldt, and E. E. Adams (1992), Field study of dispersion in a heterogeneous aquifer: 1. Overview and site description. Water Resources Research, 28, 3281-3291.
- Boggs, J. M. (1991), Database for the first macrodispersion experiment (MADE-1).
- Bomana, G. K., F. J. Molz, and K. D. Boonec (1997), Borehole flowmeter application in fluvial sediments: methodology, results, and assessment. Ground Water, 35: 443–450. doi: 10.1111/j.1745-6584.1997.tb00104.x.
- Cassiani, G., V. Bruno, A. Villa, N. Fusi, A. M. Binley (2006), A saline trace test monitored via time-lapse surface electrical resistivity tomography. Journal of Applied Geophysics, 59: 244-259.
- Grasmueck, M., R. Weger, and H. Horstmeyer (2005), Full-resolution 3D GPR imaging. Geophysics, 70: K12-K19.
- Harvey, C., and S. M. Gorelick (2000), Rate-limited mass transfer or macrodispersion: Which dominates plume evolution at the macrodispersion experiment (MADE) site? Water Resources Research, 36: 637–650.
- Hyndman, D. W., J. M. Harris, and S. M. Gorelick (1994), Coupled seismic and tracer test inversion for aquifer property characterization. Water Resources Research, 30.7: 1965-1977.
- Hyndman, D. W., and S. M. Gorelick (1996), Estimating lithologic and transport properties in three dimensions using seismic and tracer data: The Kesterson aquifer. Water Resources Research, 32.9: 2659-2670.
- Legchenko, A., J. M. Baltassat, A. Beauce, and J. Bernard (2002), Nuclear magnetic resonance as a geophysical tool for hydrogeologists. Journal of Applied Geophysics, 50: 21-46.
- Liu, G., J. J. Butler Jr., G. C. Bohling, E. Reboulet, S. Knobbe, and D. W. Hyndman (2009), A new method for high-resolution characterization of hydraulic conductivity, Water Resources Research, 45(8), doi:10.1029/2009WR008319.
- Liu, G., J. J. Butler Jr., E. Reboulet, and S. Knobbe (2012), Hydraulic conductivity profiling with direct-push methods, Grundwasser, 17(1), 19–29.

- Tronicke, J., P. Dietrich, U. Wahlig, E. Appel (2002), Integrating surface georadar and crosshole radar tomography: A validation experiment in braided stream deposits. Geophysics, 67: 1516-1523.
- Zheng, C., and S. M. Gorelick (2003), Analysis of solute transport in flow fields influenced by preferential flowpaths at the decimeter scale. Ground Water 41: 142–155.
- Zheng, C., and P. Wang (1999), MT3DMS: A modular three-dimensional multispecies transport model for simulation of advection, dispersion, and chemical reactions of contaminants in groundwater systems; documentation and user's guide.

Chapter 6

Synthesis

This dissertation presents a set of techniques to improve the characterization of and flow and transport simulations through highly heterogeneous aquifers. The Macro Dispersion Experiment site in Mississippi was selected to test the developed methods due to existing extensive data sets and previous research. The biggest challenge for this site is the highly heterogeneous nature of the porous media and the observed non-Gaussian transport during the large scale tracer tests in 1980s and 1990s [Boggs, 1991; Boggs et al., 1992]. Flow meter K data, collected prior to those tracer experiments, suggested that the K distribution was highly heterogeneous. In previous studies, this behavior could not be successfully modeled using advection and dispersion as the primary mechanisms. Indeed, this extraordinary behavior led most of the hydrological research community to believe that the advection-dispersion equation (ADE) is not capable of modeling the flow and transport in aquifers above a certain heterogeneity level.

This study was aimed to test the hypothesis that ADE is capable of modeling flow and transport even in highly heterogeneous aquifers as long as the model is supported by sufficient high resolution K data. The required high resolution K fields were created using fractal stochastic methods based on two high-resolution data sets: high-resolution direct-push K profiles and 3D full-resolution ground-penetrating radar (GPR). Below, I present a brief summary of the main outcomes of each Chapter, followed by a discussion of some new questions resulting from this work.

GPR, a high resolution non-invasive geophysical method, is capable of defining textural properties such as porosity, packing, and sorting in a spatial context. These textural properties

are related to *K* in an indirect way. Chapter 2 [based on *Dogan et al.*, 2011] presents an integrative study to investigate the consistency between GPR derived structures (or facies) and *K* data. This work was performed in an area where a recent push pull test was performed.

Descriptive statistics and distribution tests performed in Chapter 2 proved that the different facies separated statistically different *K* distributions, with a reduced level of *K* variation within each facies. Therefore, this study demonstrated that GPR-derived structural information can be successfully used to define hydrofacies.

High-resolution spatial information is necessary to create better flow and transport models, as hypothesized above. However, no invasive or non-invasive method exists to measure K fields at a spatial resolution that does not require some form of interpolation. Therefore, stochastic methods are generally required to generate parameter fields to fill in the gaps between measurement locations with similar levels of heterogeneity. To avoid drawbacks of common stochastic methods, including the inability to create parameter fields that display the connectivity of real sedimentary deposits, fractal stochastic methods were used in this dissertation. Connectivity is an important property of aquifers that can define connected high K paths as preferential flow paths. Chapter 3 [based on *Meerschaert et al.*, 2013] presents the details of the fractal K field generation technique that was developed and shows that the fractional differencing filter can remove the long-range dependence observed in K data. This finding shows that fractional differencing filters can be successfully used to further investigate the underlying distribution of K data. Parameter fields are presented that are more natural looking and have a K distribution that better matches observations from HRK profiles. Flow simulations through these fields resulted in improved representation of the transport characteristics typical for this site, such as a heavy tail and multiple concentration peaks.

The focus of the next two Chapters was on the area around the original injection wells of the Macro Dispersion Experiment tracer tests. Also, the approach demonstrated in Chapter 2 was applied to a 3D domain. Flow and transport simulations were performed following injection procedure and sampling strategy of the MADE-1 experiments. Several different *K* fields were generated using the method explained in Chapter 3. The concentrations derived from the simulations, excluding GPR facies to derive the parameter fields, were presented in Chapter 4. Vertically integrated contour maps of relative mass distribution created in this study were an innovation compared to earlier modeling efforts at the MADE site, as no other study has compared simulation results with experiment data in more than 1D. The extent of the modeled plumes and maximum mass zones were very comparable to the ones measured during the experiment. The simulations also did a good job of characterizing the fast moving heavy tail of the plume. These findings show that the proposed method using *K* fields based on just measured field data is able to define the parameters necessary for designing effective remediation solutions for real-world problems.

Chapter 5 presents a comparative study to define the value of different data sets for improving modeling results and provides insight into the required data sets for successful flow and transport modeling in heterogeneous media. This Chapter emphasizes the effect of complementary GPR data to better reproduce the heavy tail behavior of MADE plume. It also highlights the inability of flow meter *K* data to produce simulation results comparable to the observed data. It presents a comparison of the steady state and transient flow schemes, which concludes that the tracer entrapment in the vadose zone is not a strong argument to explain the poor mass recovery of the modeling efforts. Finally, an analysis of the effects of HRK

conditioning density shows that 60% to 80% of HRK profiles are needed to produce acceptable simulation results.

Despite the new developments and improvements of modeling of flow and transport in heterogeneous media presented in this dissertation, there are a few unanswered questions.

Several of these points can be summarized as follows, and may be answered with future work:

- As was shown in this dissertation, GPR facies that are derived from surface measurements are very useful to build hydrostratigraphic frameworks that can improve flow and transport modeling (Chapters 2 and 5). However, facies boundaries cannot be directly used to obtain K information. Future work could make use of inversion approaches and interpretation of borehole measurements to develop a more direct link between geophysical data and hydraulic properties of interest.
- The 3D simulations had excellent correlation with the transport observations (Chapter 4 and 5) and fractal methods provided a better tool to generate *K* fields than sequential Gaussian methods (Chapter 3). One of the two main components of fractal stochastic parameter field generation is the parameterization (fractal dimension, correlation structures and statistical measures) of the fractal method, which can be obtained using HRK data. However, the second component, the noise field, is randomly generated and of Gaussian nature. This Gaussian noise field may not be the best solution to this step, but further work would be needed to investigate whether this simplification has important consequences.
- One major disagreement between the simulations and the field experiments involves the
 mass recovery. All simulations had significantly larger mass recovery than the
 experiments, despite identical sampling and interpolation procedures. One possibility for

this observation has been considered in Chapter 5 (transient flow), but this did not address the discrepancy. Other possible explanations include the lower mean *K* throughout the model domain due to the upper of limit of the HRK tool, and an inability to reproduce the mixing in sampling wells as would have occurred during the sampling procedure in the field.

Finally, this study demonstrated that the ADE is capable of modeling flow and transport even in highly heterogeneous aquifers such as the MADE site without parameter calibration or optimization. However, high resolution parameter fields are required to enable these modeling efforts. The novel high resolution characterization tool HRK can be used in combination with high resolution geophysical methods to provide the necessary data. Even though some steps of the presented research need improvement, it presents a straightforward method to create uncalibrated, reproducible flow and transport models based on solely field data. Moreover, these models can reproduce the non-Gaussian transport behavior at the infamous MADE site.

- Dogan, M., R. L. Van Dam, G. C. Bohling, J. J. Butler Jr, and D. W. Hyndman (2011), Hydrostratigraphic analysis of the MADE site with full-resolution GPR and direct-push hydraulic profiling, Geophys. Res. Lett., 38(6), doi:10.1029/2010GL046439.
- Meerschaert, M. M., M. Dogan, R. L. Van Dam, D. W. Hyndman, and D. A. Benson (2013), Hydraulic conductivity fields: Gaussian or not? Water Resources Research, 49, doi:10.1002/wrcr.20376.
- Boggs, J. M., S. C.Young, L. M. Beard, L. W. Gelhar, K. R. Rehfeldt & E. E. Adams (1992), Field study of dispersion in a heterogeneous aquifer: 1. Overview and site description. Water Resources Research, 28(12), 3281-3291. doi:10.1029/92WR01756.
- Boggs, J. M. (1991), Database for the first Macrodispersion Experiment (MADE-1).